



## MESHFREE METHODS: MOVING BEYOND THE CUMULAN! LATTICE BOLTZMANN METHOD

Mohsen Gorakifard

**ADVERTIMENT.** L'accés als continguts d'aquesta tesi doctoral i la seva utilització ha de respectar els drets de la persona autora. Pot ser utilitzada per a consulta o estudi personal, així com en activitats o materials d'investigació i docència en els termes establerts a l'art. 32 del Text Refós de la Llei de Propietat Intel·lectual (RDL 1/1996). Per altres utilitzacions es requereix l'autorització prèvia i expressa de la persona autora. En qualsevol cas, en la utilització dels seus continguts caldrà indicar de forma clara el nom i cognoms de la persona autora i el títol de la tesi doctoral. No s'autoritza la seva reproducció o altres formes d'explotació efectuades amb finalitats de lucre ni la seva comunicació pública des d'un lloc aliè al servei TDX. Tampoc s'autoritza la presentació del seu contingut en una finestra o marc aliè a TDX (framing). Aquesta reserva de drets afecta tant als continguts de la tesi com als seus resums i índexs.

**ADVERTENCIA.** El acceso a los contenidos de esta tesis doctoral y su utilización debe respetar los derechos de la persona autora. Puede ser utilizada para consulta o estudio personal, así como en actividades o materiales de investigación y docencia en los términos establecidos en el art. 32 del Texto Refundido de la Ley de Propiedad Intelectual (RDL 1/1996). Para otros usos se requiere la autorización previa y expresa de la persona autora. En cualquier caso, en la utilización de sus contenidos se deberá indicar de forma clara el nombre y apellidos de la persona autora y el título de la tesis doctoral. No se autoriza su reproducción u otras formas de explotación efectuadas con fines lucrativos ni su comunicación pública desde un sitio ajeno al servicio TDR. Tampoco se autoriza la presentación de su contenido en una ventana o marco ajeno a TDR (framing). Esta reserva de derechos afecta tanto al contenido de la tesis como a sus resúmenes e índices.

**WARNING.** Access to the contents of this doctoral thesis and its use must respect the rights of the author. It can be used for reference or private study, as well as research and learning activities or materials in the terms established by the 32nd article of the Spanish Consolidated Copyright Act (RDL 1/1996). Express and previous authorization of the author is required for any other uses. In any case, when using its content, full name of the author and title of the thesis must be clearly indicated. Reproduction or other forms of for profit use or public communication from outside TDX service is not allowed. Presentation of its content in a window or frame external to TDX (framing) is not authorized either. These rights affect both the content of the thesis and its abstracts and indexes.



UNIVERSITAT  
ROVIRA i VIRGILI

# Meshfree Methods: Moving Beyond the Cumulant Lattice Boltzmann Method

---

Mohsen Gorakifard

DOCTORAL THESIS  
2023





# Meshfree Methods: Moving Beyond the Cumulant Lattice Boltzmann Method

---

DOCTORAL THESIS

*Author:*

MOHSEN GORAKIFARD

*Supervisor:*

Prof. CLARA SALUEÑA

Prof. ILDEFONSO CUESTA

*A thesis submitted in fulfillment of the requirements*

*for the degree of Doctor of Philosophy*

*in the*

Departament d'Enginyeria Mecànica

UNIVERSITAT ROVIRA I VIRGILI

March 7, 2023

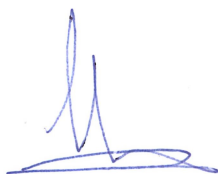


## Declaration of Authorship

I state that the present study, entitled: "**Meshfree Methods: Moving Beyond the Cumulant Lattice Boltzmann Method**" presented by MOHSEN GORAKIFARD for the award of Doctor of Philosophy, has been carried out under our supervision at the Department of Mechanical Engineering of Rovira i Virgili university.

Tarragona, March 5, 2023

Supervised by:



Prof. CLARA SALUEÑA



Prof. ILDEFONSO CUESTA

6/3/2023



UNIVERSITAT ROVIRA I VIRGILI

## *Abstract*

Departament d'Enginyeria Mecànica

Doctor of Philosophy

**Meshfree Methods: Moving Beyond the Cumulant Lattice Boltzmann Method**

by MOHSEN GORAKIFARD

To enhance the current knowledge of complex flow systems, reliable and practical methods should be evolved. One of these valuable methods is the cumulant lattice Boltzmann method (LBM), acclaimed for showing stability and robustness at high Reynolds numbers in simulations of such systems. Thus, in this dissertation, the fundamental acoustical properties of the cumulant LBM are first considered as one of the challenges of engineering problems. The propagation of point and planar acoustic waves is studied, namely the temporal decay of a standing plane wave, the spatial decay of a planar acoustic pulse, and the propagation of spherical waves. Then, as a practical example of fluid structure interaction (FSI), the coupled cumulant LBM- finite element method is applied to predict the effect of adding hairy flaps to a cylinder on the noise emission at high Reynolds numbers. The cumulant LBM provides a good agreement with theoretical, experimental and other numerical results. However, this method suffers from issues of accuracy and computational efficiency related to the use of uniform meshes. Therefore, two MFree local weak-form cumulant LB methods, the local radial point interpolation cumulant lattice Boltzmann method (LRPIC-LBM) and the meshless local Petrov-Galerkin cumulant lattice Boltzmann method (MLPGC-LBM) are suggested to overcome these shortcomings. The LB equation is divided into collision and streaming steps. The collision step is modeled by the cumulant method. In addition, the streaming step, which is naturally a pure advection equation, is discretized in time using the Lax-Wendroff scheme. It is also discretized in space, using the local radial point interpolation method (RPIM) and the meshless local Petrov-Galerkin method



(MLPG), for LRPIC-LBM and MLPGC-LBM, respectively. To substantiate the accuracy of these methods the same aeroacoustics benchmarks previously considered are again compared with those from the cumulant LBM and their respective analytical solutions. The comparisons illustrate that the LRPIC-LBM replicates the analytical results. They also show that MLPGC-LBM results are better than those of the cumulant LBM, reproducing LRPIC-LBM results with relatively shorter runtimes. Therefore, the MFree local weak-form cumulant LB methods can offer an alternative to conventional methods, without parametric dependency on the number of points per wavelength,  $N_{ppw}$ , and the resolution  $\sigma$ , while the cumulant LBM is limited by the need of mesh refinement.

## *Acknowledgements*

Throughout the writing of this dissertation I have received great support and assistance.

I would like to acknowledge my supervisors, Professor Clara Salueña and Professor Ildefonso Cuesta, whose expertise was indispensable in addressing the endless research questions and issues. Your constructive feedback and infinite patience pushed me to change the way of thinking about upcoming problems and boosted my work to the current level.

I would like to thank my colleagues at the URV Mechanical Engineering Department, specially the ECoMMFIT research group and Professor Jordi Pallarès for their wonderful collaboration. I would like to thank Lluís Vázquez for his permanent support. In addition, I would like to thank Dr. Ehsan Kian for their valuable guidance throughout my studies. Moreover, I would like to thank my visiting host, Professor Thomas Becker and Professor Ehsan Fattahi for provided me with the tools that I needed to choose the right direction and successfully complete my dissertation.

I would like to express my gratitude towards Doctoral Programme in Nanoscience, Materials and Chemical Engineering committee members, Núria Juanpere and Professor Alex Fragoso for encouraging words and thoughtful comments in doing vast bureaucracy and the jury committee members, who so generously took time out of their schedules to read the dissertation and presented valuable comments.

I would like to acknowledge the generous financial support by the Spanish Ministry of Economy, Industry and Competitiveness Research National Agency (under project DPI2016-75791-C2-1-P), by FEDER funds and by Generalitat de Catalunya - AGAUR (under project 2017 SGR 01234).

In addition, I would like to thank my parents and my brothers, Mojtaba and Ehsan for their wise counsel and sympathetic ear and for supporting me in terrible situations, standing up for me, respecting my decisions. Finally, I could not have completed this dissertation without the support of all my friends, specially members of Lab 122, (Joshua David, Mohammadjavad and Masoud Norouzi, Koorosh

Kazemi), Jordi Iglesias, Navid Jameemoghaddam, Alba Zurita and so on who provided happy distractions to rest my mind outside of my research.

# Contents

<b>Abstract</b>	<b>v</b>
<b>Acknowledgements</b>	<b>vii</b>
<b>1 Introduction</b>	<b>1</b>
1.1 Overview . . . . .	1
1.1.1 Development of the cumulant lattice Boltzmann method . . . . .	1
1.1.2 Application studies . . . . .	3
1.1.3 Improving weaknesses . . . . .	5
1.2 Thesis goals and structure . . . . .	7
1.2.1 Related Contributions . . . . .	9
<b>2 The cumulant LBM</b>	<b>11</b>
2.1 Introduction . . . . .	12
2.2 Methodology . . . . .	14
2.2.1 Cumulant lattice Boltzmann . . . . .	15
2.2.2 Structural analysis . . . . .	17
2.2.3 Coupling scheme . . . . .	20
2.2.4 The wave equation . . . . .	24
2.3 Results and Discussion . . . . .	25
2.3.1 Acoustic properties of the cumulant lattice Boltzmann method	25
Planar standing wave . . . . .	25
Planar pulse wave . . . . .	28
2.3.2 Spherical wave . . . . .	31
Acoustic pulse . . . . .	31
Acoustic point source . . . . .	33
2.3.3 Splitter plates attached to a cylinder looking like hair (SPCH) . . . . .	34

2.4	Conclusion . . . . .	41
<b>3</b>	<b>The local radial point interpolation cumulant LBM</b>	<b>45</b>
3.1	Introduction . . . . .	46
3.2	The lattice Boltzmann method . . . . .	49
3.2.1	Collision Step . . . . .	49
3.2.2	Streaming Step . . . . .	50
	MFree shape function construction – Radial point interpolation shape functions . . . . .	50
	Semi-discrete formulation – Time discretization . . . . .	52
	Semi-discrete formulation – Space discretization . . . . .	52
3.3	Results and Discussion . . . . .	54
3.3.1	Planar standing wave . . . . .	56
3.3.2	Planar pulse wave . . . . .	59
3.4	Conclusions . . . . .	63
<b>4</b>	<b>The meshless local Petrov-Galerkin cumulant LBM</b>	<b>65</b>
4.1	Introduction . . . . .	66
4.2	Lattice Boltzmann method . . . . .	67
4.2.1	Collision Step . . . . .	67
4.2.2	Streaming Step . . . . .	67
	Mfree shape function construction - Moving least squares shape functions . . . . .	68
	Semi-discrete formulation - Time discretization . . . . .	70
	Semi-discrete formulation - Space discretization . . . . .	70
4.3	Results and Discussion . . . . .	72
4.3.1	Planar standing wave . . . . .	72
4.3.2	Planar pulse wave . . . . .	78
4.3.3	Acoustic pulse . . . . .	80
4.3.4	Acoustic point source . . . . .	83
4.4	Conclusions . . . . .	84
<b>5</b>	<b>Conclusions</b>	<b>87</b>

**References**



# List of Figures

1.1	Lattice arrangement for D2Q9. . . . .	3
2.1	Two possibilities for the position of the structure inside the fluid domain. . . . .	21
2.2	Force calculation from stress. . . . .	23
2.3	Active (fluid) and inactive (structural) nodes in the LBM grid. . . . .	23
2.4	Coupling algorithm. . . . .	24
2.5	Non-dimensional acoustic pressure $p'/A$ vs. time history [s] at (0,0) for the planar standing wave considering two different choices for the bulk viscosity: Case 1 where the relaxation time for the bulk viscosity is chosen based on equation (2.8)) and Case 2 where the value of the relaxation time for the bulk viscosity is chosen as 1. . . . .	27
2.6	Non-dimensional acoustic pressure $p'/A$ vs. time history [s] at (0,0) for the planar standing wave. . . . .	28
2.7	Non-dimensional acoustic pressure $p'/A$ vs. time history [s] at origin (—), 0.056m (— · —) and 0.128m (— —) from the reference position, for the planar pulse wave. . . . .	29
2.8	Numerical error of the specified acoustic properties for the planar pulse wave as functions of the angular frequency [Hz] ( $\nu = 2.36 \times 10^{-2} \text{m}^2/\text{s}$ and different resolution). . . . .	30
2.9	Numerical error of the dissipation rate [Np/m] for the planar pulse wave as a function of angular frequency [Hz] (for $\nu = 2.35 \times 10^{-4} \text{m}^2/\text{s}$ and resolution $\Delta x = 0.004\text{m}$ ). . . . .	30
2.10	The comparison of the analytical and numerical values of the perturbation $\rho'[\text{kg}/\text{m}^3]$ . . . . .	32



2.11 Comparison of the stationary analytical and numerical values of the perturbation $\rho'$ [kg/m <sup>3</sup> ] for the cumulant LBM. . . . .	34
2.12 Comparison of the analytical and numerical values of the perturbation $\rho'$ [kg/m <sup>3</sup> ] for the BGK LBM. . . . .	35
2.13 Computational domain of the cases studied for the SPCH problem. . .	37
2.14 Spread of the vorticity [1/ $\Delta t$ ] in the wake behind a cylinder for Cases 1-3. . . . .	39
2.15 Displacement [m] vs. time [s] . . . . .	40
2.16 State of the flaps for eight selected times. . . . .	41
2.17 Spread of the vorticity [1/ $\Delta t$ ] in the wake behind twin cylinders for Cases 4-6. . . . .	42
2.18 Sound pressure level [dB] as a function of frequency [Hz]. . . . .	43
2.19 Sound pressure level [dB] as a function of frequency [Hz] for single cylinder case . . . . .	43
3.1 Nodal arrangement for the propagation of planar acoustic waves in LRPIC-LBM simulations. . . . .	55
3.2 Acoustic pressure [ $\frac{kg}{\Delta x \Delta t^2}$ ] versus time step [ $\Delta t$ ] for $\nu = 1.0 \times 10^{-2}$ [ $\frac{\Delta x^2}{\Delta t}$ ] with $N_{ppw} = 12$ points per wavelength. . . . .	57
3.3 Acoustic pressure [ $\frac{kg}{\Delta x \Delta t^2}$ ] versus time step [ $\Delta t$ ] for $\nu = 1.0 \times 10^{-4}$ [ $\frac{\Delta x^2}{\Delta t}$ ] with $N_{ppw} = 12$ points per wavelength. . . . .	58
3.4 Acoustic pressure [ $\frac{kg}{\Delta x \Delta t^2}$ ] versus time step [ $\Delta t$ ] for $\nu = 1.0 \times 10^{-2}$ [ $\frac{\Delta x^2}{\Delta t}$ ] with $N_{ppw} = 4$ points per wavelength with $\Delta t = 0.25$ . . . . .	58
3.5 Acoustic pressure [ $\frac{kg}{\Delta x \Delta t^2}$ ] versus time step [ $\Delta t$ ] for $\nu = 1.0 \times 10^{-2}$ [ $\frac{\Delta x^2}{\Delta t}$ ] with $N_{ppw} = 4$ points per wavelength with $\Delta t = 0.1$ . . . . .	59
3.6 Acoustic pressure [ $\frac{kg}{\Delta x \Delta t^2}$ ] versus time step [ $\Delta t$ ] for $\nu = 1.0 \times 10^{-2}$ [ $\frac{\Delta x^2}{\Delta t}$ ] with $N_{ppw} = 12$ points per wavelength with irregular nodal distributions. . . . .	59
3.7 Acoustic pressure [ $\frac{kg}{\Delta x \Delta t^2}$ ] versus time step [ $\Delta t$ ] for $\nu = 1.0 \times 10^{-2}$ [ $\frac{\Delta x^2}{\Delta t}$ ] with $\sigma = 0.1$ : the cumulant LBM (dashed red line), LRPIC-LBM (solid black line). . . . .	61

3.8	Acoustic pressure $[\frac{kg}{\Delta x \Delta t^2}]$ versus time step $[\Delta t]$ for $\nu = 1.0 \times 10^{-4} [\frac{\Delta x^2}{\Delta t}]$ with $\sigma = 0.1$ : the cumulant LBM (dashed red line), LRPIC-LBM (solid black line). . . . .	61
3.9	Acoustic pressure $[\frac{kg}{\Delta x \Delta t^2}]$ versus time step $[\Delta t]$ for $\nu = 1.0 \times 10^{-2} [\frac{\Delta x^2}{\Delta t}]$ with $\sigma = 0.06$ : the cumulant LBM (dashed red line), LRPIC-LBM (solid black line). . . . .	62
3.10	The ratio $\hat{p}'(x, \omega) / \hat{p}'(x, 0)$ as a function of angular frequency $[\frac{1}{\Delta t}]$ for the analytical solution, the cumulant LB and the LRPIC-LB methods. . . . .	62
3.11	Acoustic pressure $[\frac{kg}{\Delta x \Delta t^2}]$ versus time step $[\Delta t]$ for $\nu = 1.0 \times 10^{-2} [\frac{\Delta x^2}{\Delta t}]$ with $\sigma = 0.1$ considering irregular nodal distributions: the cumulant LBM (dashed blue line), LRPIC-LBM (solid black line). . . . .	63
4.1	Nodal arrangement for the propagation of planar acoustic waves in MLPGC-LBM simulations. . . . .	73
4.2	Acoustic pressure $[\frac{kg}{\Delta x \Delta t^2}]$ versus time step $[\Delta t]$ for $\nu = 1.0 \times 10^{-2} [\frac{\Delta x^2}{\Delta t}]$ with $N_{ppw} = 14$ points per wavelength. . . . .	75
4.3	Acoustic pressure $[\frac{kg}{\Delta x \Delta t^2}]$ versus time step $[\Delta t]$ for $\nu = 1.0 \times 10^{-4} [\frac{\Delta x^2}{\Delta t}]$ with $N_{ppw} = 14$ points per wavelength. . . . .	75
4.4	Acoustic pressure $[\frac{kg}{\Delta x \Delta t^2}]$ versus time step $[\Delta t]$ for $\nu = 1.0 \times 10^{-2} [\frac{\Delta x^2}{\Delta t}]$ with $N_{ppw} = 4$ points per wavelength and $\Delta t = 0.1$ . . . . .	76
4.5	Acoustic pressure $[\frac{kg}{\Delta x \Delta t^2}]$ versus time step $[\Delta t]$ for $\nu = 1.0 \times 10^{-2} [\frac{\Delta x^2}{\Delta t}]$ with $N_{ppw} = 4$ points per wavelength with $\Delta t = 0.1$ . . . . .	77
4.6	Acoustic pressure $[\frac{kg}{\Delta x \Delta t^2}]$ versus time step $[\Delta t]$ for $\nu = 1.0 \times 10^{-2} [\frac{\Delta x^2}{\Delta t}]$ with $N_{ppw} = 14$ points per wavelength with irregular nodal distributions. . . . .	77
4.7	Acoustic pressure $[\frac{kg}{\Delta x \Delta t^2}]$ versus time step $[\Delta t]$ for $\nu = 1.0 \times 10^{-2} [\frac{\Delta x^2}{\Delta t}]$ with $\sigma = 0.11$ : cumulant LBM (dashed red line), MLPGC-LBM (m=6) (solid black line), and MLPGC-LBM (m=3) (blue pentagram). . . . .	79
4.8	Acoustic pressure $[\frac{kg}{\Delta x \Delta t^2}]$ versus time step $[\Delta t]$ for $\nu = 1.0 \times 10^{-2} [\frac{\Delta x^2}{\Delta t}]$ with $\sigma = 0.06$ : cumulant LBM (dashed red line), LRPIC-LBM (solid black line), and MLPGC-LBM (m=3) (blue pentagram). . . . .	80

4.9	Acoustic pressure $[\frac{kg}{\Delta x \Delta t^2}]$ versus time step $[\Delta t]$ for $\nu = 1.0 \times 10^{-2} [\frac{\Delta x^2}{\Delta t}]$ with $\sigma = 0.11$ : cumulant LBM (dashed red line), MLPGC-LBM (m=6) (solid black line), and MLPGC-LBM (m=3) (blue pentagram with blue line). . . . .	80
4.10	Propagation of the density perturbation through the domain for $\nu = 1.0 \times 10^{-2} [\frac{\Delta x^2}{\Delta t}]$ with $\sigma = 0.11$ : cumulant LBM (solid black line), MLPGC-LBM (m=6) (dashed red line). . . . .	81
4.11	Propagation of the density perturbation through the domain for $\nu = 1.0 \times 10^{-2} [\frac{\Delta x^2}{\Delta t}]$ with $\sigma = 0.04$ : cumulant LBM (solid black line), MLPGC-LBM (m=6) (dashed red line). . . . .	82
4.12	Propagation of the density perturbation through the irregular nodal distribution for $\nu = 1.0 \times 10^{-2} [\frac{\Delta x^2}{\Delta t}]$ with $\sigma = 0.04$ : cumulant LBM (solid black line), MLPGC-LBM (m=6) (dashed red line). . . . .	82
4.13	Comparison of the values of the density perturbation with a period $T = 20 [\Delta t]$ . . . . .	83
4.14	Comparison of the values of the density perturbation with a period $T = 10 [\Delta t]$ . . . . .	84
4.15	Comparison of the values of the density perturbation with a period $T = 20 [\Delta t]$ propagating through an irregular nodal distribution. . . . .	85

# List of Tables

2.1	Parameters for the planar standing wave . . . . .	26
2.2	Relative numerical error of the specified acoustic properties as a function of the non-dimensional wave-number ( $k\Delta x$ ) for the planar standing wave. . . . .	28
2.3	Parameters for the planar pulse wave . . . . .	29
2.4	Parameters for the pseudo-2D acoustic pulse . . . . .	32
2.5	Parameters for the acoustic point source . . . . .	33
2.6	Cases studied for the SPCH ( $r$ is the radius of the cylinder) . . . . .	36
2.7	Parameters for the SPCH study . . . . .	36
2.8	The Strouhal number for Case 1 . . . . .	37
2.9	The Strouhal number for Case 4 . . . . .	38
3.1	Parameters for the planar standing wave . . . . .	56
3.2	Parameters for the planar pulse wave . . . . .	60
4.1	Parameters for the planar standing wave . . . . .	74
4.2	Parameters for the planar pulse wave . . . . .	78
4.3	Parameters for the 2D acoustic pulse . . . . .	81
4.4	Parameters for the acoustic point source . . . . .	83



# List of Abbreviations

<b>BGK</b>	<b>B</b> hatnagar <b>G</b> ross <b>K</b> rook
<b>CAA</b>	<b>C</b> omputational <b>A</b> eroacoustics
<b>CFD</b>	<b>C</b> omputational <b>F</b> luid <b>D</b> ynamics
<b>CLBM</b>	<b>C</b> ascade <b>L</b> attice <b>B</b> oltzmann <b>M</b> odel
<b>DRP</b>	<b>D</b> ispersion <b>R</b> elation <b>P</b> reserving
<b>FEM</b>	<b>F</b> inite <b>E</b> lement <b>M</b> ethod
<b>FSI</b>	<b>F</b> luid <b>S</b> tructure <b>I</b> nteraction
<b>GODRP</b>	<b>G</b> rid <b>O</b> ptimized <b>D</b> ispersion <b>R</b> elation <b>P</b> reserving
<b>IS-LBM</b>	<b>I</b> nterpolation <b>S</b> upplemented <b>L</b> attice <b>B</b> oltzmann <b>M</b> ethod
<b>LBM</b>	<b>L</b> attice <b>B</b> oltzmann <b>M</b> ethod
<b>LBM-rrBGK</b>	<b>L</b> attice <b>B</b> oltzmann <b>M</b> ethod recursive regularized <b>B</b> hatnagar <b>G</b> ross <b>K</b> rook
<b>LPIM</b>	<b>L</b> ocal <b>P</b> oint <b>I</b> nterpolation <b>M</b> ethod
<b>LRPIC-LBM</b>	<b>L</b> ocal <b>R</b> radial <b>P</b> oint <b>I</b> nterpolation <b>C</b> umulant <b>L</b> attice <b>B</b> oltzmann <b>M</b> ethod
<b>LRPIM</b>	<b>L</b> ocal <b>R</b> adial <b>P</b> oint <b>I</b> nterpolation <b>M</b> ethod
<b>MLPG</b>	<b>M</b> eshless <b>L</b> ocal <b>P</b> etrov <b>G</b> alerkin
<b>MLPGC-LBM</b>	<b>M</b> eshless <b>L</b> ocal <b>P</b> etrov <b>G</b> alerkin <b>C</b> umulant <b>L</b> attice <b>B</b> oltzmann <b>M</b> ethod
<b>MLS</b>	<b>M</b> oving <b>L</b> east <b>S</b> quares
<b>MQ</b>	<b>M</b> ulti <b>Q</b> adrics
<b>MRT</b>	<b>M</b> ulti <b>R</b> elaxation <b>T</b> imes
<b>MWR</b>	<b>M</b> ethod <b>W</b> eighted <b>R</b> esiduals
<b>NREL</b>	<b>N</b> ational <b>R</b> enewable <b>E</b> nergy <b>L</b> aboratory
<b>NWTC</b>	<b>N</b> ational <b>W</b> ind <b>T</b> echnology <b>C</b> enter
<b>PDF</b>	<b>P</b> robability <b>D</b> ensity <b>F</b> unction
<b>RBF</b>	<b>R</b> adial <b>B</b> asis <b>F</b> unctions
<b>SPCH</b>	<b>S</b> plitter <b>P</b> lates attached to the <b>C</b> ylinder base and look like <b>H</b> air



*I am dedicating this thesis to my beloved people my **Grandma,**  
**Mom, and Dad.** Love you so much. ♡♡♡*





## Chapter 1

# Introduction

### 1.1 Overview

#### 1.1.1 Development of the cumulant lattice Boltzmann method

The lattice Boltzmann method (LBM), an explicit time marching scheme for a general class of advection-diffusion models, has recently been proposed as a new computational fluid dynamic method (CFD) (1). It evolved from the field of cellular automata, notably lattice gases. The first idea of the lattice gas goes back to 1973 (2). However, a lattice gas that could correctly simulate fluid flow was presented in 1986 (3). To overcome some of the drawbacks of lattice gases, the lattice Boltzmann method was developed (4). Even though traditional CFD methods discretize and solve the macroscopic equations of fluid mechanics, the lattice Boltzmann method, which is a discretization of the Boltzmann equation, models the weakly compressible Navier-Stokes equations in the mesoscopic limit and a simpler form (5). The basic idea is that flow motion is modeled by a discrete momentum distribution function, to transfer momentum and energy through particle streaming and billiard-like particle collision on a Cartesian grid, at each time step (6). Depending on the number  $q$  of directions or velocities in the momentum space for the moving particle, and dimension  $d=2$  or  $3$  for the lattice, a  $DdQq$  stencil can be defined (7). In our simulations the  $D2Q9$  lattice model is chosen for efficiency and accuracy reasons (Figure 1.1). The LBM consists of collision and streaming parts. For each node at each time step, the local distribution function relaxes toward local equilibrium in the collision step, then it propagates to the neighboring nodes in the streaming step. Both of these steps play key roles in the accuracy and the stability of the method (8). With

the proper collision operator, simulations at large Reynolds numbers can be stable. Bhatnagar, Gross and Krook (BGK) presented a simplified collision operator (9) by using the local distribution function and the local equilibrium distribution function, to obtain a new local distribution. It should be noted that the BGK method, with only one relaxation parameter, is not stable at high Reynolds numbers. In general, the LBM is slightly compressible having a finite bulk viscosity which is a function of the relaxation rate. The bulk viscosity affects pressure waves (10), and with a single relaxation rate for both the bulk and shear viscosities, the BGK LBM can not capture pressure waves at high Reynolds numbers. To overcome this limitation, the LBM model with different relaxation parameters (the so-called multi-relaxation times (MRT) method) was developed (1). It utilizes a linear transformation into an equivalent moment space to increase stability. These moments are related to physical quantities. Basically, relaxation parameters are determined according to the physical parameters and system stability conditions. These moments are transformed back into the original space after the collision step. Although The MRT LBM is more stable than the previous method, it is not fully applicable to engineering modeling, since the moments are set based on the rest frame of reference which is relaxed on its own. Thus, Galilean invariant problems are generated as a main reason for instability. To rectify such problems, the cascade lattice Boltzmann model (CLBM) was proposed by Geier (10, 11). The idea of CLBM is to perform the collision process in a frame of reference shifted by the macroscopic velocity. Considering the moving-frame-of-reference “central moments” instead of the moments on the rest frame of reference or “raw moments”, could solve the violation of Galilean invariant problems. Central moments of a specific order are equal to the lower or same order raw moments. Therefore, lower-order raw moments have impact on higher-order central moments. In addition, higher-order central moments are dependent on the lower ones which cause a structured sequential calculation of relaxation rates in the CLBM. To improve the CLBM, the cumulant LBM was suggested where higher order moments are independent of lower order moments. Seeger presented a cumulant method for solving the Boltzmann equation (12, 13). Geier used the cumulant method for solving the LBM (14). This method is widely attracting the researchers’ interest.

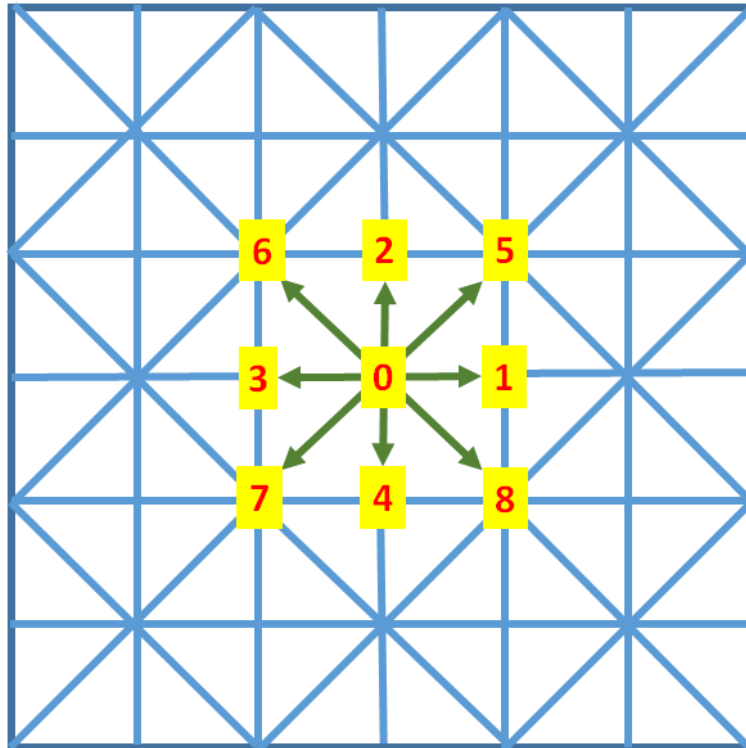


FIGURE 1.1: Lattice arrangement for D2Q9.

### 1.1.2 Application studies

To have a better estimation of the capability of the cumulant LBM to advance the fundamental knowledge of complex flow systems found in engineering problems, tracking instabilities and considering the sensitivity of the method is crucial. Two simulation classes which show such instabilities can be sound propagation and fluid structure interaction.

To begin with, the propagation of sound, as one of the challenging issues in engineering and technology (15, 16), not only affects many industries such as transportation, basically limiting engine operation, causing discomfort to crews, and polluting the environment, but also makes many simulations of engineering system (such as wind turbines) computationally expensive, particularly for the need of an enormous number of grid points or cells, and long enough time samples (17). Researchers and centers such as the National Renewable Energy Laboratory (NREL) and the National Wind Technology Center (NWTC) have initiated programs (18) to establish efficient and appropriate computational aeroacoustic (CAA) implementations. Various schemes have been devised in the field of computational aeroacoustics. Tam (19)

and Wells et al. (20) presented compact and non-compact optimized schemes like the high-order compact difference scheme (21) and the dispersion-relation-preserving (DRP) scheme (22). Cheong et al. proposed grid-optimized dispersion-relation-preserving (GODRP) schemes for curvilinear problems (23). Hybrid methods were then developed to reduce the huge cost of CAA simulations. These methods use two sets of equations, for the flow and for the acoustic disturbance field (24). However, the direct numerical simulations of aerostatics are complicated due to the small ratio between sound pressure and pressure variation as a whole, the spreading of acoustic fields over a large area, and the time-consuming nature of the above traditional methods (25). For example, the direct numerical simulation of waves using Navier-Stokes equations requires schemes of fifth-order accuracy in space and fourth order accuracy in time (26, 27). Therefore, the lattice Boltzmann methods were proposed as an alternative to the above schemes for simulating sound wave propagation. Buick et al. (28) and Dellar et al. (29) studied sound wave propagation using LBM and achieved acceptable results. Bres et al. (30) analyzed the dissipation and dispersion of acoustic waves using the BGK-LBM. Furthermore, a regularized method for the BGK-LBM (31) and the recursive and regularized LBM (LBM-rrBGK) (32, 33) have been developed to model wave propagation.

In addition, most physical phenomena are not limited to fluids and occur in different phases (fluid or solid). As practical cases of such phenomena, self-adaptive devices used to control the flow and sound side effects can be highlighted. These devices manipulating vortex shedding perform a critical role in many industries. As an illustration, splitter plates have been known as one of the effective ways for controlling vortex shedding (34, 35). Recently, several investigations have been undertaken on the effect an splitter plate on the flow pattern behind a cylinder (36–38). Brucker et al. proposed the addition of flexible flaps and studied experimentally its effect on the flow beyond a cylinder and the alteration of the shedding cycle (39, 40). They also showed that the motion pattern of the flaps changes to a wavy shape with an increase of the amplitude beyond some specific Reynolds number, which resulted in the decrease of the vortices transversal distance from the center line, reduction of structural vibrations, and sound generation. Due to the fact that in such phenomena, a fluid solver has to be coupled with a solid solver and the coupling

process of the LB methods with the finite element method is relatively straightforward, the LB methods have high potential for modeling fluid structure interaction (FSI) problems. Thus, splitter plates attached to a cylinder that look like hair (SPCH) as one of the self-adaptive devices to control the actual flow conditions, is a really hard benchmark problem to study the stability and capabilities of these methods.

To sum up, these examples could effectively show the capability of the cumulant LBM to simulate sound wave propagation by calculating the deviation from analytical results, notably the dissipation and dispersion errors. They could also assess the effects of SPCH on the noise past bodies at high velocities, particularly, the acoustic damping effect of such flaps on sound propagation through interactions among acoustic waves, solid walls and shear layers.

### 1.1.3 Improving weaknesses

In general, the implementation and parallelization of LB methods is efficient and straightforward for simulating multiphase/component flows, complex fluid flows, and flows with complicated geometries such as porous media, thermal flows, and turbulent flows. They dramatically save time and efforts as compared to traditional CFD methods.

However the lattice uniformity, generated from the lattice symmetry of the velocity stencil, limits the LBM when modeling accurately and efficiently non-uniform mesh problems (41) such as those with irregular boundaries. Even though grid refinement could improve accuracy substantially (42), this approach raises new challenges such as higher computational costs and the appearance of additional perturbations in acoustical simulations (43). To overcome such shortcomings, conventional non-uniform LB methods have been developed including: Interpolation-supplemented LBM (44, 45), combinations of LBM with finite difference methods (46), finite volume methods (47–49), finite element methods (50–52), and Taylor-series expansion and least-squares-based lattice Boltzmann methods (53, 54).

However, the above methods have the shortcomings of all the numerical methods that depend on meshes in a predefined manner, such as high cost in creating the mesh, low accuracy of stress calculations, and limitations in simulations of problems with discontinuities or moving boundaries. Thus, the concept of meshless methods

has been evolved, which based on Liu definition is “a method using a set of algebraic equations for the entire problem domain while ignoring a predefined mesh for the discretization”. It means these methods scatter a set of nodes inside and at the boundaries of the domain, which results in a system of algebraic equations to interpolate or approximate the variables.

The evolution of some MFree methods derived toward collocation methods(55, 56), vortex methods (57, 58), finite difference methods with arbitrary grids (59, 60), and the Smoothed Particle Hydrodynamics method proposed for astrophysical modeling, especially exploding stars and dust clouds (61, 62). One way to categorize MFree methods is based on the formulation procedure used, including weak forms, strong forms, and weak-strong forms. In general, the weak forms give a set of algebraic equations by a numerical integration process. Moreover, these forms have achieved remarkable progress as compared with the other categories, due to their robustness and focus on the finite element method. Therefore, a wide group of this type of MFree methods has been developed such as the diffuse element method (63), the element-free Galerkin method (64, 65), the reproducing kernel particle method (66), the point interpolation methods (67), the meshless local Petrov-Galerkin method (MLPG) (68), the boundary node method (69), the boundary point interpolation method (70), and others.

The possibility of using Mfree methods in LBM has resulted in acceptable outcomes (71–74). However, this idea is still at an early stage of development and must be improved in order to address challenging issues common in complex simulations. As an illustration, the cited studies have used the standard Bhatnagar-Gross-Krook (BGK) scheme in the collision part, which suffers from instability at high Reynolds numbers and low viscosities, and violation of the principle of Galilean invariance (6). Thus, replacing the BGK collision scheme by the more stable cumulant LBM (5, 75) could provide better results. For this purpose, the local radial point interpolation cumulant lattice Boltzmann method (LRPIC-LBM) (76) has been developed. Moreover, the efficiency of LRPIC-LBM may increase by using MLPG in the Mfree part, since the moving least squares (MLS) shape functions used in MLPG need less computational resources than the RPIM shape functions used in LRPIM. This idea resulted in the meshless local Petrov-Galerkin cumulant LB method (MLPGC-LBM)

(77).

## 1.2 Thesis goals and structure

The title of the research project is “Meshfree Methods: Moving Beyond the Cumulant Lattice Boltzmann Method”. The main objective of this project was to develop a valuable tool that could advance the fundamental knowledge of complex flow systems and areas of knowledge that have been poorly studied. The project had four main goals. The first aim of this work was to be familiar with one of the newest LB methods, the cumulant lattice Boltzmann method, which could meet our main purpose and simulate such systems with a really vast and extensive scope. The second goal of this development was to investigate the weaknesses and strengths of the cumulant LBM and improve the current understanding of the propagation of sound waves in LB simulations as one of the challenges in complex flow engineering problems. In addition, most physical phenomena are not limited to fluids but occur in different phases (fluid or solid). Therefore, a fluid solver often has to be coupled with a solid solver. As a third aim, the Cumulant LBM was coupled with the finite element method and its stability was studied, as well as its behavior in dealing with instability and noise emitting processes propagating through the domain. Finally, the fourth goal of this study was to develop new methods to improve the current cumulant LBM, thus overcoming the issues of accuracy and computational efficiency that arise due to the use of uniform meshes. Thus, two new MFree local weak-form cumulant LB methods: the local radial point interpolation cumulant lattice Boltzmann method and the meshless local Petrov-Galerkin cumulant lattice Boltzmann method were developed and analyzed.

This thesis is divided into two main parts. Part one discusses the cumulant lattice Boltzmann method and its application to aeroacoustics and fluid structure interaction. Part two proposes substitute methods to improve its weaknesses. Thus, the thesis is arranged in the following chapters:

**Chapter 1** This chapter.



**Chapter 2** studies the fundamental acoustical properties of the cumulant lattice Boltzmann method. Point and planar acoustic waves are considered including the temporal decay of a standing plane wave, the spatial decay of a planar acoustic pulse, and the propagation of spherical waves. In addition, the cumulant LBM as a fluid flow solver, coupled with a finite element structural mechanics solver, is used to study the effects of splitter plates attached to a cylinder looking like hair (SPCH). The noise generated by one and two circular cylinders supplied with such flaps is studied at high Reynolds numbers, as an example of fluid structure interaction (FSI) application.

**Chapter 3** studies propagation of planar acoustic waves, including the temporal decay of a standing plane wave and the spatial decay of a planar acoustic pulse of Gaussian shape, modeled by the local radial point interpolation cumulant lattice Boltzmann method (LRPIC-LBM). It presents the deviation from theoretical results and tries to determine whether this method might be useful as a substitute for the cumulant lattice Boltzmann method in engineering problems.

**Chapter 4** studies the propagation of point and planar acoustic waves, including the temporal decay of a standing plane wave, the spatial decay of a planar acoustic pulse of Gaussian shape, and the propagation of spherical waves by means of the meshless local Petrov-Galerkin cumulant lattice Boltzmann method (MLPG-LBM). The errors and deviations from the analytical solutions are analyzed critically and compared with the results obtained with the regular cumulant lattice Boltzmann method as well as the LRPIC-LBM of chapter 3. The advantages and disadvantages of the method are discussed in view of the results. This chapter tries to conclude whether this method might be useful as a substitute for the cumulant lattice Boltzmann method in engineering problems.

**Chapter 5** collects the remarks obtained in the previous chapters and draws a brief conclusion to the thesis.

### 1.2.1 Related Contributions

To complete the PhD project, the following attainments were fulfilled.

- **Journal articles**

- Gorakifard, Mohsen; Cuesta, Ildefonso; Salueña, Clara; Kian Far, Ehsan. (2021) “Acoustic wave propagation and its application to fluid structure interaction using the Cumulant Lattice Boltzmann Method”, *Computers & Mathematics with Applications*. 87. 91-106. 10.1016/j.camwa.2021.02.011.
- Gorakifard, Mohsen; Salueña, Clara; Cuesta, Ildefonso; Kian Far, Ehsan. (2021) “Analysis of Aeroacoustic Properties of the Local Radial Point Interpolation Cumulant Lattice Boltzmann Method”, *Energies* 14. 1443. 10.3390/en14051443.
- Gorakifard, Mohsen; Salueña, Clara; Cuesta, Ildefonso; Kian Far, Ehsan. (2022) “The Meshless Local Petrov-Galerkin Cumulant Lattice Boltzmann Method: Strengths and Weaknesses in Aeroacoustic Analysis”, *Acta Mech* 233, 1467–1483.

- **Conference contributions**

- Gorakifard, Mohsen; Cuesta, Ildefonso; Salueña, Clara; Kian Far, Ehsan. (2019) “Acoustical analysis of fluid structure interaction using the Cumulant lattice Boltzmann method”, 16th International Conference for Mesoscopic Methods in Engineering and Science, Edinburgh, UK.
- Gorakifard, Mohsen; Salueña, Clara; Cuesta, Ildefonso; Kian Far, Ehsan. (2019) “Simulation of Flow over a ECoMMFiT Logo using Cumulant Lattice Boltzmann Method”, 16th Doctoral Day in Nanoscience, Materials and Chemical Engineering, Universitat Rovira Virgili, Spain.
- Gorakifard, Mohsen; Salueña, Clara; Cuesta, Ildefonso; Kian Far, Ehsan. (2022) “Fluid software based on interactive LBM-GPU”, 17th Doctoral Day in Nanoscience, Materials and Chemical Engineering, Universitat Rovira Virgili, Spain.

- Gorakifard, Mohsen; Salueña, Clara; Cuesta, Ildefonso; Kian Far, Ehsan. (2022) “MFree local weak-form cumulant lattice boltzmann methods: Aeroacoustic Consideration”, *Tecnicística*, Elche, Spain (Invited conference).

- **Oral presentations**

- Gorakifard, Mohsen. (2018) “Jet flow control applied to a projectile”, *Ecommfit*, URV.
- Gorakifard, Mohsen. (2021) “Local radial point interpolation cumulant Lattice Boltzmann Method”, *Ecommfit*, URV.
- Gorakifard, Mohsen. (2021) “Nit Europea de la Recerca a Tarragona: ¿Lava lamps¿”, URV.

## Chapter 2

# The cumulant LBM

Splitter plates attached to a cylinder looking like hair (SPCH) is one of the self-adaptive devices used to control actual flow conditions, which in turn interact with Aeolian tones constituting a typical case of study in engineering industries. The direct numerical simulation of the sound waves stimulated by such devices is a complicated task due to the small levels of sound pressure and the time-consuming existing solvers. However, the cumulant lattice Boltzmann method (LBM) provides stability and robustness at high Reynolds numbers and carries out these simulations satisfactorily. First, the fundamental acoustical properties of the cumulant LBM are studied in this work. Propagation of point and planar acoustic waves is considered including the temporal decay of a standing plane wave, the spatial decay of a planar acoustic pulse, and the propagation of spherical waves. Then, the cumulant LBM as a fluid flow solver is coupled with a finite element structural mechanics solver to predict the effects of SPCH on the noise generated by cylinders at high Reynolds numbers as a practical fluid structure interaction (FSI) application. The spectral modification and possible acoustic damping impact of such flaps, plus the sound propagation from one and two circular cylinders are studied. A comparison of the theoretical and numerical results shows a reasonable capability of the cumulant LBM to predict acoustical events with small errors in dissipation and dispersion. Furthermore, the results show that SPCH alter the phase of the vortex shedding cycle and decrease the transversal distance from the center line of the shed vortices. Flaps, thus, control the wake generated past a cylinder and have an effective impact on reducing sound generation.

## 2.1 Introduction

Noise reduction is an important part of engineering design in transportation industries such as aircraft, high speed trains, automobiles, and so on. In general, noise limits engine operation, disturbs passengers and operators, and pollutes the environment. As a result, the understanding and controlling of noise is fundamental.

A typical case of aerodynamic noise is the Aeolian tone, named after the god of winds Aeolus in the Hellenic mythology. The first observations of Aeolian tones (78–80) were made in sound generated from bluff bodies like cylinders immersed in a flow (81, 82). Researchers believe that the hydrodynamic instability of the wake behind a cylinder after a specific critical Reynolds number, results in sound with strong tonal components based on the vortex shedding frequency. Strouhal's studies on the existence of these vortex shedding tones (83) lead to the non-dimensional Strouhal number, which is the relation between the frequency of the vortex shedding tone, the characteristic length, and the free stream velocity.

Hardin et al. (84) calculated the sound generated by an incompressible and time dependent flow over a cylinder at low Reynolds numbers. Cox et al. (85) studied the tonal noise generated from a circular cylinder for a wide range of Reynolds numbers, and compared with experimental studies. In addition, Inoue et al. (86) simulated the sound generated by two squares at a Mach number equal of 0.2 using direct solution of the 2D unsteady compressible Navier-Stokes equations. Tam (87) and Wells et al. (20) studied different popular numerical schemes in the the field of computational aeroacoustics (CAA). They presented compact and non-compact optimized schemes which are mostly based on linear wave propagation, such as the high-order compact difference schemes (21, 88) and the dispersion-relation-preserving (DRP) scheme (22). Among these methods, the DRP scheme is the most simple thanks to the use of symmetric finite differences on uniform Cartesian grids. To simulate curvilinear problems in aeroacoustics, grid-optimized dispersion-relation-preserving (GODRP) schemes were developed (23). However, the prediction of aerodynamic noise is burdensome because of the huge cost of CAA simulations, which resulted in developing hybrid methods. Hybrid methods use two sets of equations, one for the flow and another one for the acoustic disturbance field.

To control the flow and sound side effects, self-adaptive devices can be utilized. The devices for manipulating vortex shedding play a critical role in many engineering problems. As an illustration, splitter plates have been known as one of the effective ways for controlling vortex shedding (34, 35). Recently, several investigations have been carried out on the effect of an attached rigid splitter plate on the flow pattern behind a cylinder (36–38). They showed that the length of the splitter plate strongly influences the character of the vortex shedding for different fluid flow regimes. Mazellier et al. (89) studied flexible membranes, similar to bird's feathers, to control the flow behind a square. Brucker et al. experimentally studied the effects of flexible flaps on the flow around a cylinder. They showed that flaps can alter the shedding cycle (39, 40). In addition, the motion pattern of the flaps changes to a wavy shape when the amplitude is increased beyond some specific Reynolds. As a result, the vortices transversal distance from the center line, structural vibrations, and sound generation decrease.

The direct numerical simulation of sound waves stimulated by controlling devices is complicated since the sound pressure is much smaller than the whole pressure variation. In addition, the acoustic field spreads in large regions and this is a time-consuming process. For example, the direct numerical simulation of sound waves based on Navier-Stokes equations needs schemes of fifth-order accuracy in space and fourth-order accuracy in time (26, 90, 91). On the other hand, the lattice Boltzmann method (LBM) is a new and reliable method of computational fluid dynamics (CFD) which has been developed from the lattice gas method and can be used as an alternative to simulate sound wave propagation. Furthermore, the coupling of the LB method with the finite element method is relatively straightforward. Generally, the LB method, an explicit time marching scheme, is used for a broad category of advection-diffusion problems (1).

The LBM has been widely used in many applications in the field of acoustics. Buick et al. (28) and Dellar et al. (29) studied sound wave propagation using LBM, achieving acceptable results. Crouse et al. (92) investigated the propagation of standing acoustic waves and showed that the LBM can yield relatively good results on fundamental acoustic phenomena. Mari et al. (93) and Bres et al. (30) presented the dissipation and dispersion of acoustic waves using the BGK-LBM. Viggen (94)

proposed the sound propagation properties of the lattice Boltzmann equation for both free and forced waves. In addition, he proposed an extended model containing a bulk viscosity correction term with the idea that all equilibrium distributions must be identical for the one-dimensional D1Q3 velocity set. Dhuri et al. (95) investigated linear acoustic wave propagation in heterogeneous media with the BGK approximation and the multi-relaxation-time collision operators for the D2Q5 model. It should be noticed that many different schemes have been used because of numerical instabilities appearing when dealing with high Reynolds numbers (96–98) or specific characteristics of the fluid: the Taylor expansion method (99), the dual entropy approach (100), the local/global lower bound on the relaxation time (101), selective viscosity filtering (102), dissipation/dispersion optimized multiple relaxation times (103–105), augmenting hyper-viscosities in non-uniform grids (106–108), the entropy H-theorem (109–112), a regularized method for the BGK-LBM (31), the recursive and regularized LBM (LBM-rrBGK) (32, 33), and the cumulant LBM (5, 6, 43, 75). The recursively regularized LBM has been recently expanded and used for isothermal and weakly compressible flows at high Reynolds numbers, and fully compressible flows (113–115). Among these schemes, all of them having advantages and disadvantages, here the cumulant LBM is chosen due to the number of existing studies in the field of acoustics. Therefore, the aim of this work is to study the capability of the cumulant LBM to simulate sound wave propagation by calculating the deviation from analytical results, notably the dissipation and dispersion errors. Moreover, it tries to assess the effects of SPCH at high velocities on the noise beyond the cylinders, particularly, the acoustic damping effect of such flaps on sound propagation through interactions among acoustic waves, solid walls and shear layers.

## 2.2 Methodology

To study the effects of SPCH on the fluid domain and sound wave propagation, this section presents an explanation of the mathematics behind this complex phenomenon. First, the general description of the cumulant lattice Boltzmann method as a flow field solver is provided. Second, the finite element system of equations

derived for the structural solver and the Newmark Method is explained. Then, details on the fluid structure coupling are considered. Finally, to analyze the results of the cumulant LBM for the wave propagation, the general form of the lossy wave equation is obtained.

### 2.2.1 Cumulant lattice Boltzmann

The lattice Boltzmann method (LBM), a suitable substitute for Navier-Stokes solvers, can simulate complex fluid flows. This mesoscopic method is obtained from Ludwig Boltzmann's kinetic theory of gases. Although the LBM is regarded as a finite difference method for solving the Boltzmann transport equation, it leads to the Navier-Stokes equations by using the Chapman-Enskog expansion. The basic idea is that gas or fluid motion is modeled by a discrete momentum distribution function, to transfer momentum and energy through particle streaming and billiard-like particle collision on a Cartesian grid, at each time step (1). In general, the lattice is denoted by DdQq where d and q are the number of dimension and the number of the discrete speeds, respectively. The lattice Boltzmann equation without an external force is

$$f_i(x + e_{xi}c\Delta t, y + e_{yi}c\Delta t, t + \Delta t) - f_i(x, y, t) = \Omega_i \quad (2.1)$$

where  $f_i$ ,  $\Omega_i$  and  $c = \Delta x / \Delta t$  are, respectively the particle distribution function, the collision operator and the lattice speed, respectively.

In general, the LBM contains two key steps: collision and streaming. For the collision term, different choices give rise to methods like BGK, MRT, cascade, cumulant, and so on. This work considers the cumulant method as one of the newest and most robust LB methods.

The probability density function (PDF) is (8)

$$f(\xi, \eta) = \sum_{ij} f(\xi_i, \eta_j) \delta(\xi - \xi_i) \delta(\eta - \eta_j), \quad (2.2)$$

where  $f$  is the probability mass function (PMF) and  $\xi, \eta$  are discrete random variables with ranges  $R_\xi = \{\xi_1, \xi_2, \dots\}$ ,  $R_\eta = \{\eta_1, \eta_2, \dots\}$  corresponding to the microscopic velocities in x, y directions.



The moments of such PDF, without any discontinuity problems can be calculated as

$$\mu'_{\xi^m \eta^n} = \frac{\partial^m \partial^n}{\partial \Xi^m \partial H^n} M(\Xi, H) \Big|_{\Xi=H=0}, \quad (2.3)$$

where  $M(\Xi, H) = \sum_{ij} f(\xi_i, \eta_j) e^{\Xi \xi_i} e^{H \eta_j}$  is the moment generating function and  $H, \Xi$  are the normalized wave numbers.

To reduce the Galilean invariant problems of the collision step, the moment generating function is shifted into the moving frame of reference of the fluid. Then, the central moments can be calculated as

$$\mu_{\xi^m \eta^n} = \frac{\partial^m \partial^n}{\partial \Xi^m \partial H^n} \widehat{M}(\Xi, H) \Big|_{\Xi=H=0} \quad (2.4)$$

where  $\widehat{M}(\Xi, H) = e^{-\Xi u/c - H v/c} M(\Xi, H)$  is the central moment generating function.

To use the advantage of the logarithmic form of the moment generating function, the cumulant generating function is defined as (41)

$$c_{\xi^m \eta^n} = \frac{\partial^m \partial^n}{\partial \Xi^m \partial H^n} \ln(M(\Xi, H)) \Big|_{\Xi=H=0}. \quad (2.5)$$

Each cumulant relaxes with an individual relaxation rate

$$c_{\xi^m \eta^n}^* = c_{\xi^m \eta^n} + \omega_{\xi^m \eta^n} (c_{\xi^m \eta^n}^{eq} - c_{\xi^m \eta^n}) \quad (2.6)$$

where  $c_{\xi^m \eta^n}^{eq}$  are the cumulants of the equilibrium state. The equilibrium state for the cumulant generating function is  $CGF^{eq} = \Xi u/c + H v/c + \frac{\xi^2(\Xi^2 + H^2)}{2c^2}$  (14). The sound speed and the kinematic viscosity are calculated respectively, (116)

$$\xi_s = \frac{\Delta x}{\sqrt{3\Delta t}}, \quad (2.7)$$

$$\nu = \Delta t \xi_s^2 \left( \frac{1}{\omega} - \frac{1}{2} \right). \quad (2.8)$$

To itemize the algorithm: First the central moments of the distribution function are calculated using equation (2.4). Second, the cumulants are obtained from the central moments. Third, the post-collision cumulants from the collision operator are

quantified based on equation (2.6). Fourth, post-collision central moments from the post-collision cumulants are extracted. Fifth, the post-collision central moments are transferred back to the distribution functions (1).

### 2.2.2 Structural analysis

One of the numerical methods to simulate structural phenomena, is the finite element method (FEM). The FEM, generally, describes a set of algebraic equations for a domain subdivided into small-interconnected parts called finite elements. The elements are linked together by common boundaries, containing nodes, boundary lines, and surfaces. In this study the Euler-Bernoulli beam is used as structure. The transverse deflection  $w$  of the beam is governed by

$$\frac{d^2}{dx^2} \left( b \frac{d^2 w}{dx^2} \right) = f(x), \quad 0 < x < L \quad (2.9)$$

where  $b = b(x)$ ,  $f = f(x)$ , and  $f$  is the transversely distributed load. The function  $b = EI$  where  $E$  is the elasticity modulus and  $I$  is the moment of inertia. Equation (2.9) needs four boundary conditions. The structural domain is divided into a set of  $N$  line elements. To derive the element equations (117), a typical element  $\Omega^e = (x_e, x_{e+1})$  is isolated and the weak form of equation (2.9) over this element is constructed as

$$\begin{aligned} 0 &= \int_{x_e}^{x_{e+1}} v \left[ \frac{d^2}{dx^2} \left( b \frac{d^2 w}{dx^2} \right) - f \right] dx \\ &= \int_{x_e}^{x_{e+1}} \left[ -\frac{dv}{dx} \frac{d}{dx} \left( b \frac{d^2 w}{dx^2} \right) - vf \right] dx + \left[ v \frac{d}{dx} \left( b \frac{d^2 w}{dx^2} \right) \right]_{x_e}^{x_{e+1}} \\ &= \int_{x_e}^{x_{e+1}} \left( b \frac{d^2 v}{dx^2} \frac{d^2 w}{dx^2} - vf \right) dx + \left[ v \frac{d}{dx} \left( b \frac{d^2 w}{dx^2} \right) - \frac{dv}{dx} b \frac{d^2 w}{dx^2} \right]_{x_e}^{x_{e+1}} \end{aligned} \quad (2.10)$$

where  $v(x)$  is a weight function. Due to the two integrations by parts, an examination of the boundary terms makes it clear that the essential boundary conditions involve the deflection  $w$  and its derivative  $dw/dx$ , whereas the natural boundary conditions involve the bending moment  $bd^2w/dx^2$  and the shear force  $(d/dx)(bd^2w/dx^2)$

at the endpoint of the element. Using the following notation,

$$\begin{aligned}\theta &= -\frac{dw}{dx}, \\ \Phi_1^e &\equiv \left[ \frac{d}{dx} \left( b \frac{d^2w}{dx^2} \right) \right]_{x_e}, \quad \Phi_2^e \equiv \left( b \frac{d^2w}{dx^2} \right) \Big|_{x_e}, \\ \Phi_3^e &\equiv - \left[ \frac{d}{dx} \left( b \frac{d^2w}{dx^2} \right) \right]_{x_{e+1}}, \quad \Phi_4^e \equiv - \left( b \frac{d^2w}{dx^2} \right) \Big|_{x_{e+1}},\end{aligned}\quad (2.11)$$

equation (2.10) results in

$$\begin{aligned}0 &\equiv B(v, w) - L(v) \quad (2.12) \\ B(v, w) &= \int_{x_e}^{x_{e+1}} b \frac{d^2v}{dx^2} \frac{d^2w}{dx^2} dx, \\ L(v) &= \int_{x_e}^{x_{e+1}} v f dx + v(x_e) \Phi_1^e + \left( -\frac{dv}{dx} \right) \Big|_{x_e} + \Phi_2^e + v(x_{e+1}) \Phi_3^e + \left( -\frac{dv}{dx} \right) \Big|_{x_{e+1}} \Phi_4^e,\end{aligned}$$

which is a statement of the principle of virtual displacements, known as total potential energy of the beam element. Equation (2.12) requires interpolation functions ( $\phi$ ) for the element, which are continuous with nonzero derivatives up to order two. By satisfying the interpolation properties the functions are calculated as

$$\begin{aligned}w^e(x) &= u_1^e \phi_1^e + u_2^e \phi_2^e + u_3^e \phi_3^e + u_4^e \phi_4^e = \sum_{j=1}^4 u_j^e \phi_j^e, \quad (2.13) \\ u_1^e &= w(x_e), \quad u_2^e = \theta|_{x_e}, \quad u_3^e = w(x_{e+1}), \quad u_4^e = \theta|_{x_{e+1}}, \\ \phi_1^e &= 1 - 3 \left( \frac{x - x_e}{h_e} \right)^2 + 2 \left( \frac{x - x_e}{h_e} \right)^3, \quad \phi_2^e = - (x - x_e) \left( 1 - \frac{x - x_e}{h_e} \right)^2, \\ \phi_3^e &= 3 \left( \frac{x - x_e}{h_e} \right)^2 - 2 \left( \frac{x - x_e}{h_e} \right)^3, \quad \phi_4^e = - (x - x_e) \left[ \left( \frac{x - x_e}{h_e} \right)^2 - \frac{x - x_e}{h_e} \right].\end{aligned}$$

The finite element model is calculated by substituting  $w$  from (2.13) and  $v = \phi_i$  into equation (2.12),

$$K_{ij}^{x_{e+1}} = \int_{x_e}^{x_{e+1}} b \frac{d^2 \phi_i^e}{dx^2} \frac{d^2 \phi_j^e}{dx^2} dx, \quad (2.14)$$

$$F_i^{x_{e+1}} = \int_{x_e}^{x_{e+1}} \phi_i^e f dx + \Phi_i^e, \quad (2.15)$$

$$\sum_{j=1}^4 K_{ij}^e u_j^e - F_i^e = 0. \quad (2.16)$$

To obtain the time-dependent form of the equation of motion, the mass matrix is calculated as (118)

$$M_{ij}^e = \int_{x_e}^{x_{e+1}} m \phi_i^e \phi_j^e dx. \quad (2.17)$$

And with the same  $b = EI$ , the matrix elements of  $M$ ,  $K$ , and  $F$  are

$$K^e = \frac{EI}{h} \begin{bmatrix} \frac{12}{h^2} & \frac{-6}{h} & \frac{-12}{h^2} & \frac{-6}{h} \\ \frac{-6}{h} & 4 & \frac{6}{h} & 2 \\ \frac{-12}{h^2} & \frac{6}{h} & \frac{12}{h^2} & \frac{6}{h} \\ \frac{-6}{h} & 2 & \frac{6}{h} & 4 \end{bmatrix}, \quad (2.18)$$

$$F^e = -\frac{fh}{12} \begin{bmatrix} 6 \\ -h \\ 6 \\ h \end{bmatrix} + \begin{bmatrix} \Phi_1 \\ \Phi_2 \\ \Phi_3 \\ \Phi_4 \end{bmatrix}, \quad (2.19)$$

$$M^e = mh \begin{bmatrix} \frac{13}{35} & h \frac{11}{210} & \frac{9}{70} & -h \frac{13}{420} \\ h \frac{11}{210} & h \frac{1}{105} & h \frac{13}{420} & -h \frac{1}{140} \\ \frac{9}{70} & h \frac{13}{420} & \frac{13}{35} & -h \frac{11}{210} \\ -h \frac{13}{420} & -h \frac{1}{140} & -h \frac{11}{210} & h \frac{1}{105} \end{bmatrix}. \quad (2.20)$$

The governing equation for the linear dynamic response of the finite element system is

$$M\ddot{x} + C\dot{x} + Kx = F, \quad (2.21)$$

where  $M$ ,  $C$ ,  $K$  are the mass, damping, and stiffness matrices.  $F$  is the external force vector and  $x$  is the displacement vector (119).

The discrete equation system (2.21) is solved using the Newmark method, which is a direct integration method (119). In this work, the standard Newmark method is used as follows. It is first assumed that

$$x_{t+\Delta t} = x_t + (\Delta t)\dot{x}_t + (\Delta t)^2 [(0.5 - \beta)\ddot{x}_t + \beta\ddot{x}_{t+\Delta t}], \quad (2.22a)$$

$$\dot{x}_{t+\Delta t} = \dot{x}_t + (\Delta t) [(1 - \gamma)\ddot{x}_t + \gamma\ddot{x}_{t+\Delta t}], \quad (2.22b)$$

where  $\beta$  and  $\gamma$  are constant. Substituting equations (2.22a) and (2.22b) into the system equation (2.21) and solving for  $\ddot{x}$  results in

$$K_l \ddot{x}_{t+\Delta t} = F_{t+\Delta t}^r, \quad (2.23a)$$

$$K_l = [K\beta(\Delta t)^2 + C\gamma\Delta t + M], \quad (2.23b)$$

$$F_{t+\Delta t}^r = F_{t+\Delta t} - K \left\{ x_t + (\Delta t)\dot{x}_t + (\Delta t)^2(0.5 - \beta)\ddot{x}_t \right\} - C \left\{ \dot{x}_t + (\Delta t)(1 - \gamma)\ddot{x}_t \right\}. \quad (2.23c)$$

Thus, the accelerations  $\ddot{x}_{t+\Delta t}$  can be calculated by solving the matrix equation system (2.23a). The velocities and displacements can be obtained by means of equations (2.22a) and (2.22b). The Newmark method is unconditionally stable provided that  $\gamma = 0.5$  and  $\beta \geq (2\gamma + 1)^2/16$ .

### 2.2.3 Coupling scheme

Fluid-structure interaction (FSI) is the coupling between the laws of fluid dynamics and those of structural mechanics. Forces exerted on the object lead to deformations depending on the pressure and velocity of the flow and the material properties of the structure. Therefore, the velocity and pressure fields have effects on the structural deformations, and vice versa.

In general, partitioned and monolithic solution procedures have been developed for the numerical simulation of FSI problems (120). In this work, as in reference (120)

the partitioned method is used which means that separate solvers are chosen: The cumulant LBM for the fluid solver and the finite element method for the structural solver.

There are two possibilities to obtain forces on boundaries in LBM calculations: Momentum exchange and Stress integration (121). Even though the Momentum exchange scheme predicts well integral forces on large structural elements, when it comes to consider the resolution order of the fluid mesh this scheme is not reliable due to the considerable reduction of matching links. Therefore, to evaluate the forces on boundaries with the LBM, here the Pressure/stress integration scheme is chosen. Such scheme benefits from the locally available stress tensor in LBM calculated as

$$S_{IJ} = -c_s^2 \rho \delta_{IJ} + \sigma_{IJ} \quad (2.24)$$

where  $\delta$  is the Kronecker-Delta. The stresses on the boundary node can be extrapolated from neighboring cells through the matching squares algorithm (122) by generating isolines on fixed Cartesian grids. In general, there are 16 possibilities of intersection of a structure boundary node and a fluid cell, as discussed in reference (120). Figure 2.1 shows two possibilities for the position of the structure inside the fluid domain and the extrapolation of the stresses on the boundary node from neighboring cells. The extrapolation of the stresses for Structure 1 reads

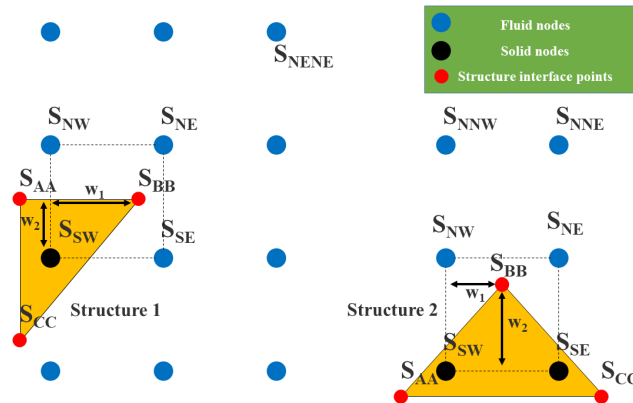


FIGURE 2.1: Two possibilities for the position of the structure inside the fluid domain.

$$S_{SW} = 2S_{NE} - S_{NENE}, \quad (2.25)$$

and the extrapolation for Structure 2,

$$\begin{aligned} S_{SW} &= 2S_{NW} - S_{NMW}, \\ S_E &= 2S_{NE} - S_{NNE}. \end{aligned} \quad (2.26)$$

The next step after extrapolation is a bilinear interpolation for the stresses

$$S = (1 - w_1)(1 - w_2) S_{SW} + w_1(1 - w_2) S_{SE} + w_1w_2S_{NE} + (1 - w_1)w_2S_{NW} \quad (2.27)$$

where  $w_1$  and  $w_2$  are normalized weight factors.

By integrating along the boundary  $\Gamma$  the scalar product of the stress tensor times the unit normal vector, the load vector is calculated,

$$F = \int_{\Gamma} S \cdot n \, d\Gamma. \quad (2.28)$$

Considering the fact that the stress components are linear (figure 2.2), the load vector at point BB using equation 2.28 equals to

$$F_{BB} = (0.25S_{AA} + 0.75S_{BB}) n_{AABB} + (0.75S_{BB} + 0.5S_{CC}) n_{BBCC}. \quad (2.29)$$

Owing to the two different grids for structure and fluid, an interface mesh is used to couple both meshes. This mesh is made of a polyline at which physical quantities are required to be stored. The interface mesh can be adapted by the FEM and LBM solvers. Due to the effect of the fluid and the structure on each other there is the possibility that after some structure movement a node in the fluid domain relocates to the solid domain and vice versa. Therefore, the algorithm must activate and deactivate the nodes inside the domains (Fig 2.3). In addition, the local velocity at the

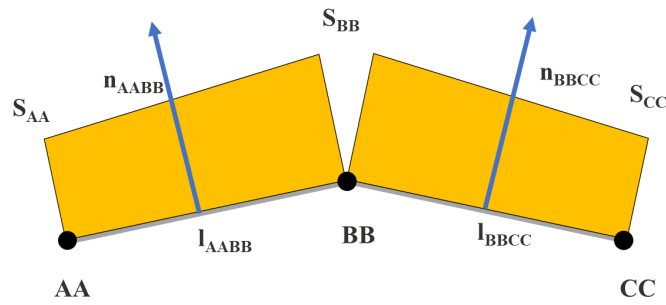


FIGURE 2.2: Force calculation from stress.

new fluid node is obtained from linear interior extrapolation. The pressure and the higher order moments are calculated based on a local Poisson type of iteration (123). The distribution functions of the new active node (fluid) are constructed or initialized as the summation of the equilibrium functions, calculated by extrapolating the velocity and the density, plus the non-equilibrium parts, obtained by the previously determined pressure and higher order moments (120, 121, 123).

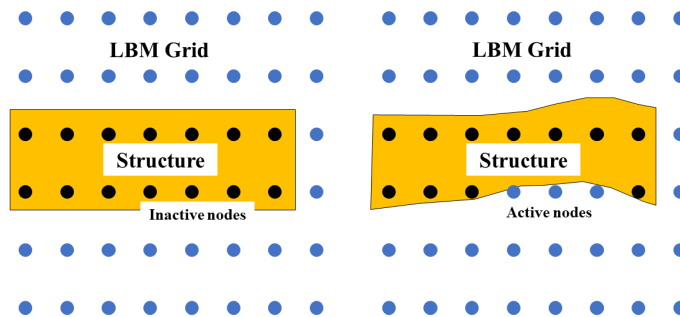


FIGURE 2.3: Active (fluid) and inactive (structural) nodes in the LBM grid.

The FSI algorithm is depicted in Fig 2.4: First the fluid solver calculates the load vector on the interface mesh points. Second, the loads are transferred through the interface mesh. Third, the structural solver calculates the new displacements. Fourth, the new displacements are transferred through the interface mesh. Fifth, the position of the interface surface geometry is calculated by the fluid solver. Sixth, the previous steps are repeated in a sequence.



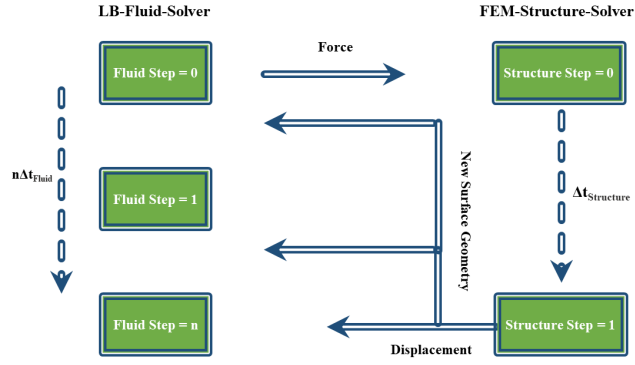


FIGURE 2.4: Coupling algorithm.

### 2.2.4 The wave equation

Acoustic waves constitute one kind of pressure fluctuations that cause the propagation of energy through a medium: gas, liquid, and solid. Even though there are different ways to obtain the lossy wave equation (124), here it is derived based on references (125, 126).

The general form of the nonlinear Navier-Stokes equation, without external body forces, is

$$\rho \left( \frac{\partial \mathbf{u}}{\partial t} + (\mathbf{u} \cdot \nabla) \mathbf{u} \right) = -\nabla p + \left( \frac{4}{3} \eta + \eta_B \right) \nabla (\nabla \cdot \mathbf{u}) - \eta \nabla \times \nabla \times \mathbf{u}, \quad (2.30)$$

where  $\eta$  is the coefficient of shear viscosity,  $\eta_B$  is the coefficient of bulk viscosity, and  $\eta \nabla \times \nabla \times \mathbf{u}$  is the dissipation of acoustic energy, which has few effects on linear acoustics.

In general, a quantity called condensation is defined in linear acoustics,  $s = (\rho - \rho_0) / \rho_0$  which is the ratio between the deviation from the equilibrium density and the equilibrium density itself, and must be small. In addition, the total pressure equation is written as  $p = p_0 + p'$  where  $p_0$  is the atmospheric pressure and  $p'$  is the acoustic pressure.

Using the linearized form of equation (2.30) and the linearized continuity equation  $\nabla \cdot \mathbf{u} = -\partial s / \partial t$ , plus the equation of state  $p' = \rho_0 c_s^2 s$ , leads to a lossy wave equation,

$$\left(1 + \tau_s \frac{\partial}{\partial t}\right) \nabla^2 p' = \frac{1}{c_s^2} \frac{\partial^2 p'}{\partial t^2} \quad (2.31)$$

where

$$\tau_s = \frac{1}{\rho_0 c_s^2} \left( \frac{4}{3} \eta + \eta_B \right).$$

## 2.3 Results and Discussion

In this section, the cumulant LBM is used first to calculate the acoustic dissipation and dispersion for benchmark cases, and the results are compared with theoretical values. Second, spherical wave propagation at a very low viscosity is studied by means of different LB methods and the results are compared with the theoretical solution. Finally, the cumulant LBM is coupled with a finite element method to study the effect on the flow and sound propagation around one single and two twin cylinders due to SPCH at high Re numbers, as a real engineering FSI case of study.

### 2.3.1 Acoustic properties of the cumulant lattice Boltzmann method

The LBM has been used to model the aerodynamic and hydrodynamic characteristics of different phenomena, moreover, it has the capability to directly obtain the acoustic field without additional computational cost. In this section, the aim is to study the accuracy of the cumulant LBM in predicting acoustic properties for benchmark cases before extending it to fluid-structure interaction applications in the following sections. Initially, the dispersion and dissipation relations of the propagation of a plane wave are presented based on the temporal and spatial analyses from equation (2.31) as in Bres et al.'s work (30). Then, the propagation of a standing plane wave and a planar acoustic pulse of Gaussian shape is implemented using the cumulant LBM. Numerical errors, finally, for the dissipation and dispersion parameters are computed for these cases.

#### Planar standing wave

A standing plane acoustic wave is considered for a temporal analysis as a first configuration. The calculated dissipation and dispersion relations based on the temporal

analysis of equation (2.31) (30) lead to

$$c_T = \zeta_s \sqrt{1 - \left(\frac{k\nu}{\zeta_s}\right)^2}, \quad (2.32a)$$

$$\alpha_T = k^2\nu, \quad (2.32b)$$

where  $k$  is the wave-number. The assumptions for this set-up are listed in table 2.1. For a linear acoustic problem, the perturbation amplitude  $p'$  is chosen small compared to the average pressure  $p_0$ . Periodic boundary conditions are applied in both directions. The time step is chosen so that we have dispersion and dissipation effects, but not boundary side effects.

TABLE 2.1: Parameters for the planar standing wave

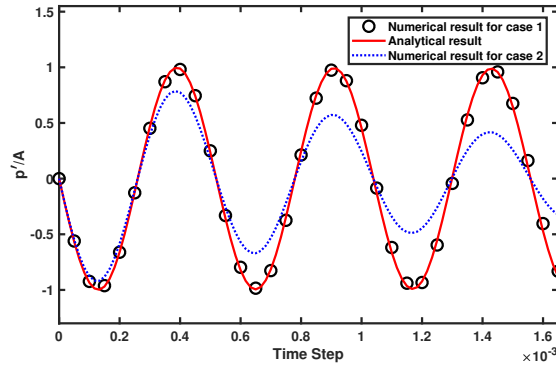
Variables	$p'(x, y, 0)$	$\rho'$	$u'$	$v'$	A
Description	$A \sin\left(\frac{2\pi x}{\lambda}\right)$	$\frac{p'}{\zeta_s^2}$	$\frac{p'}{\rho_0 \zeta_s}$	0	$10^{-3} p_0$

The acoustic pressure at time  $t$  is (30)

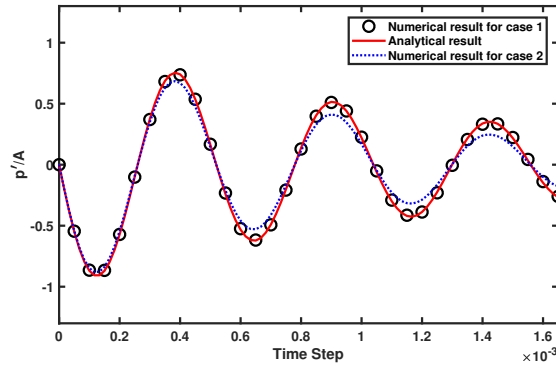
$$p'(x, y, t) = A \exp[-(\alpha_T + \alpha_T^{num}) t] \sin[k(x - (c_T + c_T^{num}) t)], \quad (2.33)$$

where the superscript "num" denotes the deviation between the numerical and theoretical values. Therefore,  $c_T^{num}$  and  $\alpha_T^{num}$  are the deviation phase speed and temporal dissipation rate, respectively. These coefficients can be derived, for any location, from the plot of the perturbation versus time using nonlinear least-squares fitting and equations (2.32a) and (2.32b). In addition, the results can be presented either as a function of the number of the points per wavelength  $N_{ppw} = \lambda/\Delta x$  or the non dimensional wave-number  $k\Delta x = 2\pi/N_{ppw}$ .

To study the accuracy of the propagation of waves using the cumulant LBM, various viscosities and different resolutions (i.e. number of points per wavelength) are considered. One of the most important properties for characterizing fluid flow which has a vital effect on the accuracy of acoustics simulations is the bulk viscosity (1, 6, 14). Figure 2.5 shows the comparison between numerical results for two different choices of the bulk viscosity against the analytical solution. The subfigures show



(A)  $\nu = 1.5 \times 10^{-3} \text{m}^2/\text{s}$ .



(B)  $\nu = 1.5 \times 10^{-1} \text{m}^2/\text{s}$ .

FIGURE 2.5: Non-dimensional acoustic pressure  $p'/A$  vs. time history [s] at (0,0) for the planar standing wave considering two different choices for the bulk viscosity: Case 1 where the relaxation time for the bulk viscosity is chosen based on equation (2.8)) and Case 2 where the value of the relaxation time for the bulk viscosity is chosen as 1.

the results for values  $\nu = 1.5 \times 10^{-3} \text{m}^2/\text{s}$  and  $\nu = 1.5 \times 10^{-1} \text{m}^2/\text{s}$  of the kinematic viscosity and  $N_{ppw} = 18$  point per wavelength. Case 1: the relaxation time for the bulk viscosity is chosen based on equation (2.8). Case 2: the value of the relaxation time for the bulk viscosity is chosen as 1. Therefore, a wrong selection of the bulk viscosity leads to inaccurate results.

Figure 2.6 presents the acoustic pressure time-history for  $\nu = 1.5 \times 10^{-2} \text{m}^2/\text{s}$  with  $N_{ppw} = 12$  points per wavelength. The relative numerical error of the phase speed and temporal dissipation rate are presented as functions of the non dimensional wave-number in table 2.2. The table shows that the deviations from the theoretical values are small, even for a relatively low resolution with 12 points per wavelength: about 0.77 percent in the phase speed and 0.018 percent in the dissipation

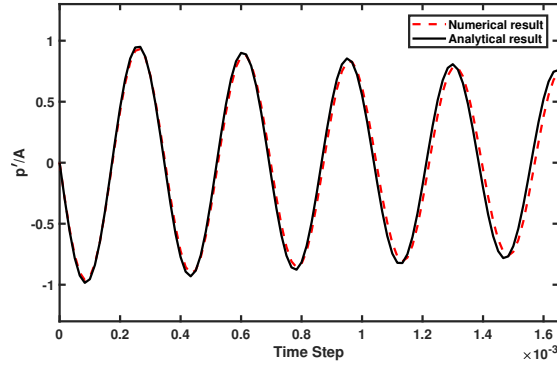


FIGURE 2.6: Non-dimensional acoustic pressure  $p'/A$  vs. time history [s] at (0,0) for the planar standing wave.

rate. It should be noted that by reducing the viscosity, the phase speed and dissipation errors are almost constant. Thus the results are only a function of  $N_{ppw}$  and are independent of viscosity in the range of interest. It can be concluded that the results of the cumulant LBM show a good agreement with the theoretical values and behave similarly to the numerical values of reference (30).

TABLE 2.2: Relative numerical error of the specified acoustic properties as a function of the non-dimensional wave-number ( $k\Delta x$ ) for the planar standing wave.

$k\Delta x$	$\pi/12$	$\pi/6$	$\pi/4$	$\pi/3$	$\pi/2$
$c_T^{num}/c_T$	$-1.8 \times 10^{-3}$	$-7.7 \times 10^{-3}$	$-1.7 \times 10^{-2}$	$-3.1 \times 10^{-2}$	$-7.2 \times 10^{-2}$
$\alpha_T^{num}/\alpha_T$	$-7.5 \times 10^{-4}$	$-1.8 \times 10^{-4}$	$-1.2 \times 10^{-3}$	$-4.3 \times 10^{-3}$	$-2.5 \times 10^{-2}$

### Planar pulse wave

A planar pulse wave is studied for a spatial analysis where acoustic waves of fixed frequencies propagate through the domain. The dissipation and dispersion relations derived, based on the spatial analysis from equation (2.31) (30) are

$$c_S = \sqrt{2}\zeta_s \sqrt{\frac{1 + (\omega\tau_s)^2}{\sqrt{1 + (\omega\tau_s)^2} + 1}}, \quad (2.34a)$$

$$\alpha_S = \frac{\omega}{\sqrt{2}\zeta_s} \sqrt{\frac{\sqrt{1 + (\omega\tau_s)^2} - 1}{1 + (\omega\tau_s)^2}}. \quad (2.34b)$$

With the assumptions presented in table 2.3, a planar pulse of Gaussian shape initially propagates from the origin through the domain where periodic boundary conditions are imposed. The time step is chosen in a way that the pulse passes without interfering with the boundaries.

TABLE 2.3: Parameters for the planar pulse wave

Variables	$p'(x, y, 0)$	$\rho'$	$u'$	$v'$	A	$\sigma$
Description	$A \exp\left(-\ln(2) \frac{x^2}{\sigma^2}\right)$	$\frac{\rho'}{c_s^2}$	$\frac{p'}{\rho_0 c_s}$	0	$10^{-3} p_0$	0.03

The Fourier transform of the pressure time history of the passing wave gives the Fourier coefficient of pressure  $\hat{p}'(x, \omega)$

$$\hat{p}'(x, \omega) = \hat{p}'(x, 0) \exp[-(\alpha_s + \alpha_s^{num})x] \exp\left[i\omega \frac{x}{c_s + c_s^{num}}\right] \quad (2.35)$$

which is similar to the solution of equation (2.31) (30), where  $c_s^{num}$  and  $\alpha_s^{num}$  are the deviation phase speed and spatial dissipation rate, respectively. The coefficients are calculated as a function of the frequency using the phase and amplitude of the ratio  $\hat{p}'(x, \omega) / \hat{p}'(x, 0)$  and the dissipation and dispersion relations given in equations (2.34a) and (2.34b).

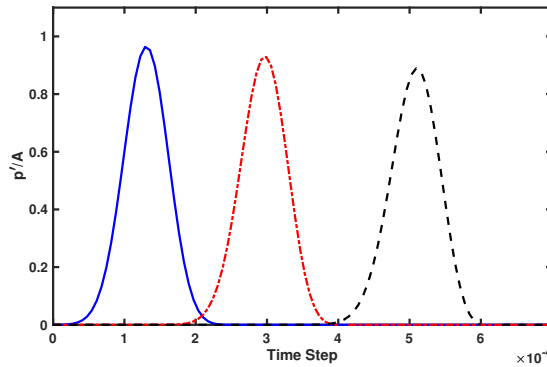
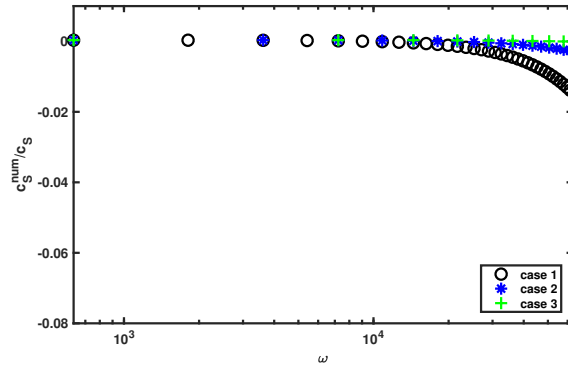
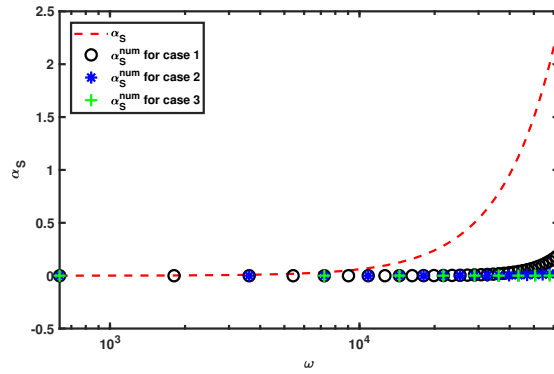


FIGURE 2.7: Non-dimensional acoustic pressure  $p'/A$  vs. time history [s] at origin (—), 0.056m (---) and 0.128m (---) from the reference position, for the planar pulse wave.

Figure 2.7 presents the acoustic pressure time-history of the propagation of the planar Gaussian pulse for  $\nu = 2.36 \times 10^{-2} \text{m}^2/\text{s}$  with a resolution  $\Delta x = 0.004\text{m}$ . It shows the planar wave as it moves toward the positions 0.056m and 0.128m from the reference position. In addition, the amplitude of the wave changes with the



(A) Phase speed.



(B) Dissipation rate [Np/m].

FIGURE 2.8: Numerical error of the specified acoustic properties for the planar pulse wave as functions of the angular frequency [Hz] ( $\nu = 2.36 \times 10^{-2} \text{m}^2/\text{s}$  and different resolution).

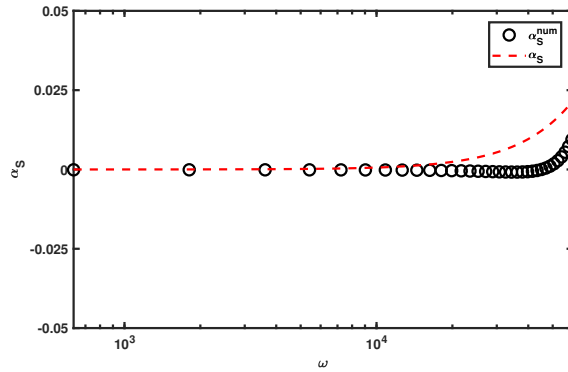


FIGURE 2.9: Numerical error of the dissipation rate [Np/m] for the planar pulse wave as a function of angular frequency [Hz] (for  $\nu = 2.35 \times 10^{-4} \text{m}^2/\text{s}$  and resolution  $\Delta x = 0.004\text{m}$ ).

propagation distance from the reference point. The relative numerical error of the phase speed  $c_s^{num}/c_s$  and the dissipation rate  $\alpha_s^{num}$  (in Np/m, where Np is a dimensionless unit called neper) are depicted in figures 2.8a and 2.8b as functions of the angular frequency, for resolutions  $\Delta x = 0.004\text{m}$  (Case 1),  $\Delta x = 0.002\text{m}$  (Case 2), and

$\Delta x = 0.001\text{m}$  (Case 3). Errors are small as in the planar standing wave example, even for the relatively low resolution  $\Delta x = 0.004\text{m}$ . Various viscosities, as in the first set-up, are used to study the predictive accuracy of the cumulant LBM in a traveling planar pulse. Figure 2.9 presents the relative numerical error of the dissipation rates for  $\nu = 2.35 \times 10^{-4}\text{m}^2/\text{s}$  and resolution  $\Delta x = 0.004\text{m}$ . It shows the same behavior as in the planar standing wave case regarding the reduction of viscosity. To conclude, the results of the cumulant LBM show a good agreement with the theoretical values for the dissipation rate.

### 2.3.2 Spherical wave

Unlike section 2.3.1 where the wave propagates in a straight line, in most real cases, sources generate a wave which expands in a set of spherical wave fronts. The analytic solution for an outgoing cylindrical wave obtained from equation (2.31) in cylindrical coordinates is

$$\rho'(x, y, t) = AH_0^{(2)}(kr) \exp(i\omega t), \quad (2.36)$$

where  $H_0^{(2)}$  is the zeroth-order Hankel function of the second kind (126). In the following section, spherical wave propagation is studied using the cumulant LBM for a low value of the viscosity  $\nu = 1.5 \times 10^{-5}\text{m}^2/\text{s}$ .

#### Acoustic pulse

A pseudo-2D acoustic pulse is investigated as a first configuration of spherical wave propagation, where the pulse assumes a Gaussian shape. This is the most standard aeroacoustic 2D benchmark case (127). Table 2.4 shows the assumptions of this setup. Periodic boundary conditions are chosen. However, the time step as well as the total simulation time are set to avoid any boundary effects.

For very low viscosities and small amplitudes of the acoustic perturbation, equation (2.36) results in the density fluctuation  $\rho'(x, y, t)$  (128):

$$\rho'(x, y, t) = \frac{A}{2\alpha} \int_0^\infty \exp\left(\frac{-s^2}{4\alpha}\right) \cos(\zeta_s t s) J_0(rs) s ds, \quad (2.37)$$



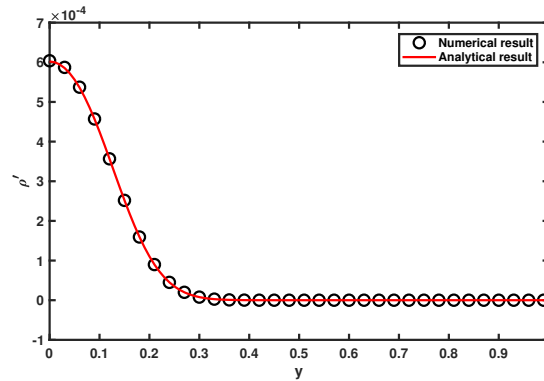
where  $J_0$  is the zeroth-order Bessel function of the first kind.

In this set-up, an acoustic pulse is generated by an initial Gaussian pressure distribution from the center of the computational domain, then the wave front of the pulse expands rapidly throughout the domain.

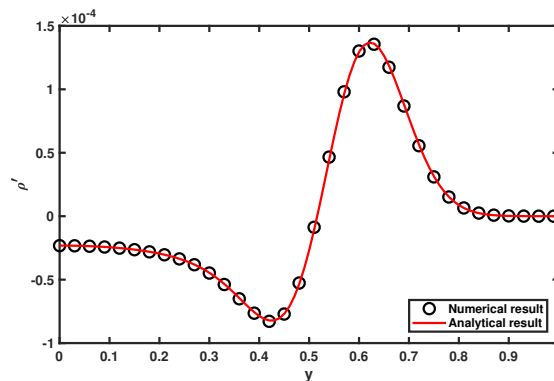
TABLE 2.4: Parameters for the pseudo-2D acoustic pulse

Variables	$\rho'$	$u'$	$v'$	$\epsilon$	$\alpha$	$b$	$r$
Description	$\epsilon \exp(-\alpha r^2)$	0	0	$10^{-3}$	$\frac{\ln(2)}{b^2}$	$10^{-1}$	$\sqrt{x^2 + y^2}$

Figure 2.10 draws a comparison between the numerical and analytical solutions for the density function of the acoustic pulse propagation. There is a good agreement between the cumulant LBM and the analytical solution at time steps 10 (figure 2.10a) and 100 (figure 2.10b). The results show that the cumulant LBM faithfully reproduces the spherical acoustic pulse wave at a very low viscosity.



(A) Time step=10.



(B) Time step=100.

FIGURE 2.10: The comparison of the analytical and numerical values of the perturbation  $\rho'$  [kg/m<sup>3</sup>].

### Acoustic point source

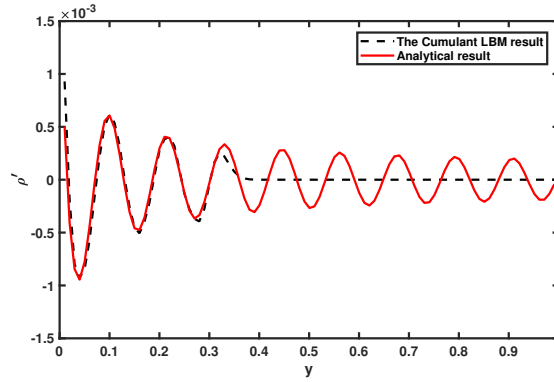
In the preceding section, finite acoustic waves propagate throughout the domain from an initial wave distribution. It is time to study infinite waves such as those produced by a point source which emits a sinusoidal signal. The assumptions for this set-up are presented in table 2.5.

TABLE 2.5: Parameters for the acoustic point source

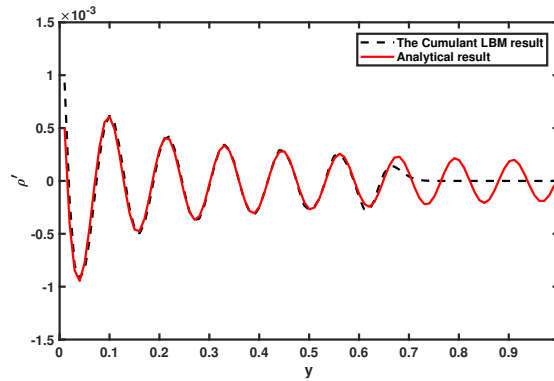
Variables	$\rho'$	$\omega$	$B$	$r$	$T$
Description	$B \sin(\omega t)$	$\frac{2\pi}{T}$	$10^{-2}$	$\sqrt{x^2 + y^2}$	20

To simulate this point source, a sinusoidal density function is fixed to the LBM lattice at the center of the domain as in references (129) and (126). Furthermore, the velocity can be chosen as a constant ( $u = 0$ ) or based on the particles streaming into the source node to guarantee conservation inside the domain. In addition, periodic boundary conditions are imposed.

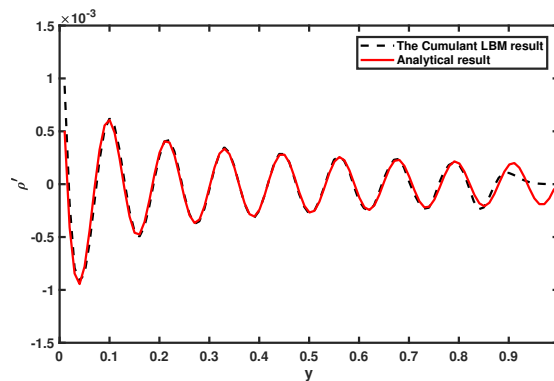
In order to make a meaningful assessment of the results of different LB methods regarding the stationary analytic solution for the point source cylindrical waves given by equation (2.36), we used the same method as Viggen (126) and Sagaut et al. (130). Figures 2.11 and 2.12 show the comparison between the numerical result and the stationary analytical solution for the propagation of the density function of the acoustic point source wave. The comparison shows a good match between the cumulant LBM result and the stationary analytical solution at time steps 60 (figure 2.11a), 120 (figure 2.11b), and 160 (figure 2.11c). It should be noted that the reason why the numerical density is 0 beyond a certain point is that the spherical waves spreading from the source have not yet reached those points at that time. The plots for different time steps show that the unsteady spherical waves follow the stationary analytical solution by overlapping it over time. In addition, as Viggen (126) and Sagaut et al. (130) have shown, the stationary analytical graph can give a mature and understandable prediction of the wave motion throughout the whole domain. On the contrary, the comparison does not draw a good match between the BGK LBM and the analytical solution at time steps 60 (figure 2.12a), 120 (figure 2.12b), and 160 (figure 2.12c). Even though, the numerical results follow the analytic solution, they



(A) Time step 60.



(B) Time step 120.



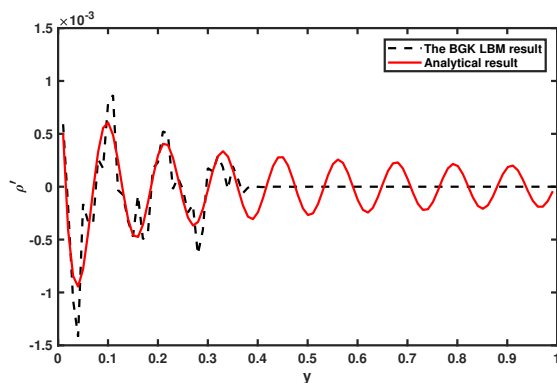
(C) Time step 160.

FIGURE 2.11: Comparison of the stationary analytical and numerical values of the perturbation  $\rho'$  [ $\text{kg}/\text{m}^3$ ] for the cumulant LBM.

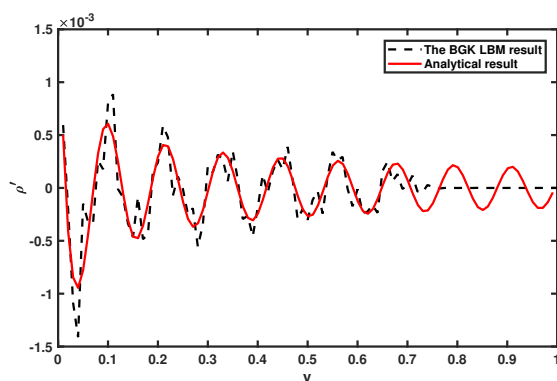
display noisy behavior, as the method is unstable at low viscosities. In a nutshell, the acoustic point source example can illustrate the power of the cumulant lattice Boltzmann method to naturally simulate acoustic behavior even at a very low viscosity.

### 2.3.3 Splitter plates attached to a cylinder looking like hair (SPCH)

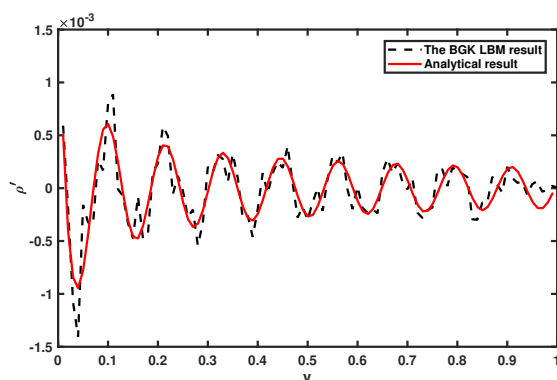
There is a growing need for the SPCH to control flow and Aeolian tones in many industries. Aeolian tones, i.e. sound generated by flow over objects, is relevant to



(A) Time step 60.



(B) Time step 120.



(C) Time step 160.

FIGURE 2.12: Comparison of the analytical and numerical values of the perturbation  $\rho'$  [ $\text{kg}/\text{m}^3$ ] for the BGK LBM.

airframes at high Reynolds numbers. To have a good assessment of such devices, the finite element method as a structural solver is coupled with the cumulant LBM as a fluid solver. Thus, this section will challenge the cumulant LBM in a real engineering FSI modeling problem, by focusing on the influence of the SPCH on the dynamics of a cylinder wake flow.

Six cases are examined in this section, presented in table 2.6 and figure 2.13.

These cases consist of a single cylinder and two twin cylinders aligned perpendicularly to the free stream and whose centers are 3 diameters apart. The origin of coordinates is the mid-point between the two cylinder centers. Case 1 and Case 4 should be considered as references for Cases 2 and 3, and Cases 5 and 6, respectively, when describing figures 2.14, 2.17, and 2.18. Table 2.7 shows the assumptions for the fluid and the domain in these setups. The Reynolds number is chosen based on the cylinder diameter and the free stream velocity. The fluid characteristics are set based on air. The flexible flaps are distributed homogeneously along the aft part of the segments facing the downstream direction at 60 degrees from the center. In addition, the Young modulus is  $12.525 \times 10^6 \text{kg/ms}^2$  and the structural density is  $\rho_{solid} = 1000 \text{kg/m}^3$ . The boundary conditions include velocity inlet ( $U_0$ ), non-reflecting (14) and pressure outlet boundary conditions, plus the bounce back scheme (120). It should be noted that we used the modified bounce back scheme developed in (131, 132) for the velocity, which is second order accurate for arbitrarily shaped boundaries.

TABLE 2.6: Cases studied for the SPCH (r is the radius of the cylinder)

Cases	Figures	Cylinders	Flaps	Length of flaps	Width of flaps	State of flaps
1	2.13a	1	0	$\times$	$\times$	$\times$
2	2.13c	1	3	$r$	0.001 m	Stationary
3	2.13e	1	2	$2r$	0.001 m	Moving
4	2.13b	2	0	$\times$	$\times$	$\times$
5	2.13d	2	3	$r$	0.001 m	Stationary
6	2.13f	2	2	$2r$	0.001 m	Moving

To validate the results, the cumulant LBM results for Cases 1 and 4 are compared with experimental and several previous numerical studies.

TABLE 2.7: Parameters for the SPCH study

Variables	$U_\infty$	$D$	fluid	Domain length	Domain width
Values	24.5 m/s & 73.5 m/s	0.00955 m	air	60 D	30 D

Table 2.8 presents the comparison between experimental (133, 134) and cumulant LBM results on the Strouhal number, a dimensionless number describing oscillating

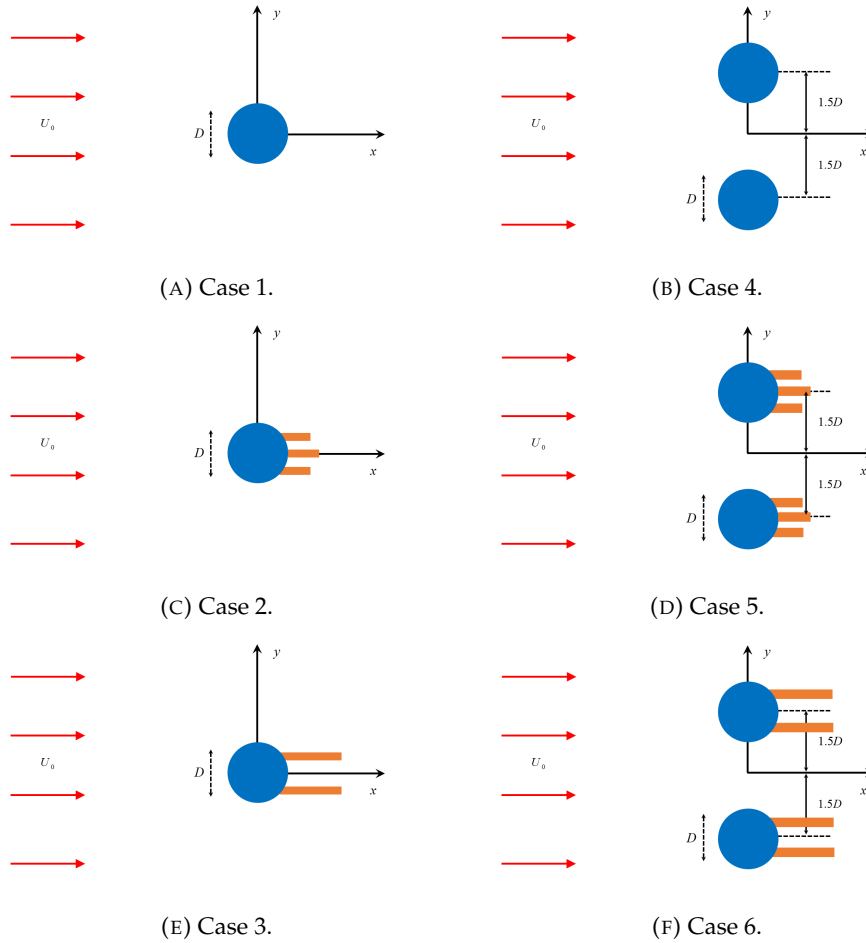


FIGURE 2.13: Computational domain of the cases studied for the SPCH problem.

flow mechanisms. It is defined as  $St = 2r/(U_\infty T) = (2rf)/U_\infty$ , where  $T$  and  $f$  are the period and the frequency of the vortex shedding, respectively. The results in table 2.8 are for Case 1 of figure 2.13 at  $Re = 1.58 \times 10^4$ . The results are presented for three grid resolutions. The Strouhal number for grid resolutions 2 and 3 shows less than 1 percent deviation from the reference data.

TABLE 2.8: The Strouhal number for Case 1

	St
Experimental result (133, 134)	0.201
Cumulant LBM result for grid resolution 1 (nodes=525056)	$0.185 \pm 0.001$
Cumulant LBM result for grid resolution 2 (nodes=1050112)	$0.203 \pm 0.005$
Cumulant LBM result for grid resolution 3 (nodes=2100225)	$0.202 \pm 0.011$

Table 2.9 shows a similar comparison for Case 4 and  $Re = 1.58 \times 10^4$ . It shows

that the results for grid resolutions 2 and 3 are between the results of Guenanff and Lockard (135). Therefore, to reduce the computational cost, the grid resolution 2 is used.

TABLE 2.9: The Strouhal number for Case 4

	St
Kia et al. (136)	0.205
Cheong et al. (137)	0.204
Guéanff et al (135)	0.212
Lockard (135)	0.222
Loh et al. (135)	0.239
<b>Cumulant LBM result for grid resolution 1 (nodes=525056)</b>	0.194 ± 0.001
<b>Cumulant LBM result for grid resolution 2 (nodes=1050112)</b>	0.218 ± 0.004
<b>Cumulant LBM result for grid resolution 3 (nodes=2100225)</b>	0.215 ± 0.009

The generation of vorticity past the cylinders under consideration can give a good estimation of the effects of SPCH. Figure 2.14 shows the spread of the vorticity in the wake past the cylinder for Cases 1-3 and  $Re = 4.7 \times 10^4$ . Figure 2.14a shows a wavy layer of discrete vorticity moving downstream in the wake of the cylinder for Case 1. Near the cylinder, the wave pattern is sharper than in farther downstream, due to momentum transport within the system caused by random and chaotic time-dependent motion occurring in the region. In addition, the figure shows that the spatial generation of vorticity is asymmetrical. The position of the vortices changes with time; in fact, vorticity oscillates and radiates sound waves into the flow. Figure 2.14b depicts the spread of vorticity created by three flaps which are not allowed to move. It shows that the use of a sparse set of such flaps can passively manipulate the vortex shedding generated in the wake of bluff bodies. The transverse distance of the vorticity from the center-line reduces. Figure 2.14c depicts the spread of the vorticity caused by two flaps with length  $L = 2r$  allowed to move. The mobility of flaps is one of the major elements having great effects on the vorticity. It is clear that the presence of flaps alters the phase within the vortex shedding cycle such that the transversal dislocation of the shed vorticity is reduced. Accordingly, the vorticity is not arranged in the same manner as in Case 1, instead it is shed in a row along the

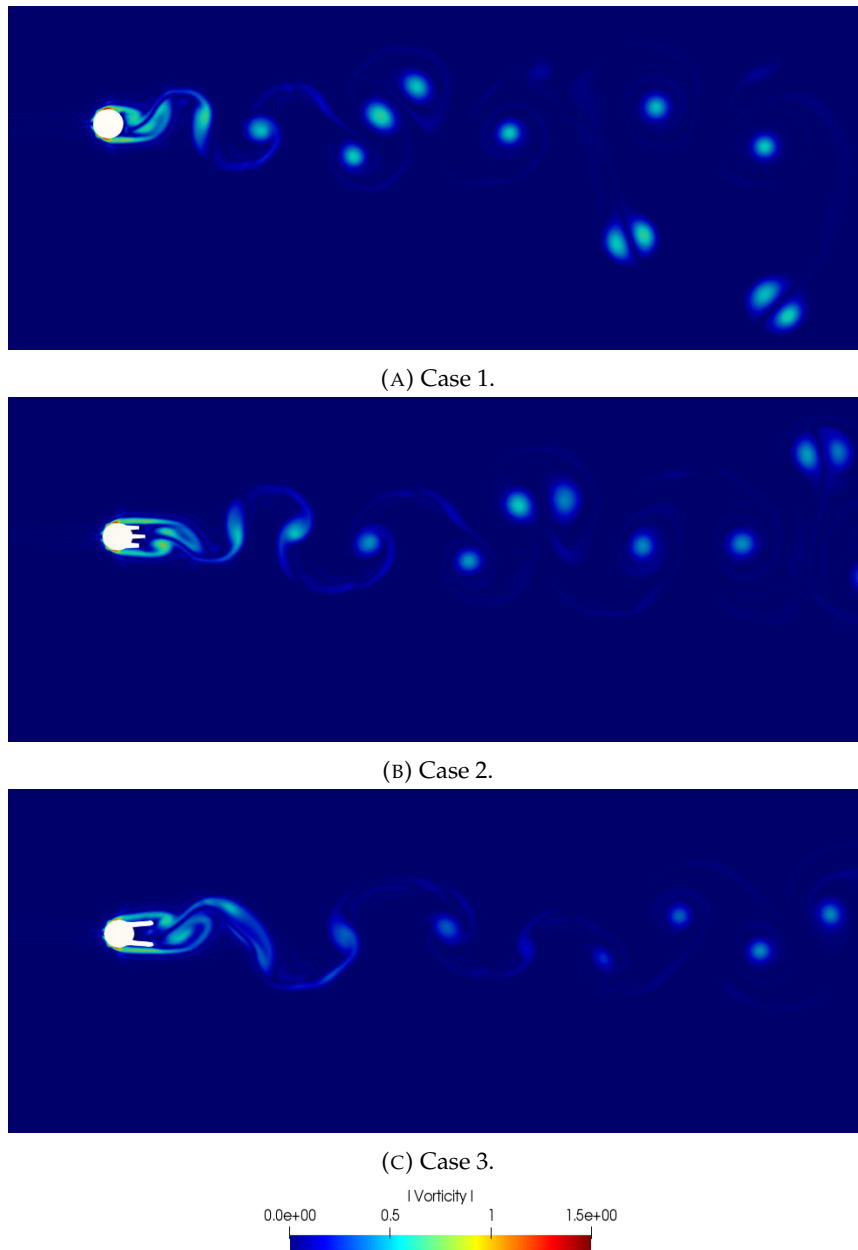


FIGURE 2.14: Spread of the vorticity  $[1/\Delta t]$  in the wake behind a cylinder for Cases 1-3.

center-line. Figure 2.15 illustrates the flap displacement vs. time for Case 3. The black and red lines show the upper and lower flaps. In addition, the '\*' symbols indicate the times chosen to depict the state of the flaps in figure 2.16.

Figure 2.17 illustrates the spread of the vorticity in the street behind two twin cylinders (Cases 4-6) and  $Re = 4.7 \times 10^4$ . In Figure 2.17a, the contour plots show that the noise source for Case 4 is of dipolar nature. Far from the twin cylinders, however, the pattern of the vorticity changes. The use of three flaps limits their motion. The size and location of the vorticity change, especially when moving away



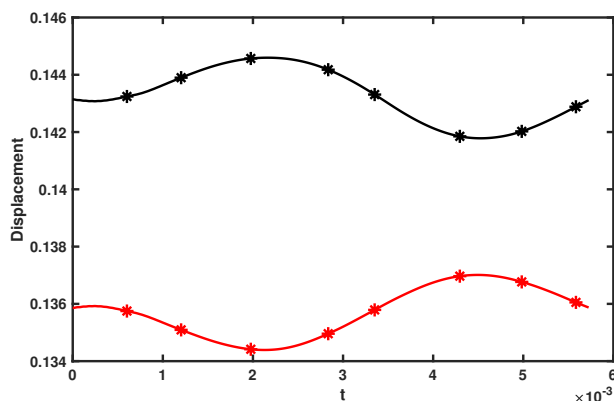


FIGURE 2.15: Displacement [m] vs. time [s]

from the twin cylinders as depicted in Figure 2.17b. By using the length  $L = 2r$  for flaps and letting them fluctuate as in Case 6, the arrangement of the vorticity in the wake changes considerably. Figure 2.17c demonstrates that the vorticity is broken into smaller pieces and its strength reduces. Therefore, there is a significant effect of such moving flaps on the flow over twin cylinders.

The point located at  $(0D, 0.63D)$  from the center of the single cylinder (or the upper cylinder in the twin-cylinder configurations) is selected for recording data to depict the sound pressure level (SPL), where  $D$  is the cylinder diameter. Figure 2.18 shows the SPL vs. frequency, computed by Fast Fourier transform, for  $Re = 4.7 \times 10^4$ . The SPL in dB is relative to the level of 20mPa. The figure shows that the cylinder without flaps has higher frequency, however, its SPL is lower than cylinders with 3 flaps. In addition, it shows that for twin cylinders,  $L = 2r$  and moving flaps, the frequency and the SPL reduce. It means that flaps with special characteristics can modify the shedding cycle past the cylinder, having an effect on the generated sound, and can reduce the wake deficit. Young's modulus has a great effect on the flexibility and the mobility of the flaps, resulting in changes in sound and flow patterns. Figure 2.19 shows the SPL vs. frequency for one cylinder with two flaps of length  $3r$  for two different Young's modulus ( $E_1 = 36.21 \times 10^6 \text{kg/ms}^2$ ,  $E_2 = 36.23 \times 10^6 \text{kg/ms}^2$ ) and  $Re = 4.7 \times 10^4$ . It should be noted that the Young's modulus is chosen to let flaps move but not touch each other. The less the Young's modulus, the higher the SPL and the frequency.

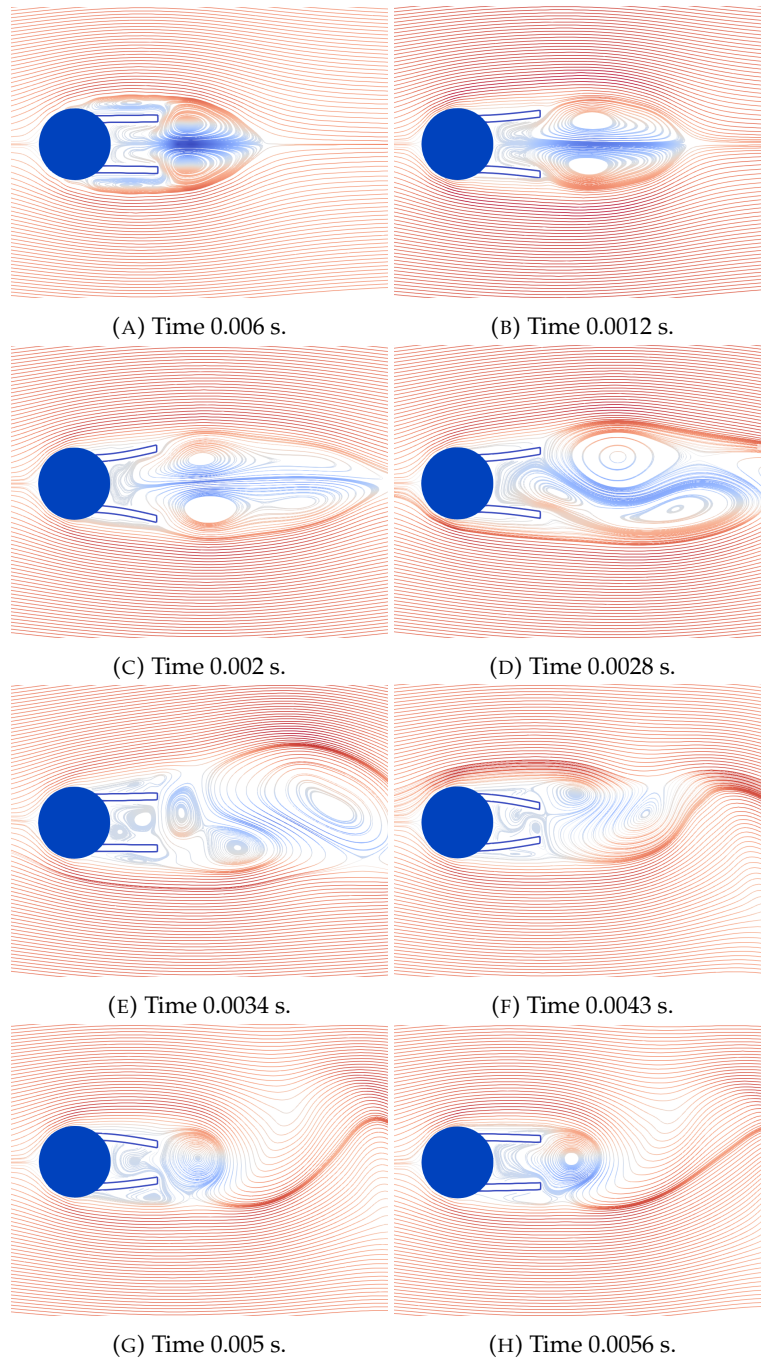


FIGURE 2.16: State of the flaps for eight selected times.

## 2.4 Conclusion

In this work a theoretical and numerical study of different types of sound wave propagation, their dissipation and dispersion rates, was carried out using the cumulant LBM. In addition, the cumulant LBM was coupled to a finite element method creating a FSI platform to model the effects of simpler splitter plates attached to the cylinder which look like hair on the flow and sound pattern in cylinder wakes.

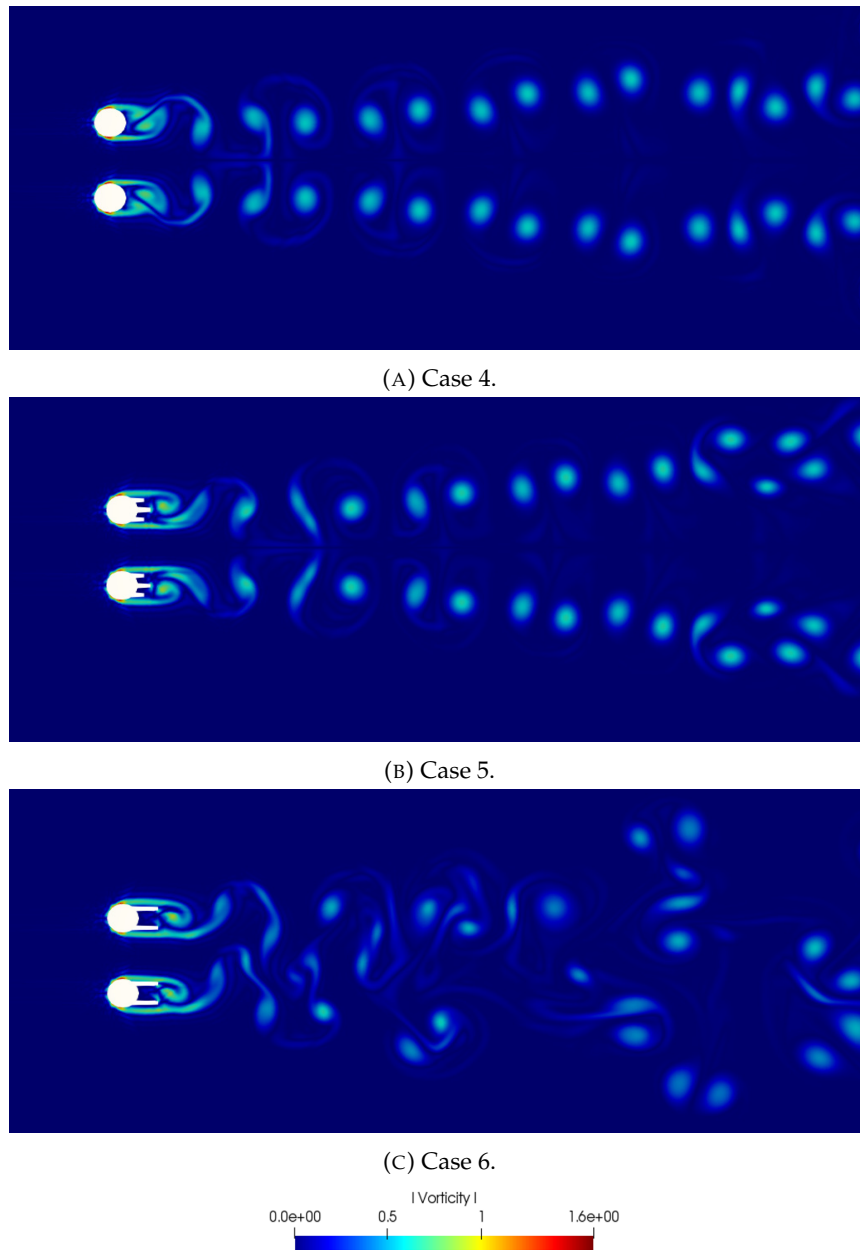
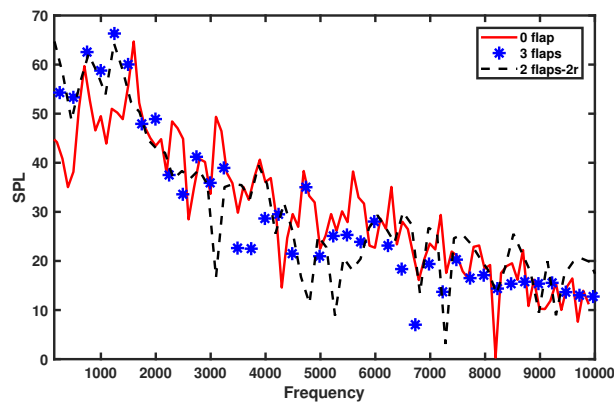


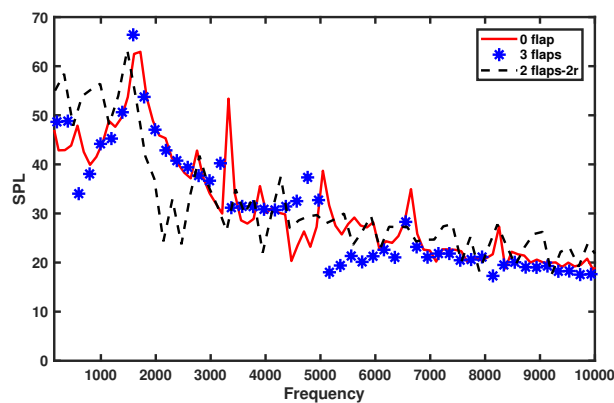
FIGURE 2.17: Spread of the vorticity  $[1/\Delta t]$  in the wake behind twin cylinders for Cases 4-6.

The temporal and spatial analyses of the acoustic properties for the standing plane wave and the Gaussian planar pulse show that the cumulant LBM reproduces the dissipation and dispersion rates of the theoretical solutions. In general, the phase speed and dissipation errors are almost constant, even for a relatively low resolution mesh, and they are independent of viscosity and fluid regime, but a function of the number of points per wavelength.

The comparison with analytical solutions shows that the cumulant LBM correctly reproduces the spherical acoustic pulse wave propagation, as well as the infinite



(A) Single cylinder cases.



(B) Twin cylinder cases.

FIGURE 2.18: Sound pressure level [dB] as a function of frequency [Hz].

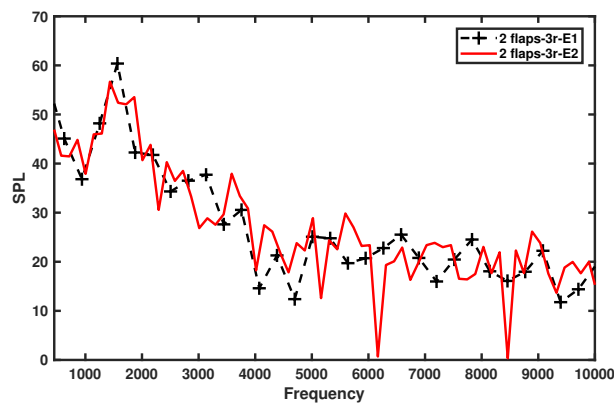


FIGURE 2.19: Sound pressure level [dB] as a function of frequency [Hz] for single cylinder case

spherical wave emitted from a point source. However, the BGK LBM has difficulties reproducing infinite spherical wave propagation. The solution displays chaotic behavior due to a numerical instability at low viscosities.

The FSI study of the effect of flaps on the vorticity and the frequency of the flow

pattern using the cumulant LBM ends up with the idea that the mobility of such flaps is one of the major factors altering the phase within the vortex shedding cycle. They reduce the transversal dislocation of the shed vorticity, causing the vortices being shed in a row along the center-line of the flow over a single cylinder.

As a final conclusion, the cumulant LBM correctly predicts the aerodynamic, hydrodynamic, and acoustic characteristics of different phenomena at high  $Re$  and different flow regimes in a simple way without additional computational cost.

## Chapter 3

# The local radial point interpolation cumulant LBM

The lattice Boltzmann method (LBM) has recently been used to simulate wave propagation, one of the challenging aspects of wind turbine modeling and simulation. However, standard LB methods suffer from the instability that occurs at low viscosities and from its characteristic lattice uniformity, which results in issues of accuracy and computational efficiency following mesh refinement. The local radial point interpolation cumulant lattice Boltzmann method (LRPIC-LBM) is proposed in this work to overcome these shortcomings. The LB equation is divided into collision and streaming steps. The collision step is modeled by the cumulant method, one of the most stable LB methods at low viscosities. In addition, the streaming step, which is naturally a pure advection equation, is discretized in time and space using the Lax-Wendroff scheme and the local radial point interpolation method (RPIM), a mesh free method. We describe the propagation of planar acoustic waves, including the temporal decay of a standing plane wave and the spatial decay of a planar acoustic pulse. The analysis of these specific benchmark problems has yielded qualitative and quantitative data on acoustic dispersion and dissipation, and their deviation from analytical results demonstrates the accuracy of the method. We found that the LRPIC-LBM replicates the analytical results for different viscosities, and the errors of the fundamental acoustic properties are negligible, even for quite low resolutions. Thus, this method may constitute a useful platform for effectively predicting complex engineering problems such as wind turbine simulations, without parameter dependencies such as the number of points per wavelength  $N_{ppw}$  and resolution  $\sigma$

or the detrimental effect caused by the use of coarse grids found in other accurate and stable LB models.

### 3.1 Introduction

Evidences of early sailing boats on the Nile and of Persian pumps and mills from the first century B.C. show humans were interested in Wind Energy since ancient times (138). In general, a wind turbine is defined as a device which converts the wind's kinetic energy into electrical energy (139, 140). It plays a key role on producing intermittent renewable energy and implementing a strategy to lower costs and reducing the reliance on fossil fuels (141, 142). Wind turbines have unique aerodynamic and aeroacoustic behavior that makes their prediction most challenging (15, 16), particularly their simulation needs an enormous number of grid points or cells, and long enough time samples (17). Researchers and centers such as the National Renewable Energy Laboratory (NREL) and the National Wind Technology Center (NWTC) have initiated multi-year programs on aeroacoustic wind turbine modeling (18) to develop efficient and appropriate computational aeroacoustic (CAA) implementations. Among particular issues specified to wind turbine problems, the propagation of sound is always a significant computational challenge (143, 144). With this aim, different numerical approaches were developed in the field of computational aeroacoustics. Tam (19) and Wells et al. (20) proposed popular numerical schemes such as compact and non-compact optimized schemes like the high-order compact difference scheme (21) and the dispersion-relation-preserving (DRP) scheme (22). Cheong et al. proposed grid-optimized dispersion-relation-preserving (GODRP) schemes for aeroacoustic simulations (23). Due to the huge cost of CAA simulations, hybrid methods using two sets of equations, one for the flow and another one for the acoustic disturbance field were developed (24).

Direct aerostatic simulations are computer-intensive due to the small ratio between sound pressure and pressure variation as a whole, the spreading of acoustic fields over a large area, and the time-consuming nature of traditional methods (25). As an illustration, the direct numerical simulation of waves using Navier-Stokes

equations requires schemes of fifth-order accuracy in space and fourth order accuracy in time (26, 27). Therefore, the lattice Boltzmann method (LBM), an explicit time marching scheme (8), has been widely used as an alternative to simulate sound wave propagation due to its kinetic nature, relative simplicity of implementation and parallelization. The LBM as a mesoscopic method uses probability density functions (probability of finding particles within a certain range of velocities at a certain range of locations at a given time) to model the momentum distribution in discrete space, thereby economizing computer resources (1). Buick et al. (28) and Dellar et al. (29) studied sound wave propagation using LBM and achieved acceptable results. Bres et al. (30) and Gorakifard et al. (145) presented the dissipation and dispersion of acoustic waves using the BGK-LBM and the cumulant LBM, respectively. Furthermore, a regularized method for the BGK-LBM (31) and the recursive and regularized LBM (LBM-rrBGK) (32, 33) have been developed to model wave propagation.

One of the drawbacks of the LBM is lattice uniformity, originated from symmetric lattice velocity models such as the square and cubic lattice meshes in 2D/3D simulations (146). Lattice uniformity causes the streaming step to occur at uniform neighboring grid points. Thus, the LBM is only applied to uniform meshes, whereas issues of accuracy and computational efficiency mainly affect simulations of problems that require non-uniform meshes. For example, numerical simulations with curved and irregular boundaries, common in wind turbine simulations, encounter difficulties when fitting the grids to the boundaries or adapting complex computational domains. Grid refinement schemes or adaptive LBM can help to simulate curved and moving boundaries more accurately (42). Wood (147) used refinement in LBM simulations to analyze wind energy and utilized adaptive LBM for moving boundaries (148). However, these schemes are associated with higher computational costs and even additional perturbations in acoustical problems (43).

Generally, the methods commonly used along with the LBM on non-uniform meshes include three distinct categories (149). The first is the interpolation supplemented LBM (IS-LBM) (44, 45). This method adds an interpolation step to the collision and streaming steps of the LBM. Two major drawbacks of the IS-LBM are its inefficiency due to the need to interpolate at each time-step, and the appearance of negative particle distributions (150). The second method is the combination of



the LBM with the finite difference method (46), finite volume methods (47–49), or finite element methods (50–52) used to stabilize the computation. The third method is the Taylor-series expansion and least-squares-based lattice Boltzmann method (53, 54) instead of direct interpolation. These methods, the implementation of which is somewhat simple, use continuous distribution functions in physical space.

Although the above numerical schemes show robustness for complex problems, they are affected by the inherent shortcomings of using meshes in numerical methods, such as the enormous cost of generating meshes, the low level of stress accuracy in fluid-structure interaction simulations (FSI) (119), obstacles in the adaptive analysis, and limitations in simulations of physical phenomena with singular, or nearly singular behavior. Mesh-free or meshless methods have been devised to eliminate mesh-related problems (151). The MFree method based on Liu’s definition (152) is “a method that generates a system of algebraic equations for the entire problem domain without consideration of a predefined mesh.” This means that the method needs a set of scattered nodes inside the problem domain and on the boundaries of the domain called field nodes. In addition, the relationship between the nodes for the interpolation or approximation of the unknown field variables is not required (151). Some of these well-known methods are the local point interpolation method (LPIM) (153), the local radial point interpolation method (LRPIM) (154), and the meshless local Petrov-Galerkin method (MLPG) (68, 155).

The coupling of LBM and MFree methods has achieved acceptable results in some applications (71–73, 156); however, this approach is at an early stage of development and must be improved to address instability in low viscosities and high Re numbers. A key point in the stability and the accuracy of these methods is the collision operator, which is not remarkable in early LB methods such as the BGK model and the multi-relaxation times (MRT) model (6), both of which also violate the principle of Galilean invariance. Therefore, using a suitable collision operator to simulate complex engineering problems accurately has been recognized as a necessity. The advent of the more stable cumulant LBM (5, 75) could dramatically improve MFree-LB methods and contribute to their advancement as powerful numerical tools for complex simulations.

The aim of this work is to study the capability of the local radial point interpolation cumulant LBM (LRPIC-LBM) to simulate the propagation of planar acoustic waves, including the temporal decay of a standing plane wave and the spatial decay of a planar acoustic pulse of Gaussian shape and calculate the deviation from theoretical results, and to determine whether this method might be useful for wind turbine problems. The LB equation is deconstructed into collision and streaming parts. The collision step is performed by means of the cumulant method. The streaming step, which represents a pure advection equation, is discretized first in time using the Lax-Wendroff scheme, and then in space using the local radial point interpolation method (RPIM).

### 3.2 The lattice Boltzmann method

The lattice Boltzmann method (LBM) is obtained from the kinetic theory of gases. In the LBM, a key point for modeling the momentum distribution in discrete space is the use of probability density functions (1). The lattice Boltzmann equation without an external force is

$$f_i(\mathbf{x} + \mathbf{c}_i \Delta t, t + \Delta t) - f_i(\mathbf{x}, t) = \Omega_i \quad (3.1)$$

where  $\mathbf{x}$  and  $\mathbf{c}_i$  are vectors of the position and lattice speed and  $f_i$  is the particle distribution function and  $\Omega_i$  is the collision operator.

In general, the LBM consists of collision and streaming steps. In the local radial point interpolation cumulant LBM (LRPIC-LBM), the cumulant method is used for the collision part and the local radial point interpolation method (RPIM) is used for the streaming parts.

#### 3.2.1 Collision Step

The cascade method has been proposed (10, 157) as a way to overcome the instability problems and modeling artifacts of previous LB methods. However, it is hindered by the effects of lower order moments over higher order moments. The cumulant method, presented by Seeger to solve the Boltzmann equation (12, 13), effectively

resolves these issues. Cumulants can be efficiently generated from central moments. The cumulant method for solving the LBM is described in section 2.2.1.

### 3.2.2 Streaming Step

To model the streaming step, the second most important part of the LBM, a pure advection equation is normally solved from a Lagrangian approach within uniform structured meshes with CFL numbers equal to one. However, considering the Eulerian perspective for the calculation can effectively resolve this step when meshes are non-uniform and unstructured. The pure advection equation is

$$\frac{\partial f_i}{\partial t} + c_{i,\alpha} \frac{\partial f_i}{\partial x_\alpha} = 0, \quad (3.2)$$

One alternative is a semi-discrete formulation with time and space derivatives discretized separately. Thus, equation (3.2) is discretized using the explicit Lax-Wendroff scheme in time, followed by the local radial point interpolation method (LRPIM) in space. In addition, it is important to approximate the unknown field functions using trial (shape) functions as an approximate solution for the partial differential equation.

#### MFfree shape function construction – Radial point interpolation shape functions

Radial point interpolation method (RPIM) shape functions were developed to circumvent the singularity problem arising in the point interpolation method (PIM). The RPIM interpolation augmented with polynomials is

$$f^h(\mathbf{x}, t) = \sum_{i=1}^n R_i(\mathbf{x}) a_i(t) + \sum_{j=1}^m p_j(\mathbf{x}) b_j(t) = \mathbf{R}^T(\mathbf{x}) \mathbf{a}(t) + \mathbf{p}^T(\mathbf{x}) \mathbf{b}(t) \quad (3.3)$$

where  $R_i(\mathbf{x})$  is a radial basis function (RBF), and  $p_j(\mathbf{x})$  is monomial in the coordinate space  $x^T = [x, y]$ :  $\mathbf{R}^T = [R_1(\mathbf{x}) R_2(\mathbf{x}) \cdots R_n(\mathbf{x})]$  and  $\mathbf{p}^T = [p_1(\mathbf{x}) p_2(\mathbf{x}) \cdots p_m(\mathbf{x})]$ . Parameters  $n$  and  $m$  are the number of RBFs and polynomial basis functions. Variables  $a_i$  and  $b_j$  are time dependent unknown coefficients. It should be noted that the independent variable in RBF  $R_i(\mathbf{x})$  is the distance between the point of interest  $\mathbf{x}$  and a node at  $\mathbf{x}_i$ .

Different radial basis functions (RBF), and their characteristics have been studied extensively in the meshless RPIM. In this work, the multi-quadrics (MQ) function is used as

$$R_i = \left( r_i^2 + (\alpha_c d_c)^2 \right)^q \quad (3.4)$$

where  $\alpha_c = 1.0$ ,  $q = 1.03$ , and  $d_c = 3.0$ .

To determine the  $n + m$  unknown coefficients in equation (3.3), some specific constraint equations and the Kronecker delta function property are dictated. These constraints are

$$\sum_{i=1}^n p_j(x_i) a_i(t) = \mathbf{P}_m^T \mathbf{a}(t) = 0, \quad j = 1, 2, \dots, m \quad (3.5)$$

where

$$\mathbf{P}_m^T = \begin{bmatrix} 1 & 1 & \cdots & 1 \\ x_1 & x_2 & \cdots & x_n \\ y_1 & y_2 & \cdots & y_n \\ \vdots & \vdots & \ddots & \vdots \\ p_m(x_1) & p_m(x_2) & \cdots & p_m(x_n) \end{bmatrix} \quad (3.6)$$

Thus, the approximation function can be obtained as

$$f^h(\mathbf{x}, t) = \sum_{i=1}^n \phi_i(\mathbf{x}) f_i(t) = \mathbf{\Phi}(\mathbf{x}) \mathbf{F}(t) \quad (3.7)$$

where  $\mathbf{F}$  is a vector containing the nodal values of the distribution function and  $\mathbf{\Phi}$  is a vector containing the first  $n$  components of the  $\tilde{\mathbf{\Phi}}$  vector

$$\tilde{\mathbf{\Phi}} = \left[ \mathbf{R}^T \mathbf{p}^T \right] \mathbf{G}^{-1} \quad (3.8)$$

where

$$\mathbf{G} = \begin{bmatrix} \mathbf{R}_0 \mathbf{P}_m \\ \mathbf{P}_m^T \mathbf{0} \end{bmatrix}, \quad (3.9)$$

$$\mathbf{R}_0 = \begin{bmatrix} R_1(r_1) & R_2(r_1) & \cdots & R_n(r_1) \\ R_1(r_2) & R_2(r_2) & \cdots & R_n(r_2) \\ \vdots & \vdots & \ddots & \vdots \\ R_1(r_n) & R_2(r_n) & \cdots & R_n(r_n) \end{bmatrix}, \quad (3.10)$$

$$r_k = \sqrt{(x_k - x_i)^2 + (y_k - y_i)^2}. \quad (3.11)$$

### Semi-discrete formulation – Time discretization

The Taylor series expansion of the particle distributions is

$$f_i^{n+1} = f_i^n + \Delta t \left. \frac{\partial f_i}{\partial t} \right|^n + \frac{\Delta t^2}{2} \left. \frac{\partial^2 f_i}{\partial t^2} \right|^n + O(\Delta t^3), \quad (3.12)$$

where here  $n$  refers to the time step. Substituting the time derivatives in terms of the  $t$  derivatives up to second order results in the time discretization of equation (3.2) based on the Lax-Wendroff scheme,

$$f_i^{n+1} = f_i^n - \Delta t c_{i,\alpha} \frac{\partial f_i^n}{\partial x_\alpha} + \frac{\Delta t^2}{2} c_{i,\alpha} c_{i,\beta} \frac{\partial^2 f_i^n}{\partial x_\alpha \partial x_\beta}. \quad (3.13)$$

### Semi-discrete formulation – Space discretization

The local radial point interpolation method (LRPIM) was developed to avoid the side effects of using global background cells in the global weak-form. In this method, the numerical integration is performed within the local domain consisting of a set of distributed nodes. The LRPIM is based on the RPIM shape functions with the delta function property. The main advantage of the LRPIM is the excellent interpolation stability of RBFs.

MFree local weak-form methods use the weak form of the problem obtained from the method of weighted residuals (MWR). The weighted residual statement of equation (3.13) on the local domain  $\Omega_I$  of point  $I$  bounded by  $\Gamma_I$  is posed as

$$\begin{aligned} \int_{\Omega_I} w_I f_i^{n+1} d\Omega &= \int_{\Omega_I} w_I f_i^n d\Omega - \Delta t \int_{\Omega_I} w_I c_{i,\alpha} \frac{\partial f_i^n}{\partial x_\alpha} d\Omega \\ &+ \frac{\Delta t^2}{2} \int_{\Omega_I} w_I c_{i,\alpha} c_{i,\beta} \frac{\partial^2 f_i^n}{\partial x_\alpha \partial x_\beta} d\Omega \end{aligned} \quad (3.14)$$

where  $w_I$  is the local weight function of node  $I$  considered as

$$w_I(r) = \begin{cases} \frac{2}{3} - 4r^2 + 4r^3 & r \leq 0.5 \\ \frac{4}{3} - 4r + 4r^2 - \frac{4}{3}r^3 & 0.5 < r \leq 1 \\ 0 & r > 1 \end{cases} \quad (3.15)$$

where  $r = |x - x_i| / d^{\max}$  and  $d^{\max}$  is the radius of the compact support. Equation (3.14) is applied to all nodes in the problem domain.

To work with a continuous approximate solution, it is necessary to decrease the differentiation requirements of the unknown in the weighted residual statement by employing integration by parts in equation (3.14),

$$\begin{aligned} \int_{\Omega_I} w_I f_i^{n+1} d\Omega &= \int_{\Omega_I} w_I f_i^n d\Omega - \int_{\Omega_I} \left( \Delta t w_I c_{i,\alpha} \frac{\partial f_i^n}{\partial x_\alpha} + \frac{\Delta t^2}{2} c_{i,\alpha} c_{i,\beta} \frac{\partial w_I}{\partial x_\beta} \frac{\partial f_i^n}{\partial x_\alpha} \right) d\Omega \\ &+ \frac{\Delta t^2}{2} \int_{\Gamma_I} w_I c_{i,\alpha} c_{i,\beta} \frac{\partial f_i^n}{\partial x_\alpha} n_\beta d\Gamma \end{aligned} \quad (3.16)$$

where  $\Gamma_I$  is the boundary of the local domain  $\Omega_I$  and  $n_\beta$  is the unit outward normal vector.

Substitution of the approximate solution given in equations (3.7) into the weak form given by equation (3.16) leads to

$$\sum_{j=1}^{N_I} \mathbf{M}_{IJ} f_{i,j}^{n+1} = \sum_{j=1}^{N_I} [\mathbf{M}_{IJ} + \mathbf{K}_{i,IJ}] f_{i,j}^n \quad (3.17)$$

where  $\mathbf{M}_{IJ}$  and  $\mathbf{K}_{i,IJ}$  are the nodal mass and stiffness matrix, respectively, defined as

$$\mathbf{M}_{IJ} = \int_{\Omega_I} w_I \Phi_J \, d\Omega \quad (3.18)$$

$$\mathbf{K}_{i,IJ} = - \int_{\Omega_I} \left( \Delta t w_I + \frac{\Delta t^2}{2} c_{i,\beta} \frac{\partial w_I}{\partial x_\beta} \right) c_{i,\alpha} \frac{\partial \Phi_J}{\partial x_\alpha} \, d\Omega + \frac{\Delta t^2}{2} \int_{\Gamma_I} w_I c_{i,\alpha} \frac{\partial \Phi_J}{\partial x_\alpha} c_{i,\beta} n_\beta \, d\Gamma \quad (3.19)$$

Thus, the global equation system for all nodes in the entire domain is obtained as

$$\mathbf{M} \mathbf{f}_i^{n+1} = [\mathbf{M} + \mathbf{K}_i] \mathbf{f}_i^n \quad (3.20)$$

where  $\mathbf{M}$ ,  $\mathbf{K}$ , and  $\mathbf{f}_i$  are the global mass matrix, stiffness matrix, and particle distribution vector, respectively. This system has  $N$  equations with  $N$  unknowns which is solved separately for each direction.

To numerically evaluate the area and the curve integrals in equations (3.18) and (3.19) the Gauss quadrature scheme is used as follows

$$\mathbf{M}_{IJ} = \sum_{k=1}^{n_g} \tilde{w}_k w_I(x_k) \Phi_J(x_k) \left| J^{\Omega_I} \right| \quad (3.21)$$

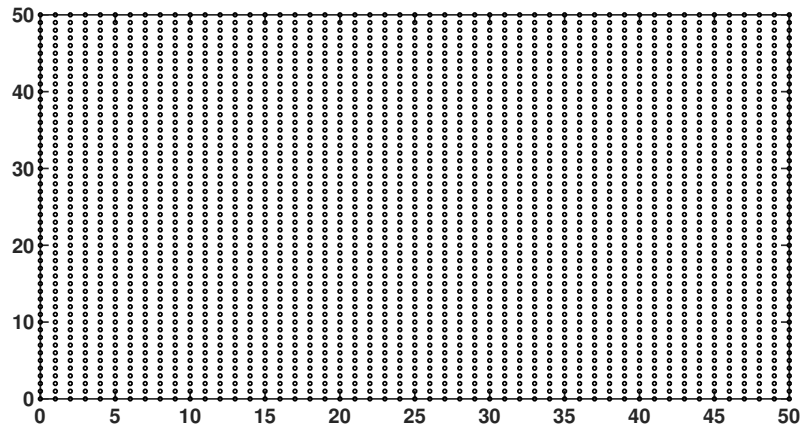
$$\begin{aligned} \mathbf{K}_{i,IJ} = & - \sum_{k=1}^{n_g} \tilde{w}_k \left( \Delta t w_I(x_k) + \frac{\Delta t^2}{2} c_{i,\beta} \frac{\partial w_I}{\partial x_\beta} \Big|_{x_k} \right) c_{i,\alpha} \frac{\partial \Phi_J}{\partial x_\alpha} \Big|_{x_k} \left| J^{\Omega_I} \right| \\ & + \frac{\Delta t^2}{2} \sum_{k=1}^{n_g^b} \tilde{w}_k w_I(x_k) c_{i,\alpha} \frac{\partial \Phi_J}{\partial x_\alpha} \Big|_{x_k} c_{i,\beta} n_\beta \left| J^{\Gamma_I} \right| \end{aligned} \quad (3.22)$$

where  $n_g$  and  $n_g^b$  are the total number of Gauss points in the quadrature domain and boundaries,  $\tilde{w}_k$  is the Gauss weight factor for Gauss point  $x_k$ ,  $J^{\Omega_I}$  and  $J^{\Gamma_I}$  are the Jacobian matrix for the domain and boundary integrations, respectively.

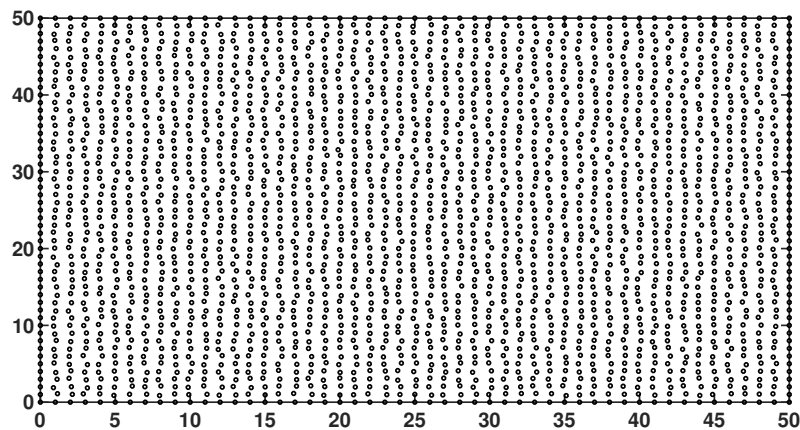
### 3.3 Results and Discussion

One of the complicated phenomena that has recently received major interest from researchers using the LBM is wind turbine aeroacoustics (147, 148, 158, 159), which can be directly simulated without additional computational cost. In this section, our aim is to demonstrate the standard analysis procedure using the local radial point

interpolation cumulant lattice Boltzmann method (LRPIC-LBM) to predict acoustic properties for benchmark cases. Thus, numerical studies are conducted for the propagation of planar acoustic waves, concentrating on numerical dissipation and dispersion. A quantitative assessment of the method's two setups, including the temporal decay of a standing plane wave in a periodic domain and the spatial decay of a propagating planar acoustic pulse of Gaussian shape for regular and irregular nodal distributions (shown in Figures 3.1a and 3.1b) are discussed below. It should be noted that the default nodal arrangement is a regular distribution; the base units are in the LB system.



(A) Regular nodes.



(B) Irregular nodes.

FIGURE 3.1: Nodal arrangement for the propagation of planar acoustic waves in LRPIC-LBM simulations.



### 3.3.1 Planar standing wave

As an initial case study, we performed a temporal analysis on a standing plane acoustic wave in a periodic domain. The dissipation and dispersion relations based on the temporal analysis as represented in subsection 2.3.1 are

$$c_T = \zeta_s \sqrt{1 - \left(\frac{k\nu}{\zeta_s}\right)^2}, \quad (3.23a)$$

$$\alpha_T = k^2\nu \quad (3.23b)$$

where  $k$  is the wave number. The assumptions for this set-up are presented in Table 3.1. They were chosen as in reference (145) for ease of comparison.

TABLE 3.1: Parameters for the planar standing wave

Variables	$p'(x, y, 0)$	$\rho'$	$u'$	$v'$	A
Description	$A \sin\left(\frac{2\pi x}{\lambda}\right)$	$\frac{\rho'}{\zeta_s}$	$\frac{p'}{\rho_0 \zeta_s}$	0	$10^{-3} p_0$

The acoustic pressure at time  $t$  is (145)

$$p'(x, y, t) = A \exp[-\alpha_T t] \sin[k(x - c_T t)] \quad (3.24)$$

It should be noted that the results of the temporal analysis can be considered as a function of the number of points per wavelength  $N_{ppw} = \lambda/\Delta x$  or the non-dimensional wave-number  $k\Delta x = 2\pi/N_{ppw}$ .

In accordance with the concepts discussed in (145) to study the accuracy of the propagation of waves using the local radial point interpolation cumulant lattice Boltzmann method (LRPIC-LBM), various viscosities and different resolutions (i.e. the number of points per wavelength) were studied. Figure 3.2 shows the acoustic pressure time history for  $\nu = 1.0 \times 10^{-2} [\frac{\Delta x^2}{\Delta t}]$  with  $N_{ppw} = 12$  points per wavelength. The analytical result is represented by a solid black line, whereas the cumulant LBM and the LRPIC-LBM are shown with a red dashed line and a blue five-pointed star, respectively. The deviations of the numerical phase speed and the temporal dissipation rate from the theoretical values are less than one percent for the BGK LBM (30)

and the cumulant LBM (145) for resolutions lower than 12 points per wavelength. However, the LRPIC-LBM exhibits even better behavior in predicting the acoustic pressure of the analytical values.

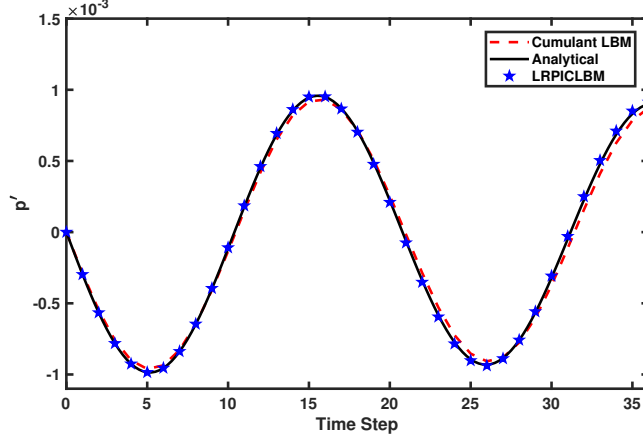


FIGURE 3.2: Acoustic pressure  $[\frac{kg}{\Delta x \Delta t^2}]$  versus time step  $[\Delta t]$  for  $\nu = 1.0 \times 10^{-2} [\frac{\Delta x^2}{\Delta t}]$  with  $N_{ppw} = 12$  points per wavelength.

The acoustic pressure time history for  $\nu = 1.0 \times 10^{-4} [\frac{\Delta x^2}{\Delta t}]$  with  $N_{ppw} = 12$  points per wavelength is presented in Figure 3.3. It shows the comparison between the analytical solution, the cumulant LBM and the LRPIC-LBM numerical solution at low viscosities. One of the most problematic issues in the BGK LBM is the low viscosity limit, which makes the solution unstable. However, the cumulant LBM, with phase speed and temporal dissipation rate errors of less than 1 percent, as in reference (145), did not present difficulties at low viscosity. Although both approaches were successful, the new method exhibited better performance, closely following the theoretical result for the same viscosity value.

An important characteristic highlighted by some researchers (30, 145) is that these numerical deviations are only a function of  $N_{ppw}$  and are independent of other parameters such as frequency and viscosity. They found that the errors of the BGK (30) and the cumulant LBM (145) are about 7 percent for  $N_{ppw} = 4$ . However, the acoustic pressure time history for  $\nu = 1.0 \times 10^{-2} [\frac{\Delta x^2}{\Delta t}]$  with  $N_{ppw} = 4$  points per wavelength illustrated in Figure 3.4 for the analytical solution, the cumulant LBM and the LRPIC-LBM reveals that the deviation is less than 2 percent for the LRPIC-LBM, with  $\Delta t = 0.25$ . Thus, the LRPIC-LBM is much more successful in predicting theoretical results even with a low number of points per wavelength.

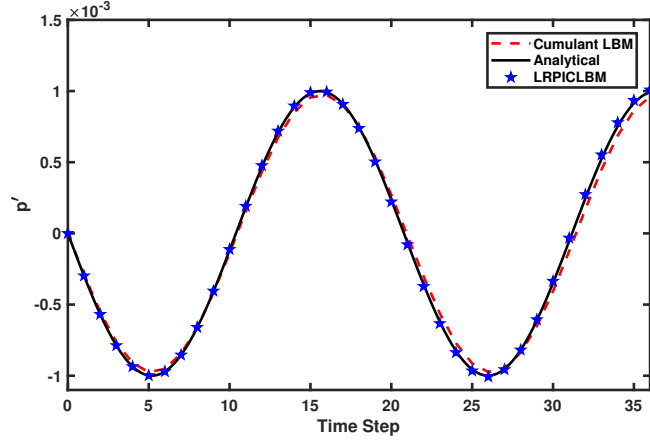


FIGURE 3.3: Acoustic pressure  $[\frac{kg}{\Delta x \Delta t^2}]$  versus time step  $[\Delta t]$  for  $\nu = 1.0 \times 10^{-4} [\frac{\Delta x^2}{\Delta t}]$  with  $N_{ppw} = 12$  points per wavelength.

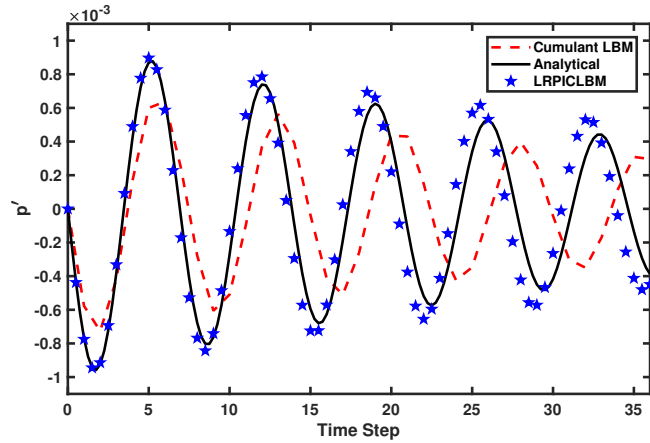


FIGURE 3.4: Acoustic pressure  $[\frac{kg}{\Delta x \Delta t^2}]$  versus time step  $[\Delta t]$  for  $\nu = 1.0 \times 10^{-2} [\frac{\Delta x^2}{\Delta t}]$  with  $N_{ppw} = 4$  points per wavelength with  $\Delta t = 0.25$ .

The choice of the time step size has an influence on the accuracy and stability of the solution. A smaller time step leads to more accurate results, especially in a hyperbolic partial differential equation (PDE). To minimize the phase speed and dissipation rate errors, the time step was reduced. Figure 3.5 shows the acoustic pressure time history for  $\nu = 1.0 \times 10^{-2} [\frac{\Delta x^2}{\Delta t}]$  with  $N_{ppw} = 4$  points per wavelength and  $\Delta t = 0.1$ . The LRPI-CLBM replicates the analytical results with negligible errors. Therefore, this method makes it possible to predict wave motion more accurately with no dependency on the number of points per wavelength  $N_{ppw}$ .

Although the results of the propagation of acoustic waves for regular nodal distributions were good, it is important to adequately estimate accuracy when considering irregular nodes (Figure 3.1b). The acoustic pressure time history for  $\nu =$

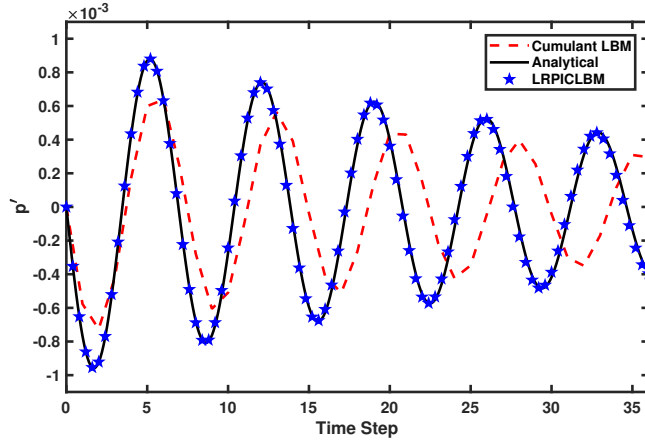


FIGURE 3.5: Acoustic pressure  $[\frac{kg}{\Delta x \Delta t^2}]$  versus time step  $[\Delta t]$  for  $\nu = 1.0 \times 10^{-2} [\frac{\Delta x^2}{\Delta t}]$  with  $N_{ppw} = 4$  points per wavelength with  $\Delta t = 0.1$ .

$1.0 \times 10^{-2} [\frac{\Delta x^2}{\Delta t}]$  with  $N_{ppw} = 12$  points per wavelength is presented in Figure 3.6. The results show that the local radial point interpolation cumulant lattice Boltzmann method (LRPIC-LBM) with irregular nodal distributions again very closely reproduced the analytical acoustic pressure.

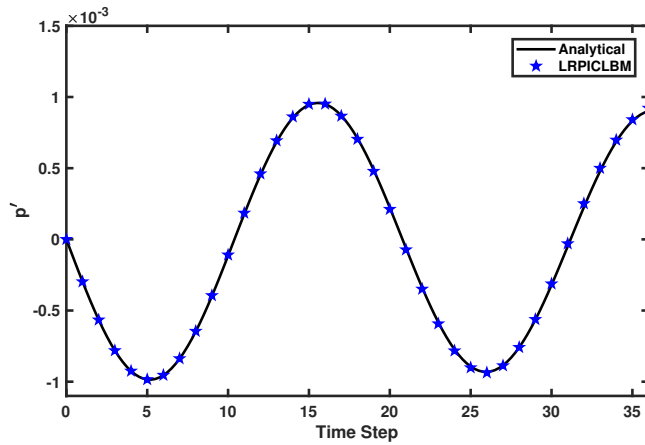


FIGURE 3.6: Acoustic pressure  $[\frac{kg}{\Delta x \Delta t^2}]$  versus time step  $[\Delta t]$  for  $\nu = 1.0 \times 10^{-2} [\frac{\Delta x^2}{\Delta t}]$  with  $N_{ppw} = 12$  points per wavelength with irregular nodal distributions.

### 3.3.2 Planar pulse wave

Next, we studied a planar pulse wave by replacing the plane wave with a Gaussian shape planar pulse, initially located at the center of the domain. The dissipation and

dispersion relationships derived from the spatial analysis as represented in subsection 2.3.1 are

$$c_S = \sqrt{2}\zeta_s \sqrt{\frac{1 + (\omega\tau_s)^2}{\sqrt{1 + (\omega\tau_s)^2} + 1}}, \quad (3.25a)$$

$$\alpha_S = \frac{\omega}{\sqrt{2}\zeta_s} \sqrt{\frac{\sqrt{1 + (\omega\tau_s)^2} - 1}{1 + (\omega\tau_s)^2}}. \quad (3.25b)$$

The variables and parameters for this case are presented in Table 3.2. A planar pulse emits from the origin throughout the domain, where periodic boundary conditions are imposed.

TABLE 3.2: Parameters for the planar pulse wave

Variables	$p'(x, y, 0)$	$\rho'$	$u'$	$v'$	A	$\sigma$
Description	$A \exp\left(-\ln(2) \frac{x^2}{\sigma^2}\right)$	$\frac{\rho'}{\zeta_s^2}$	$\frac{p'}{\rho_0 \zeta_s}$	0	$10^{-3} p_0$	0.06 – 0.1

To assess the accuracy of the LRPIC-LBM in simulating the pulse wave emission, we proceeded as in reference (145). Different viscosities and resolutions (which are related to the choice of  $\sigma$ ) were studied. Figure 3.7 depicts the acoustic pressure time history for  $\nu = 1.0 \times 10^{-2} [\frac{\Delta x^2}{\Delta t}]$  with  $\sigma = 0.1$ . The cumulant LBM results (dashed red line) are compared to the LRPIC-LBM (solid black line). As stated in (30, 145) the intensity loss at any location is proportional to the distance of propagation, regardless of the precise location. Thus, the data were extracted from the center of the domain, and at 5, 11, and 17 nodes apart from the center. For resolutions up to  $\sigma = 0.1$ , deviations between the cumulant LBM and the LRPIC-LBM results were less than 1 percent.

The acoustic pressure time history for  $\nu = 1.0 \times 10^{-4} [\frac{\Delta x^2}{\Delta t}]$  with  $\sigma = 0.1$  is shown in Figure 3.8. It presents the comparison between the cumulant LBM and the LRPIC-LBM at low viscosity. While the standard BGK LBM creates instabilities and noisy results, less than 1 percent deviation was found between the cumulant LBM and this method, with stable behavior at low viscosities. In addition, as in the case of the temporal results shown in Figure 3.3, reducing the viscosity in the considered range

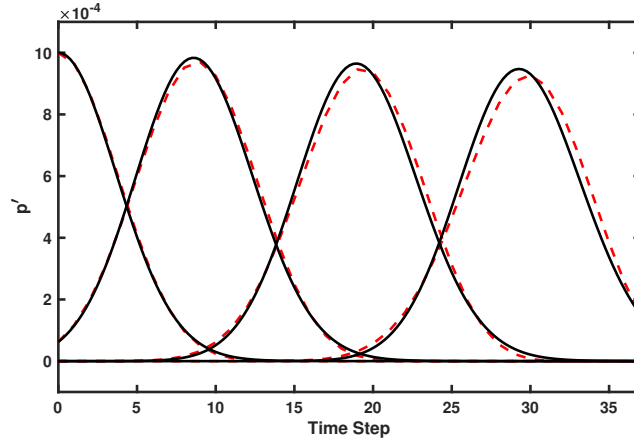


FIGURE 3.7: Acoustic pressure  $[\frac{kg}{\Delta x \Delta t^2}]$  versus time step  $[\Delta t]$  for  $\nu = 1.0 \times 10^{-2} [\frac{\Delta x^2}{\Delta t}]$  with  $\sigma = 0.1$ : the cumulant LBM (dashed red line), LRPIC-LBM (solid black line).

did not substantially impact the results.

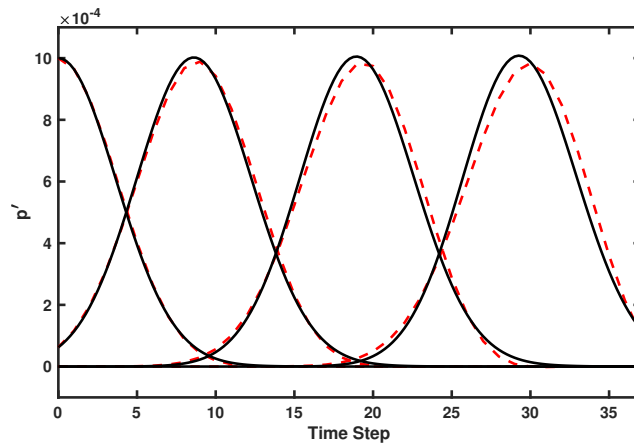


FIGURE 3.8: Acoustic pressure  $[\frac{kg}{\Delta x \Delta t^2}]$  versus time step  $[\Delta t]$  for  $\nu = 1.0 \times 10^{-4} [\frac{\Delta x^2}{\Delta t}]$  with  $\sigma = 0.1$ : the cumulant LBM (dashed red line), LRPIC-LBM (solid black line).

Like the parameter  $N_{ppw}$  introduced in the temporal analysis of the first set up,  $\sigma$  is another effective parameter used in spatial analysis which affects the accuracy of the LBM results. The acoustic pressure time history is depicted in Figure 3.9 for  $\nu = 1.0 \times 10^{-2} [\frac{\Delta x^2}{\Delta t}]$ , with  $\sigma = 0.06$ . It shows that the deviations between the cumulant LBM and the LRPIC-LBM results increase after the reduction of  $\sigma$ . The wiggling observed in the results of the cumulant LBM is due to the reduction of the number of nodes inside the pulse, which brings the accuracy of the results into question. However, the LRPIC-LBM graphs are smooth and unaffected by the lesser number

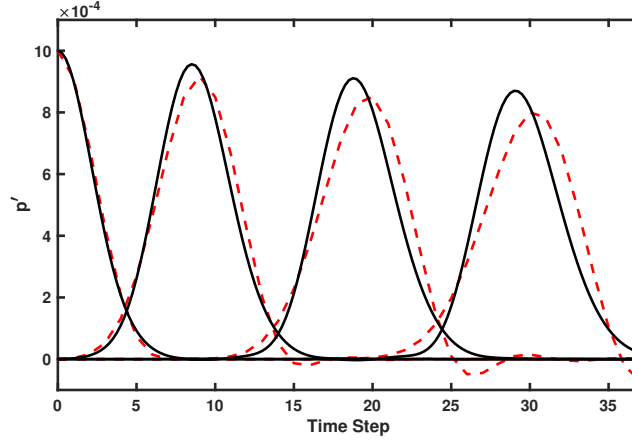


FIGURE 3.9: Acoustic pressure  $[\frac{kg}{\Delta x \Delta t^2}]$  versus time step  $[\Delta t]$  for  $\nu = 1.0 \times 10^{-2} [\frac{\Delta x^2}{\Delta t}]$  with  $\sigma = 0.06$ : the cumulant LBM (dashed red line), LRPIC-LBM (solid black line).

of nodes. To better assess the accuracy of the LRPIC-LBM compared to the cumulant LBM, the data shown in Figure 3.9 were compared with the analytical results. The Fourier transform of the pressure time history of the passing wave yields the Fourier coefficient of pressure  $\hat{p}'(x, \omega) = \hat{p}'(x, 0) \exp[-\alpha_S x] \exp[i\omega \frac{x}{c_S}]$  which is the solution to equation (2.31) (30). Figure 3.10 shows the ratio  $\hat{p}'(x, \omega) / \hat{p}'(x, 0)$  as a function of angular frequency for the analytical solution. This figure shows that the LRPIC-LBM is more successful than the cumulant LBM at predicting theoretical results with  $\sigma = 0.06$ . Thus, this method can model wave propagation more accurately even at smaller resolutions.

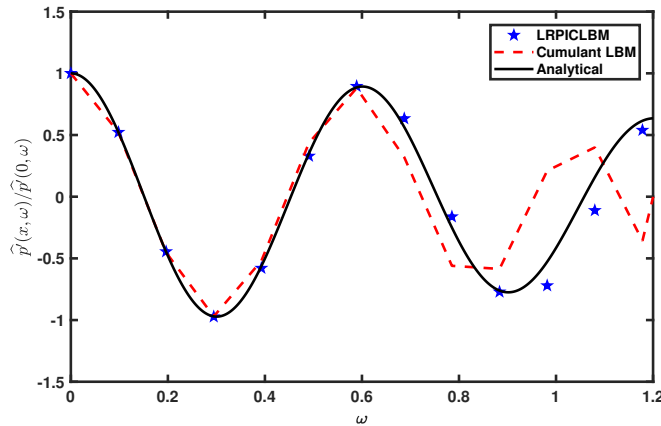


FIGURE 3.10: The ratio  $\hat{p}'(x, \omega) / \hat{p}'(x, 0)$  as a function of angular frequency  $[\frac{1}{\Delta t}]$  for the analytical solution, the cumulant LB and the LRPIC-LB methods.

Figure 3.11 illustrates the acoustic pressure time history for  $\nu = 1.0 \times 10^{-2} [\frac{\Delta x^2}{\Delta t}]$

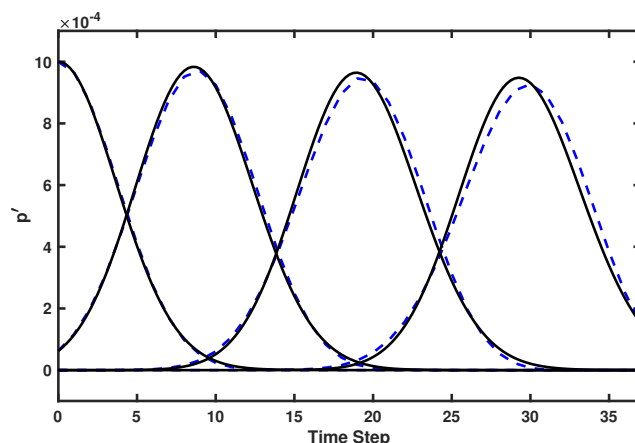


FIGURE 3.11: Acoustic pressure  $[\frac{kg}{\Delta x \Delta t^2}]$  versus time step  $[\Delta t]$  for  $\nu = 1.0 \times 10^{-2} [\frac{\Delta x^2}{\Delta t}]$  with  $\sigma = 0.1$  considering irregular nodal distributions: the cumulant LBM (dashed blue line), LRPIC-LBM (solid black line).

with  $\sigma = 0.1$  considering irregular nodes (Figure 3.1b). The cumulant LBM and the LRPIC-LBM results are represented by a dashed blue line and a solid black line, respectively. The data are extracted as in Figure 3.7. The results show that the LRPIC-LBM with irregular nodal distributions reproduced the behavior observed previously.

### 3.4 Conclusions

This work presents a numerical study of the propagation of acoustic waves, one of the challenging issues occurring in wind turbine simulations, that includes the temporal decay of a standing plane wave and the spatial decay of a planar acoustic pulse, using the local radial point interpolation cumulant lattice Boltzmann method (LRPIC-LBM). The LB equation is divided into collision, modeled by the cumulant method, and streaming, discretized in time and space, using the Lax-Wendroff scheme and the local radial point interpolation method (RPIM). The LRPIC-LBM results were compared with the cumulant LBM and the analytical solutions. Both methods showed a similar acoustic pressure time history, and the deviations for the phase speed and the dissipation rate were minor for high number of points per wavelength  $N_{ppw}$  and resolution  $\sigma$ . In addition, they showed that reduced viscosity does not affect the stability of either LB method due to the intrinsic characteristics of



the cumulant method. Unlike LB methods such as the BGK LBM and the cumulant LBM, the time history for the acoustic pressure and the phase speed and dissipation rate predicted by LRPIC-LBM showed considerably smaller errors for low  $N_{ppw}$  and  $\sigma$  due to the construction of the meshless method itself. Moreover, the LRPIC-LBM with irregular nodal distributions reproduces the same propagation of acoustic waves obtained with regular nodal distributions.

In summary, the freedom to scatter nodes based on problem conditions and the occurrence of sharp gradients plus the accuracy obtained from the RPIM along with the good stability and simplicity achieved by the cumulant LBM may provide an adequate platform with which to model wind turbine problems.

## Chapter 4

# The meshless local Petrov-Galerkin cumulant LBM

As we have emphasized in previous chapters, the lattice Boltzmann method (LBM) suffers from an instability at low viscosities and from having to compromise between accuracy and computational efficiency due to its lattice uniformity. Thus, here, the meshless local Petrov-Galerkin cumulant lattice Boltzmann method (MLPGC-LBM) is proposed to remedy these shortcomings. The collision step is modeled by the cumulant method, stable at low viscosities, and the streaming step is discretized first in time based on the Lax-Wendroff scheme, then in space according to the meshless local Petrov-Galerkin method, a mesh-free method (MLPG). To substantiate the accuracy of this method in aeroacoustics, the temporal decay of a standing plane wave, the spatial decay of a planar acoustic pulse, and the propagation of circular waves are considered, and the results are compared with numerical and analytical solutions. The comparisons show that MLPGC-LBM presents better results than standard LB methods, replicating the local radial point interpolation cumulant lattice Boltzmann method (LRPIC-LBM) results with relatively shorter runtimes, and being in a good agreement with the analytical solutions. The errors of the acoustic dispersion and dissipation are irrelevant, even for quite low resolutions. Therefore, MLPGC-LBM can offer an alternative to conventional aeroacoustics simulations alongside LRPIC-LBM with shorter runtimes, without parametric dependency on the number of points per wavelength and the resolution.

## 4.1 Introduction

The lattice Boltzmann method (LBM) is restricted by the lattice uniformity resulting from the symmetries of the lattice velocity model assumed. To overcome this restriction, conventional non-uniform LB methods have been proposed, categorized in different types: interpolation-supplemented LBM (44, 45), combinations of LBM with finite difference methods (46), finite volume methods (47–49), finite element methods (50–52), and Taylor-series expansion and least-squares-based lattice Boltzmann methods (53, 54). These methods have succeeded in simulating different problems, however, they suffer from drawbacks such as mesh generating costs, low accuracy of the computed stress in fluid-structure interaction simulations (119), and a disability to model singular physical phenomena. Thus, Mesh-Free methods are devised to deal with such obstacles (151, 152) by using a set of nodes called field nodes, scattered inside and on the boundaries of the domain. These methods generate a system of algebraic equations for the field nodes, without the need to explicitly link them in order to interpolate or approximate the unknown variables.

MFree methods have been developed along with old methods like the collocation method (160, 161), vortex method (57), finite difference method (162–164), and smoothed particle hydrodynamics (165, 166). Among the MFree methods classified according to their formulation procedure, the so called weak-form methods have attracted the interest of many researchers and are broadly expanded (151), such as the diffuse element method (63), the local radial point interpolation method (LRPIM) (154), the local point interpolation method (LPIM) (153), and the meshless local Petrov-Galerkin method (MLPG) (68). The idea of combining LBM and Mfree methods has led to acceptable results in some cases (71–73). These studies use the standard Bhatnagar-Gross-Krook (BGK) approach which is not stable at high Reynolds numbers and low viscosities (6, 74). Thus, combining the more stable cumulant LBM (5, 75) with Mfree-LB methods could provide better results in different engineering problems. This is the case when using the local radial point interpolation cumulant lattice Boltzmann method (LRPIC-LBM) (76). It can predict analytical results without parameter dependencies such as the number of points per wavelength  $N_{ppw}$ , and the resolution  $\sigma$ . In addition, as it will be shown in the following, the efficiency of

Mfree-LB methods could be increased by substituting the local radial point interpolation method with meshless local Petrov-Galerkin method in the Mfree part, due to the fact that radial point interpolation method shape functions used in LRPIM need more computational resources than moving least squares (MLS) shape functions used in MLPG.

The main objective of this work is to study the ability of the meshless local Petrov-Galerkin cumulant LBM (MLPG-LBM) to simulate aeroacoustics problems and compute the errors and deviations from the experimental and standard LBM, and LRPIC-LBM results. Thus, the LB equation is split into the collision part, modeled through the cumulant method, and the streaming part which is discretized first in time using the Lax-Wendroff scheme, then in space utilizing MLPG.

## 4.2 Lattice Boltzmann method

The lattice Boltzmann method (LBM) has been a good substitute for solving the Navier–Stokes equations to model different fluid flow phenomena. The LBM is divided into collision and streaming steps. The cumulant method as introduced in section 3.2.1 is used for the collision part, while the meshless local Petrov-Galerkin method (MLPG) instead of the local radial point interpolation method (RPIM) for the streaming part is adopted to introduce the meshless local Petrov-Galerkin cumulant lattice Boltzmann method (MLPG-CLBM) as follows.

### 4.2.1 Collision Step

The cumulant LBM was proposed by Seeger to solve the Boltzmann equation (12, 13). We refer to section 2.2.1 for the explanation of the cumulant LBM.

### 4.2.2 Streaming Step

The second key element of LBM is the streaming process, which is implemented by solving a pure advection equation (as presented in section 3.2.2)

$$\frac{\partial f_i}{\partial t} + c_{i,\alpha} \frac{\partial f_i}{\partial x_\alpha} = 0 \quad (4.1)$$

The Lax-Wendroff scheme and meshless local Petrov-Galerkin method (MLPG) are separately used for time and space discretization of Equation (4.1). Moreover, the unknown field function  $f_i$  can be estimated by trial (shape) functions as an approximate solution for the PDE. In this work, moving least-squares shape functions are chosen.

### Mfree shape function construction - Moving least squares shape functions

The moving least-squares (MLS) approximation developed by mathematicians in the field of data fitting (167) has been used for constructing MFree shape functions. It is classified as a method of series approximation of functions.

In the MLS approximation, the distribution function is approximated by  $f^h(\mathbf{x}, t)$  as

$$f(\mathbf{x}, t) \approx f^h(\mathbf{x}, t) = \sum_{i=1}^m p_i(\mathbf{x}) a_i(\mathbf{x}, t) = \mathbf{p}^T(\mathbf{x}) \mathbf{a}(\mathbf{x}, t) \quad (4.2)$$

where  $m$ ,  $p_i(\mathbf{x})$ , and  $a_i(\mathbf{x}, t)$  are the number of basis functions, the basis functions, and their corresponding coefficients, respectively. The coefficient  $\mathbf{a}$  is determined by minimizing the difference between the local approximation and the function according to the formula

$$J = \sum_{i=1}^n w_i(\mathbf{x}) \left[ \mathbf{p}^T(\mathbf{x}_i) \mathbf{a}(\mathbf{x}, t) - f_i(t) \right]^2, \quad (4.3)$$

where  $n$  is the number of nodes in the support domain of  $\mathbf{x}$  for the weight function  $w_i(\mathbf{x}) = w(\mathbf{x} - \mathbf{x}_i) \neq 0$  with a compact support associated with node  $\mathbf{x}_i$  and maximum at node  $\mathbf{x}_i$ . In addition,  $f_i(t) = f(\mathbf{x}_i, t)$  is the nodal value of the function  $f(\mathbf{x}, t)$ . It is called nodal parameter given that  $f_i(t) \neq f^h(\mathbf{x}_i, t)$  in the MLS approximation.

Minimizing the functional  $J$  leads to

$$\mathbf{A}(\mathbf{x}) \mathbf{a}(\mathbf{x}, t) = \mathbf{B}(\mathbf{x}) \mathbf{F}(t), \quad (4.4)$$

where

$$\mathbf{A}(\mathbf{x}) = \sum_{i=1}^n w_i \mathbf{p}(\mathbf{x}_i) \mathbf{p}^T(\mathbf{x}_i) = \begin{bmatrix} \sum_{i=1}^n w_i & \sum_{i=1}^n x_i w_i & \sum_{i=1}^n y_i w_i \\ \sum_{i=1}^n x_i w_i & \sum_{i=1}^n x_i^2 w_i & \sum_{i=1}^n x_i y_i w_i \\ \sum_{i=1}^n y_i w_i & \sum_{i=1}^n x_i y_i w_i & \sum_{i=1}^n y_i^2 w_i \end{bmatrix}, \quad (4.5)$$

$$\begin{aligned} \mathbf{B}(\mathbf{x}) &= [w_1(\mathbf{x}) \mathbf{p}(\mathbf{x}_1), w_2 \mathbf{p}(\mathbf{x}_2), \dots, w_n \mathbf{p}(\mathbf{x}_n)] \\ &= \begin{bmatrix} w_1 & w_2 & \dots & w_n \\ x_1 w_1 & x_2 w_2 & \dots & x_n w_n \\ y_1 w_1 & y_2 w_2 & \dots & y_n w_n \end{bmatrix}, \end{aligned} \quad (4.6)$$

$$\mathbf{F}(t) = [f_1(t), f_2(t), \dots, f_n(t)]^T. \quad (4.7)$$

Estimating  $\mathbf{a}(\mathbf{x}, t)$  from equation (4.4), and substituting it into equation (4.2), results in the following final form

$$f^h(\mathbf{x}, t) = \sum_{i=1}^n \phi_i(\mathbf{x}) f_i(t) = \mathbf{\Phi}(\mathbf{x}) \mathbf{F}(t), \quad (4.8)$$

where

$$\mathbf{\Phi}^T(\mathbf{x}) = \mathbf{p}^T(\mathbf{x}) \mathbf{A}^{-1}(\mathbf{x}) \mathbf{B}(\mathbf{x}), \quad (4.9)$$

and the shape function  $\phi_i$  for the  $i$ -th node is  $\phi_i(\mathbf{x}) = \mathbf{p}^T(\mathbf{x}) (\mathbf{A}^{-1} \mathbf{B})_i$ .

Unlike the finite-element approximation, the continuity of the MLS approximation depends not only on the basis functions, but also on the weight functions. Having  $C^l$  and  $C^k$  as the continuity classes for the basis functions and the weight functions respectively, results in  $C^{\min(l,k)}$  for the continuity of the MLS shape function. Since the base functions are infinitely differentiable monomial functions, the properties of the weight functions become thus determinant. Among the different types of weight functions employed in meshless methods, the cubic spline function is used in this work

$$V_i(r) = \begin{cases} \frac{2}{3} - 4r^2 + 4r^3 & r \leq 0.5 \\ \frac{4}{3} - 4r + 4r^2 - \frac{4}{3}r^3 & 0.5 < r \leq 1 \\ 0 & r > 1 \end{cases} \quad (4.10)$$

where  $r = |x - x_i| / d^{\max}$  and  $d^{\max}$  is the radius of the compact support.

### Semi-discrete formulation - Time discretization

Using the Taylor series expansion of the particle distributions and substituting the time derivatives with the spacial derivatives up to second order, the time discretization of equation (4.1) according to the Lax-Wendroff scheme is obtained as

$$f_i^{n+1} = f_i^n - \Delta t c_{i,\alpha} \frac{\partial f_i^n}{\partial x_\alpha} + \frac{\Delta t^2}{2} c_{i,\alpha} c_{i,\beta} \frac{\partial^2 f_i^n}{\partial x_\alpha \partial x_\beta}. \quad (4.11)$$

where here  $n$  refers to the time step.

### Semi-discrete formulation - Space discretization

The meshless local Petrov-Galerkin (MLPG) method, a local weak-form, is proposed to avoid global background cells for either function approximation or integration. The numerical integrations are executed over a local quadrature domain consisting of a set of distributed nodes. It should be mentioned that the MLS approximation is utilized to construct the shape functions in MLPG, which results in improving the efficiency of the scheme beyond that of the LRPM.

Generally, the weak form of the problem generated from the method of weighted residuals is used for MFree local weak-form methods. Thus, the weighted residual form of equation (4.11) on the local domain  $\Omega_I$  of point  $I$  bounded by  $\Gamma_I$  is

$$\begin{aligned} \int_{\Omega_I} V_I f_i^{n+1} d\Omega &= \int_{\Omega_I} V_I f_i^n d\Omega - \Delta t \int_{\Omega_I} V_I c_{i,\alpha} \frac{\partial f_i^n}{\partial x_\alpha} d\Omega \\ &+ \frac{\Delta t^2}{2} \int_{\Omega_I} V_I c_{i,\alpha} c_{i,\beta} \frac{\partial^2 f_i^n}{\partial x_\alpha \partial x_\beta} d\Omega \end{aligned} \quad (4.12)$$

where  $V_I$  is the local weight function of node  $I$  introduced in equation (4.10). Equation (4.12) is employed for all nodes in the domain.

Using integration by parts in equation (4.12), a continuous approximate solution is obtained and the differentiation requirements of the unknowns in the weighted residual form are reduced,

$$\begin{aligned} \int_{\Omega_I} V_I f_i^{n+1} d\Omega &= \int_{\Omega_I} V_I f_i^n d\Omega - \int_{\Omega_I} \left( \Delta t V_I c_{i,\alpha} \frac{\partial f_i^n}{\partial x_\alpha} + \frac{\Delta t^2}{2} c_{i,\alpha} c_{i,\beta} \frac{\partial V_I}{\partial x_\beta} \frac{\partial f_i^n}{\partial x_\alpha} \right) d\Omega \\ &+ \frac{\Delta t^2}{2} \int_{\Gamma_I} V_I c_{i,\alpha} c_{i,\beta} \frac{\partial f_i^n}{\partial x_\alpha} n_\beta d\Gamma \end{aligned} \quad (4.13)$$

where  $\Gamma_I$  and  $n_\beta$  are respectively the boundary of the local domain  $\Omega_I$  and the unit outward normal vector.

Substitution of the approximate solution (4.8) into equation (4.13) gives

$$\sum_{j=1}^{N_I} \mathbf{M}_{IJ} f_{i,j}^{n+1} = \sum_{j=1}^{N_I} [\mathbf{M}_{IJ} + \mathbf{K}_{i,IJ}] f_{i,j}^n \quad (4.14)$$

where  $\mathbf{M}_{IJ}$  is the nodal mass matrix and  $\mathbf{K}_{i,IJ}$  is the nodal stiffness matrix, written as

$$\mathbf{M}_{IJ} = \int_{\Omega_I} V_I \Phi_J d\Omega \quad (4.15)$$

$$\mathbf{K}_{i,IJ} = - \int_{\Omega_I} \left( \Delta t V_I + \frac{\Delta t^2}{2} c_{i,\beta} \frac{\partial V_I}{\partial x_\beta} \right) c_{i,\alpha} \frac{\partial \Phi_J}{\partial x_\alpha} d\Omega + \frac{\Delta t^2}{2} \int_{\Gamma_I} V_I c_{i,\alpha} \frac{\partial \Phi_J}{\partial x_\alpha} c_{i,\beta} n_\beta d\Gamma \quad (4.16)$$

Therefore, the global equation system for all nodes in the whole domain is expressed by

$$\mathbf{M} \mathbf{f}_i^{n+1} = [\mathbf{M} + \mathbf{K}_i] \mathbf{f}_i^n \quad (4.17)$$

where  $\mathbf{f}_i$ ,  $\mathbf{M}$ , and  $\mathbf{K}$  and are the particle distribution vector, the global mass matrix, and stiffness matrix, respectively. This system is worked out separately for each direction.

Using the Gauss quadrature scheme leads to the numerical area and curve integration of equations (4.15) and (4.16),



$$\mathbf{M}_{IJ} = \sum_{\kappa=1}^{n_g} \tilde{\zeta}_{\kappa} V_I(x_{\kappa}) \Phi_J(x_{\kappa}) \left| J^{\Omega_I} \right| \quad (4.18)$$

$$\begin{aligned} \mathbf{K}_{i,IJ} = & - \sum_{\kappa=1}^{n_g} \tilde{\zeta}_{\kappa} \left( \Delta t V_I(x_{\kappa}) + \frac{\Delta t^2}{2} c_{i,\beta} \frac{\partial V_I}{\partial x_{\beta}} \Big|_{x_{\kappa}} \right) c_{i,\alpha} \frac{\partial \Phi_J}{\partial x_{\alpha}} \Big|_{x_{\kappa}} \left| J^{\Omega_I} \right| \\ & + \frac{\Delta t^2}{2} \sum_{\kappa=1}^{n_g^b} \tilde{\zeta}_{\kappa} V_I(x_{\kappa}) c_{i,\alpha} \frac{\partial \Phi_J}{\partial x_{\alpha}} \Big|_{x_{\kappa}} c_{i,\beta} n_{\beta} \left| J^{\Gamma_I} \right| \end{aligned} \quad (4.19)$$

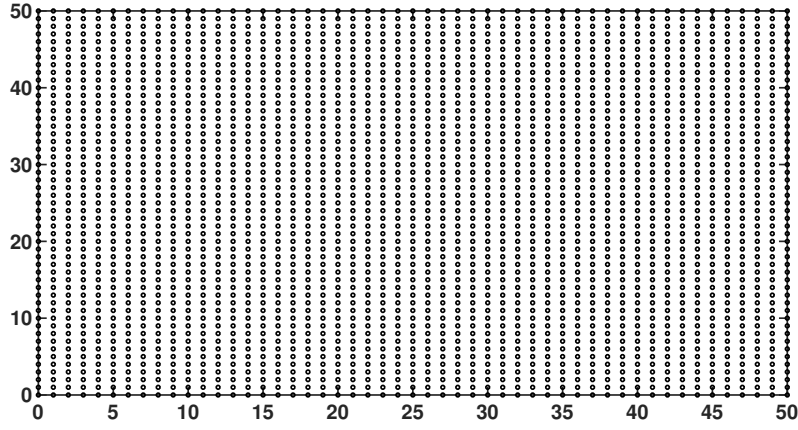
where  $n_g$ ,  $n_g^b$ ,  $\tilde{\zeta}_{\kappa}$ ,  $J^{\Omega_I}$ , and  $J^{\Gamma_I}$  are respectively the total number of Gauss points in the quadrature domain, the total number of Gauss points at the boundaries, the Gauss weight factor for Gauss point  $x_{\kappa}$ , the Jacobian matrix for the domain integrations, and the Jacobian matrix for boundary integrations.

### 4.3 Results and Discussion

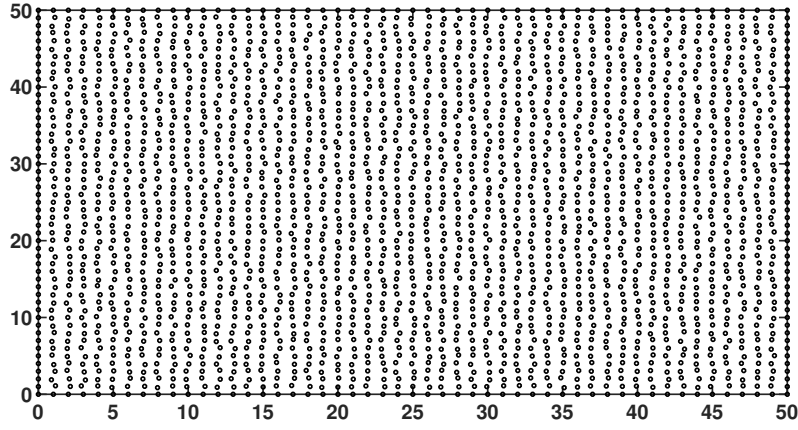
For direct simulations with reduction of computational costs, aeroacoustics has lately adopted the LBM. In this section, the standard analysis consisting of obtaining acoustic properties for benchmark cases is studied using the meshless local Petrov-Galerkin cumulant lattice Boltzmann method (MLPGC-LBM). Here, as in previous chapters, the propagation of planar acoustic waves is considered, focusing on numerical dissipation and dispersion. In addition, spherical wave propagations are studied. To have a better assessment of MLPGC-LBM, four setups based on (76, 145) are examined including the temporal decay of a standing plane wave in a periodic domain, the spatial decay of a propagating planar acoustic pulse of Gaussian shape, a 2D acoustic pulse with Gaussian shape, and acoustic point source for regular (default) and irregular nodal distributions (shown in Figures 4.1a and 4.1b). The base units are in the LB system.

#### 4.3.1 Planar standing wave

As a first configuration, a standing plane acoustic wave in a periodic domain is studied. The dissipation and dispersion relations according to a temporal analysis as



(A) Regular nodes.



(B) Irregular nodes.

FIGURE 4.1: Nodal arrangement for the propagation of planar acoustic waves in MLPGC-LBM simulations.

represented in subsection 2.3.1 are

$$c_T = c_s \sqrt{1 - \left(\frac{kv}{c_s}\right)^2}, \quad (4.20a)$$

$$\alpha_T = k^2 v \quad (4.20b)$$

where  $k$  is the wave-number. The assumptions for this set-up are given as a reference in Table 4.1 (76, 145) (Where " $\prime$ " is perturbation quantity). The results of such study can be expressed either as a function of the number of points per wavelength  $N_{ppw} = \lambda/\Delta x$ , or the non dimensional wave-number  $k\Delta x = 2\pi/N_{ppw}$ .

The acoustic pressure at time  $t$  is (76, 145)

TABLE 4.1: Parameters for the planar standing wave

Variables	$p'(x, y, 0)$	$\rho'$	$u'$	$v'$	$A$
Description	$A \sin\left(\frac{2\pi x}{\lambda}\right)$	$\frac{\rho'}{c_s^2}$	$\frac{\rho'}{\rho_0 c_s}$	0	$10^{-3} p_0$

$$p'(x, y, t) = A \exp[-\alpha_T t] \sin[k(x - c_T t)] \quad (4.21)$$

To study the pros and cons of the meshless local Petrov-Galerkin cumulant lattice Boltzmann method (MLPGC-LBM), the propagation of waves with various viscosities,  $\nu$ , and different resolutions (i.e. the number of points per wavelength) was investigated. The acoustic pressure time-history for  $\nu = 1.0 \times 10^{-2} \left[\frac{\Delta x^2}{\Delta t}\right]$  with  $N_{ppw} = 14$  points per wavelength is presented in figure 4.2. The analytical result is drawn with a solid black line while MLPGC-LBM with linear basis functions ( $m = 3$ ) and quadric basis functions ( $m = 6$ ) are shown with a blue five-pointed star and a red asterisk, respectively. It is shown that this method with linear and quadric basis functions gives a good prediction of the analytical acoustic pressure values.

Figure 4.3 shows the acoustic pressure time history for  $\nu = 1.0 \times 10^{-4} \left[\frac{\Delta x^2}{\Delta t}\right]$  with  $N_{ppw} = 14$  points per wavelength. It draws a comparison between the analytical solution and the meshless local Petrov-Galerkin cumulant lattice Boltzmann method results with linear basis functions ( $m = 3$ ) at low viscosities. One major drawback of standard LB methods is the instability that develops at low viscosities, however, this method even with linear basis functions, shows a good performance and closely predicts the theoretical solution with negligible phase speed and temporal dissipation rate errors.

The numerical deviations of the acoustical properties for current standard LB methods are functions of  $N_{ppw}$  and are independent of other parameters such as the frequency and the viscosity. For example, the errors of the BGK (30) and the cumulant LBM (145) are about 7 percent for  $N_{ppw} = 4$  for such properties. However, the advent of combined Mfree-LB methods such as the local radial point interpolation cumulant lattice Boltzmann method (LRPIC-LBM), makes it possible to predict wave motion with no dependency on the number of points per wavelength  $N_{ppw}$ . Figure 4.4 shows the acoustic pressure time history for  $\nu = 1.0 \times 10^{-2} \left[\frac{\Delta x^2}{\Delta t}\right]$  with

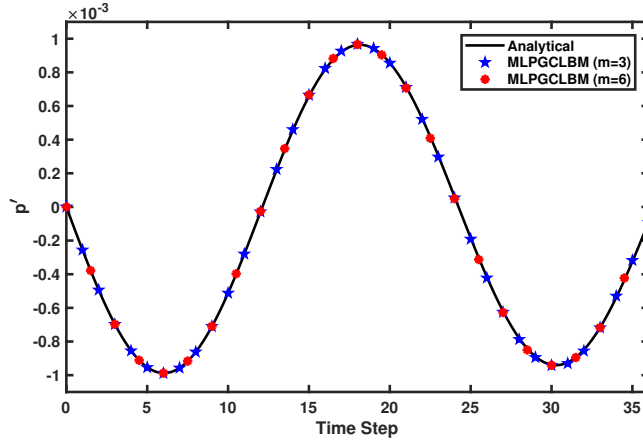


FIGURE 4.2: Acoustic pressure  $[\frac{kg}{\Delta x \Delta t^2}]$  versus time step  $[\Delta t]$  for  $\nu = 1.0 \times 10^{-2} [\frac{\Delta x^2}{\Delta t}]$  with  $N_{ppw} = 14$  points per wavelength.

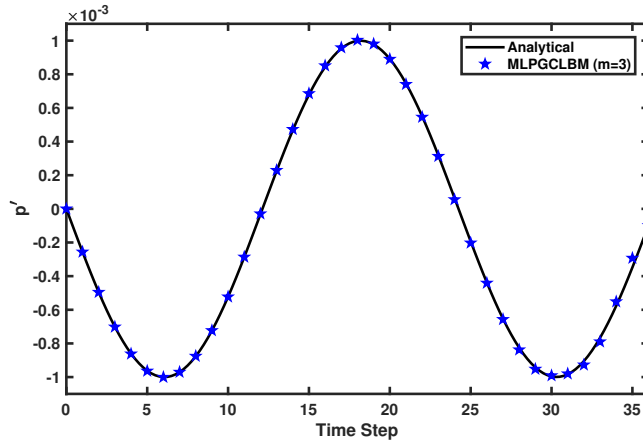


FIGURE 4.3: Acoustic pressure  $[\frac{kg}{\Delta x \Delta t^2}]$  versus time step  $[\Delta t]$  for  $\nu = 1.0 \times 10^{-4} [\frac{\Delta x^2}{\Delta t}]$  with  $N_{ppw} = 14$  points per wavelength.

$N_{ppw} = 4$  points per wavelength for the analytical solution (a solid black line), the cumulant LBM (a dash red line) and the meshless local Petrov-Galerkin cumulant lattice Boltzmann method (MLPGC-LBM) with linear basis functions (magenta asterisk), with  $\Delta t = 0.1$ . It shows that MLPGC-LBM with linear basis functions is more successful in predicting theoretical results than the cumulant LBM, with a reduced number of points per wavelength.

In general, one of the characteristics of MLPGM is that the Kronecker delta condition is not satisfied, so the accuracy of the results obtained in the nodes is reduced. Among the ways presented in reference (151) to improve accuracy, we are interested in increasing the polynomial degree of the basis functions. Thus, by replacing the linear basis functions with quadric ones in meshless local Petrov-Galerkin cumulant

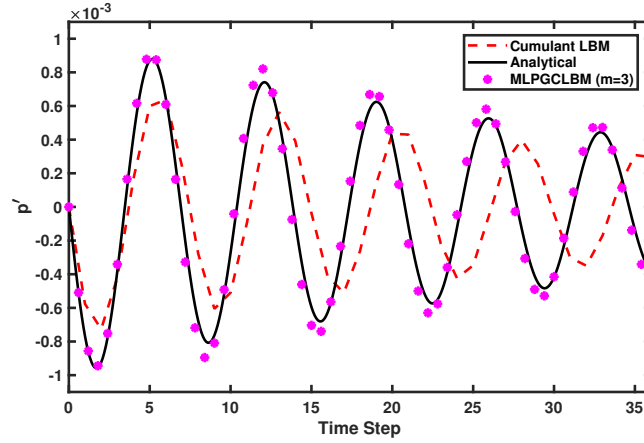


FIGURE 4.4: Acoustic pressure  $[\frac{kg}{\Delta x \Delta t^2}]$  versus time step  $[\Delta t]$  for  $\nu = 1.0 \times 10^{-2} [\frac{\Delta x^2}{\Delta t}]$  with  $N_{ppw} = 4$  points per wavelength and  $\Delta t = 0.1$ .

lattice Boltzmann method (MLPGC-LBM), an improvement is achieved as we will show. Figure 4.5 shows the acoustic pressure time history for  $\nu = 1.0 \times 10^{-2} [\frac{\Delta x^2}{\Delta t}]$  with  $N_{ppw} = 4$  points per wavelength for the analytical solution (black solid line), the local radial point interpolation cumulant lattice Boltzmann method (LRPIC-LBM) (blue five-point star) and the meshless local Petrov-Galerkin cumulant lattice Boltzmann method (MLPGC-LBM) solution with quadric basis functions ( $m = 6$ ) (magenta asterisk), for  $\Delta t = 0.1$ . This figure shows that both MLPGC-LBM and LRPIC-LBM replicate the analytical results. On the other hand, one of the pros of MLPGM is that its efficiency is higher than that of LRPIM due to the difference in the interpolation procedures (the moving least squares (MLS) shape functions). Therefore, MLPGC-LBM benefits from this feature. Moreover, for the acoustic pressure time history shown in figure 4.5, the average run time for the MLPGC-LBM is 0.285 times that of the LRPIC-LBM. Both methods give similar results, predicting wave motion accurately with no dependency on the number of points per wavelength  $N_{ppw}$ , but MLPGC-LBM needs lesser run times.

In many engineering problems such as those of acoustics, it is necessary to use irregular nodes. We have seen how MLPGC-LBM performs efficiently when it comes to predict the propagation of acoustic waves through domains with regular nodal distributions. However, the accuracy of this method should also be examined with irregular nodes (Figure 4.1b). Figure 4.6 presents the acoustic pressure time history

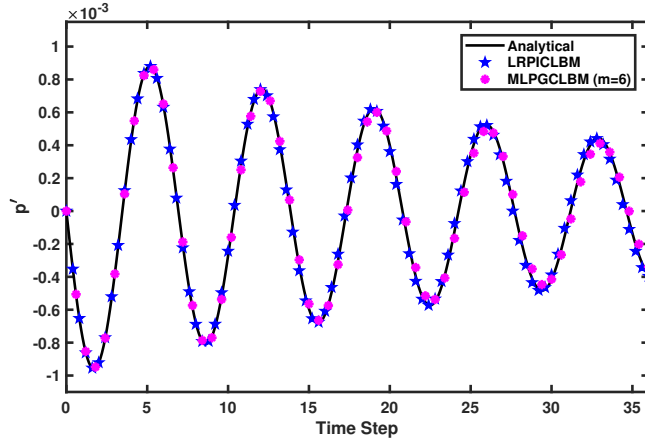


FIGURE 4.5: Acoustic pressure  $[\frac{kg}{\Delta x \Delta t^2}]$  versus time step  $[\Delta t]$  for  $\nu = 1.0 \times 10^{-2} [\frac{\Delta x^2}{\Delta t}]$  with  $N_{ppw} = 4$  points per wavelength with  $\Delta t = 0.1$ .

for  $\nu = 1.0 \times 10^{-2} [\frac{\Delta x^2}{\Delta t}]$  with  $N_{ppw} = 14$  points per wavelength. It shows the comparison between analytical (solid black line) and MLPGC-LBM results determined with linear basis functions ( $m = 3$ ) (blue five-pointed star) and quadric basis functions ( $m = 6$ ) (red asterisk). It is shown that MLPGC-LBM with linear basis functions cannot reliably predict the motion of waves and results soon depart from the theoretical solution. This issue is related to the lack of a delta function in parts of the MLPGC-LBM solver. We observe instead how the results of MLPGC-LBM with quadric basis functions dramatically improve and very closely reproduce the analytical acoustic pressure.

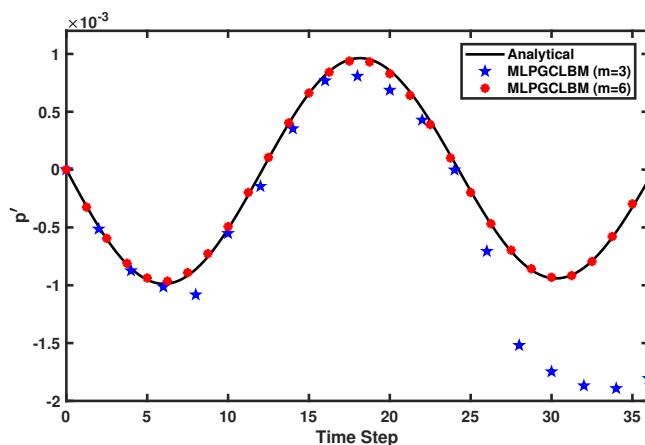


FIGURE 4.6: Acoustic pressure  $[\frac{kg}{\Delta x \Delta t^2}]$  versus time step  $[\Delta t]$  for  $\nu = 1.0 \times 10^{-2} [\frac{\Delta x^2}{\Delta t}]$  with  $N_{ppw} = 14$  points per wavelength with irregular nodal distributions.

### 4.3.2 Planar pulse wave

As a second case, the study of a planar pulse wave is carried out by choosing a planar pulse of Gaussian shape located at the center of the domain. The dissipation and dispersion relations generated from the spatial analysis as represented in subsection 2.3.1 are

$$c_S = \sqrt{2}\zeta_s \sqrt{\frac{1 + (\omega\tau_s)^2}{\sqrt{1 + (\omega\tau_s)^2} + 1}}, \quad (4.22a)$$

$$\alpha_S = \frac{\omega}{\sqrt{2}\zeta_s} \sqrt{\frac{\sqrt{1 + (\omega\tau_s)^2} - 1}{1 + (\omega\tau_s)^2}}. \quad (4.22b)$$

The planar pulse propagates throughout the domain. The assumptions are shown in Table 4.2. It should be noted that periodic boundary conditions are imposed.

TABLE 4.2: Parameters for the planar pulse wave

Variables	$p'(x, y, 0)$	$\rho'$	$u'$	$v'$	A	$\sigma$
Description	$A \exp\left(-\ln(2) \frac{x^2}{\sigma^2}\right)$	$\frac{\rho'}{c_s^2}$	$\frac{\rho'}{\rho_0 c_s}$	0	$10^{-3} p_0$	0.06 – 0.11

To study the behavior of meshless local Petrov-Galerkin cumulant lattice Boltzmann method (MLPGC-LBM) in a pulse wave emission, we followed references (76, 145). Thus, different viscosities and resolutions  $\sigma$  are considered. The acoustic pressure time-history for  $\nu = 1.0 \times 10^{-2} [\frac{\Delta x^2}{\Delta t}]$  with  $\sigma = 0.11$  is presented in figure 4.7. It shows the comparison between the cumulant LBM (dashed red line) and the MLPGC-LBM results with linear basis functions ( $m = 3$ ) (blue pentagram) and quadric basis functions ( $m = 6$ ) (solid black line). Data are taken at 0, 5, 11, and 17 nodes apart from the center of the domain showing that the intensity loss at any location is proportional to the propagation distance (30, 76, 145). It should be noted that the deviations between the cumulant LBM and MLPGC-LBM with linear or quadric basis functions are minor.

In general, the resolution  $\sigma$  is a parameter which can have an effective impact on the accuracy of LBM results. Figure 4.8 shows the acoustic pressure time history for  $\nu = 1.0 \times 10^{-2} [\frac{\Delta x^2}{\Delta t}]$ , with  $\sigma = 0.06$ . It shows that by reducing  $\sigma$ , the number of

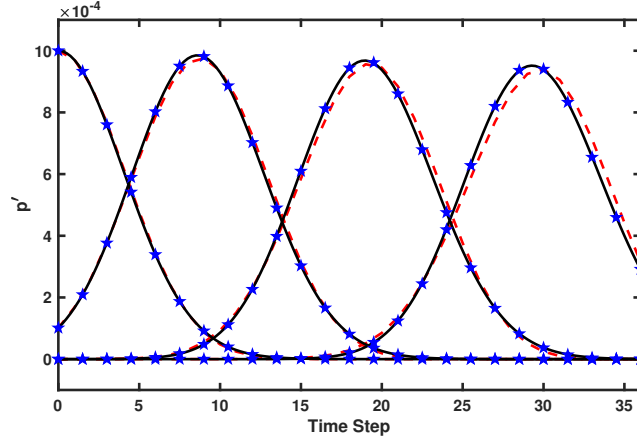


FIGURE 4.7: Acoustic pressure  $[\frac{kg}{\Delta x \Delta t^2}]$  versus time step  $[\Delta t]$  for  $\nu = 1.0 \times 10^{-2} [\frac{\Delta x^2}{\Delta t}]$  with  $\sigma = 0.11$ : cumulant LBM (dashed red line), MLPGC-LBM ( $m=6$ ) (solid black line), and MLPGC-LBM ( $m=3$ ) (blue pentagram).

nodes inside the pulse reduces, which produces wiggling in the cumulant LBM results (dashed red line). On the other hand, combinations of LBM and Mfree methods such as local radial point interpolation cumulant lattice Boltzmann method (LRPIC-LBM) (solid black line) and meshless local Petrov-Galerkin cumulant lattice Boltzmann method (MLPGC-LBM) with linear basis functions (blue pentagram) behave smoothly. These two Mfree-LB methods give the same results for this setup, but the average run time for MLPGC-LBM is 0.289 times the LRPIC-LBM run time per iteration. The comparison of the ratio  $\hat{p}'(x, \omega) / \hat{p}'(x, 0)$ , as a function of the angular frequency, between LRPIC-LBM and analytical solutions (76) shows that LRPIC-LBM with  $\sigma = 0.06$  successfully predicts theoretical results. And since MLPGC-LBM data closely follow those of LRPIC-LBM, therefore, this method can successfully simulate wave propagation even at low resolutions.

The acoustic pressure time history for  $\nu = 1.0 \times 10^{-2} [\frac{\Delta x^2}{\Delta t}]$  with  $\sigma = 0.11$  for irregular nodes (Figure 4.1b) is depicted in figure 4.9. Cumulant LBM and meshless local Petrov-Galerkin cumulant lattice Boltzmann method (MLPGC-LBM) results with linear basis functions ( $m = 3$ ) and quadric basis functions ( $m = 6$ ) are represented by a dashed red line, blue pentagram with blue line, and a solid black line, respectively. Figure 4.9 shows that this method with linear basis functions cannot predict wave propagation, which traces back to the lack of a delta function property in the MLPGM scheme. Therefore, as in the temporal analysis of section 4.3.1, the solution



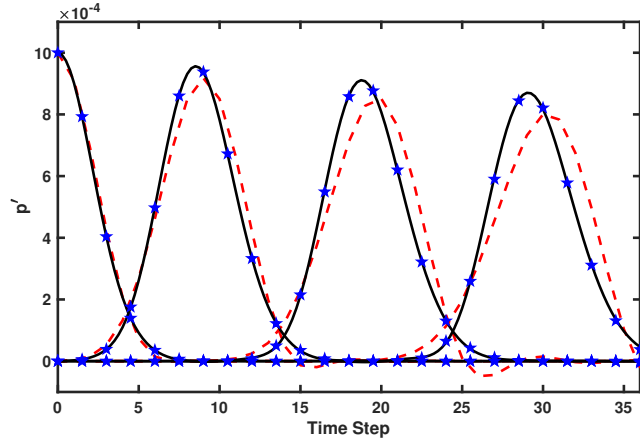


FIGURE 4.8: Acoustic pressure  $[\frac{kg}{\Delta x \Delta t^2}]$  versus time step  $[\Delta t]$  for  $\nu = 1.0 \times 10^{-2} [\frac{\Delta x^2}{\Delta t}]$  with  $\sigma = 0.06$ : cumulant LBM (dashed red line), LRPIC-LBM (solid black line), and MLPGC-LBM (m=3) (blue pentagram).

shows instabilities. On the other hand, by using quadric basis functions, one can obtain the same results as with a regular nodal distribution.

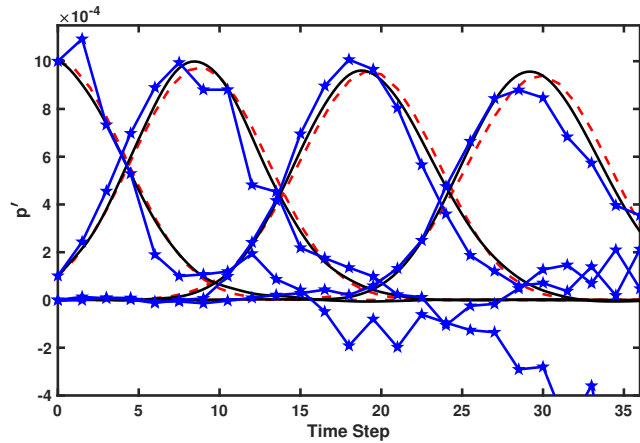


FIGURE 4.9: Acoustic pressure  $[\frac{kg}{\Delta x \Delta t^2}]$  versus time step  $[\Delta t]$  for  $\nu = 1.0 \times 10^{-2} [\frac{\Delta x^2}{\Delta t}]$  with  $\sigma = 0.11$ : cumulant LBM (dashed red line), MLPGC-LBM (m=6) (solid black line), and MLPGC-LBM (m=3) (blue pentagram with blue line).

### 4.3.3 Acoustic pulse

A 2D acoustic pulse is studied as the most standard aeroacoustic 2D benchmark case (127). This is categorized as a type of spherical wave propagation, with a pulse which is considered as Gaussian in shape. The assumptions of the setup are written in Table 4.3. Even though periodic boundary conditions are chosen, the total simulation time

is limited so as to prevent any boundary effects. In this study, an acoustic pulse generated by an initial Gaussian pressure distribution expands from the center of the domain.

TABLE 4.3: Parameters for the 2D acoustic pulse

Variables	$\rho'$	$u'$	$v'$	$\epsilon$	$\alpha$	$\sigma$	$r$
Description	$\epsilon \exp(-\alpha r^2)$	0	0	$10^{-3}$	$\frac{\ln(2)}{\sigma^2}$	0.11 - 0.04	$\sqrt{x^2 + y^2}$

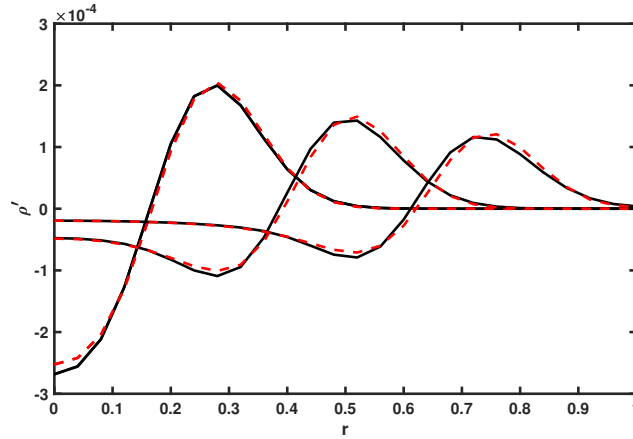


FIGURE 4.10: Propagation of the density perturbation through the domain for  $\nu = 1.0 \times 10^{-2} [\frac{\Delta x^2}{\Delta t}]$  with  $\sigma = 0.11$ : cumulant LBM (solid black line), MLPGC-LBM ( $m=6$ ) (dashed red line).

Figure 4.10 draws a comparison between the solutions of the cumulant LBM (solid black line) and the meshless local Petrov-Galerkin cumulant LBM with quadric basis functions ( $m = 6$ ) (dashed red line). The plot represents the density perturbation obtained with the parameters  $\nu = 1.0 \times 10^{-2} [\frac{\Delta x^2}{\Delta t}]$  and  $\sigma = 0.11$  as a function of the radial distance. There is a good agreement between both methods when  $\sigma$  is equal to 0.11 or greater, and the deviations are small.

In the study of the propagation of the spherical acoustic pulse, the parameter  $\sigma$  can also affect the accuracy of the LBM results. This is shown in Figure 4.11, which represents the density function of the acoustic pulse propagation for  $\nu = 1.0 \times 10^{-2} [\frac{\Delta x^2}{\Delta t}]$  with  $\sigma = 0.04$ . Here, the same behavior as in planar acoustic waves is found: by reducing  $\sigma$ , the number of nodes inside the pulse is also reduced, which causes the wiggling seen in the cumulant LBM density wave. Figure 4.10 shows that the cumulant LBM is less stable at low resolutions.

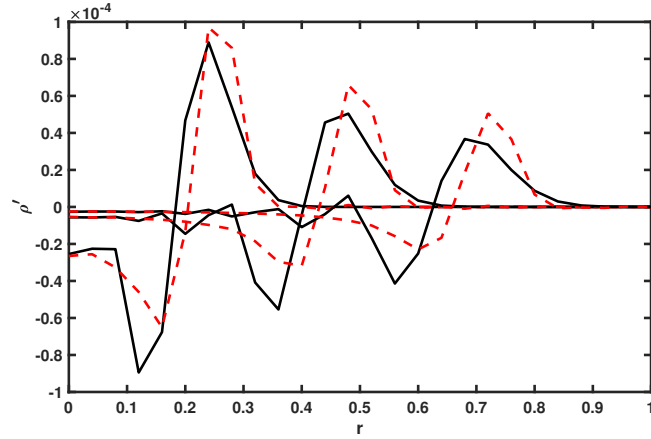


FIGURE 4.11: Propagation of the density perturbation through the domain for  $\nu = 1.0 \times 10^{-2} [\frac{\Delta x^2}{\Delta t}]$  with  $\sigma = 0.04$ : cumulant LBM (solid black line), MLPGC-LBM ( $m=6$ ) (dashed red line).

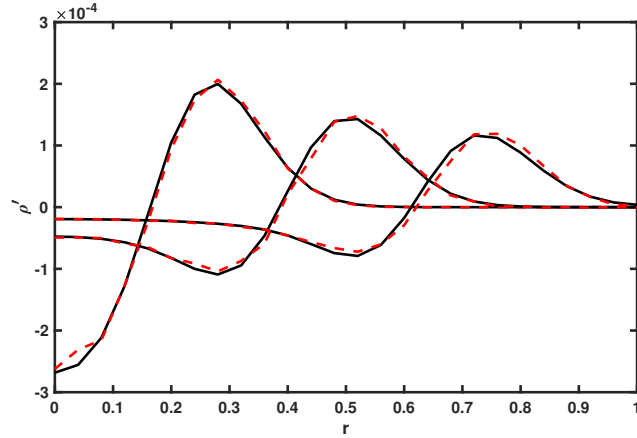


FIGURE 4.12: Propagation of the density perturbation through the irregular nodal distribution for  $\nu = 1.0 \times 10^{-2} [\frac{\Delta x^2}{\Delta t}]$  with  $\sigma = 0.04$ : cumulant LBM (solid black line), MLPGC-LBM ( $m=6$ ) (dashed red line).

The propagation of the spherical acoustic pulse for  $\nu = 1.0 \times 10^{-2} [\frac{\Delta x^2}{\Delta t}]$  with  $\sigma = 0.11$  for an irregular nodal distribution (Figure 4.1b) is illustrated in Figure 4.12. The results of the meshless local Petrov-Galerkin cumulant LBM with quadric basis functions ( $m = 6$ ) and the cumulant LBM are represented by a dashed red line and a solid black line, respectively. Figure 4.12 shows that this method, using quadric basis functions, can predict the same results as with regular nodes.

### 4.3.4 Acoustic point source

In this section, to further demonstrate the abilities of the meshless local Petrov-Galerkin cumulant LBM in simulating 2D problems, another test case will be studied: the infinite waves generated by a point source which transmits a sinusoidal signal. The assumptions for this set-up are listed in table 4.4. To model this point source, a sinusoidal density function is set up at the center node of the domain as in references (145) and periodic boundary conditions are used.

TABLE 4.4: Parameters for the acoustic point source

Variables	$\rho'$	$\omega$	$B$	$r$	$T$
Description	$B \sin(\omega t)$	$\frac{2\pi}{T}$	$10^{-2}$	$\sqrt{x^2 + y^2}$	$10 - 20$

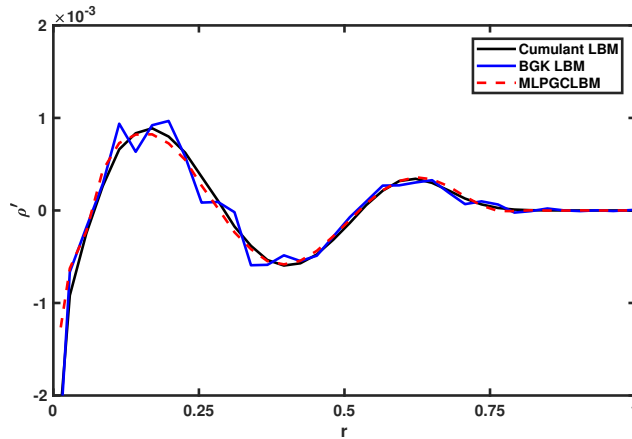


FIGURE 4.13: Comparison of the values of the density perturbation with a period  $T = 20 [\Delta t]$ .

The propagation of the density function of the acoustic point source wave for  $\nu = 1.0 \times 10^{-2} [\frac{\Delta x^2}{\Delta t}]$  with a period  $T = 20[\Delta t]$  is shown in Figure 4.13. The meshless local Petrov-Galerkin cumulant (MLPGC-LBM) result is drawn with a dashed red line while the standard cumulant and standard BGK LBM results are shown with a solid black line and a solid blue line, respectively. MLPGC-LBM shows a good agreement with the cumulant LBM at a relatively suitable period  $T = 20[\Delta t]$ . The BGK LBM result follows the other curves, but it displays noisy behavior, as the method is here unstable.

The period  $T$ , like  $\sigma$ , is a parameter which can have effects on the accuracy of LBM results. Figure 4.14 presents the propagation of the density function of the

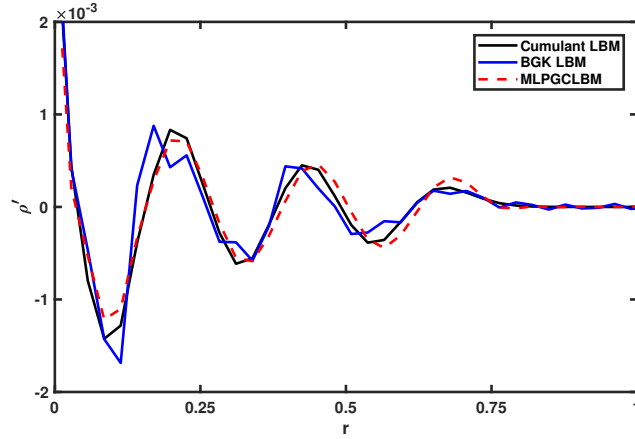


FIGURE 4.14: Comparison of the values of the density perturbation with a period  $T = 10 [\Delta t]$ .

acoustic point source wave for  $\nu = 1.0 \times 10^{-2} [\frac{\Delta x^2}{\Delta t}]$ , with periods  $T = 10$ . It illustrates that by reducing the period, the number of nodes inside the waves is reduced, which yield worse results for the BGK LBM (solid blue line) than the previous simulation. In fact, the deviation between the cumulant (solid black line) and the meshless local Petrov-Galerkin cumulant LBM (dashed red line) increases for  $T = 10$ .

A similar analysis can be conducted on the same problem using an irregular nodal distribution for the methods under consideration, with analogous results. As an example, the propagation of the density function of the acoustic point source wave for  $\nu = 1.0 \times 10^{-2} [\frac{\Delta x^2}{\Delta t}]$  with period  $T = 20[\Delta t]$  for an irregular nodal distribution is depicted in Figure 4.15. It shows small deviations between the meshless local Petrov-Galerkin cumulant (MLPGC-LBM) (dashed red line) and the cumulant LBM (solid black line).

## 4.4 Conclusions

In this work, propagation of point and planar acoustic waves comprising the temporal decay of a standing plane wave, the spatial decay of a planar acoustic pulse, and the propagation of spherical waves, in most real cases, are modeled by the meshless local Petrov-Galerkin cumulant lattice Boltzmann method (MLPGC-LBM). In this model the collision step is modeled by the cumulant method and the streaming step is discretized first in time based on the Lax-Wendroff scheme, then in space according to the meshless local Petrov-Galerkin method, a mesh-free method (MLPG). The

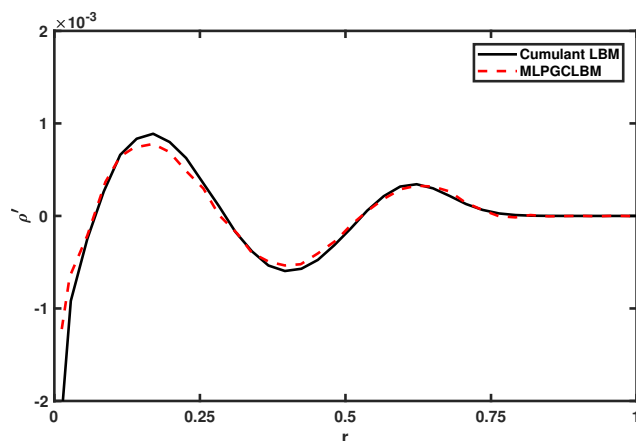


FIGURE 4.15: Comparison of the values of the density perturbation with a period  $T = 20 [\Delta t]$  propagating through an irregular nodal distribution.

comparison drawn between the results of MLPGC-LBM and LRPIC-LBM, cumulant LBM, and the analytical solution, illustrates that the acoustic pressure time-history for LB methods has a similar behavior and the errors of the phase speed and the dissipation rate at high enough  $N_{ppw}$  and  $\sigma$  are negligible. Moreover, the decrease of the viscosity does not undermine the stability of these two LB methods due to the advantages of the cumulant method. However, the meshless local Petrov-Galerkin cumulant lattice Boltzmann method predicts the same acoustic pressure time-history as the local radial point interpolation cumulant lattice Boltzmann method but with shorter run times, and the error of both the phase speed and the dissipation rate for low  $N_{ppw}$  and  $\sigma$  are negligible thanks to the properties of the Mfree method. Furthermore, using MLPGC-LBM with irregular nodal distributions and linear basis functions to simulate the propagation of acoustic waves does not give correct results, thus quadric basis functions are needed due to inaccuracies generated by the lack of delta function properties in the MLPGM scheme. Moreover, simulating spherical propagations (acoustic 2D pulse and acoustic point source) show that when the number of point per wavelength is high, the deviations between the MLPGC-LBM and cumulant LBM are low and vice versa, reproducing the same results as planar acoustic waves. To conclude, the possibility of scattering the computational nodes through the domain depending on problem conditions (such as geometries), the accuracy achieved by MLPG, and the high stability provided by the cumulant LBM, make MLPG-LBM a good alternative to conventional methods to model complex

engineering problems, especially in aeroacoustics.

## Chapter 5

# Conclusions

In this thesis we studied one of the newest LB methods, “the cumulant lattice Boltzmann method” and developed new MFree local weak-form cumulant LB methods which can aid in the modeling of challenging engineering problems. To begin with, the cumulant lattice Boltzmann method was used to improve the standard numerical treatment of sound wave propagation as one of the demanding topics of nowadays modeling. Thus, different types of sound wave propagation, their dissipation and dispersion rates were considered. Moreover, due to the fact that in the most common phenomena, fluid and solid phases coexist and interact, and the coupling of fluid and solid solvers is always challenging, the cumulant LBM was coupled with the finite element method and its behavior was investigated. The problem selected for this purpose was a fluid-structure interaction problem: the wake post a cylinder with flexible flaps attached. This challenging example served to show the stability of the cumulant LBM and study the effects of splitter plates which look like hair on the flow and sound pattern of cylinder wakes. The major conclusions are the following, the cumulant LBM based on the temporal and spatial analyses of the acoustic properties replicated the dissipation and dispersion rates of the theoretical solutions for the standing plane wave and the Gaussian planar pulse. The phase speed and dissipation errors are a function of the number of points per wavelength. In addition, the cumulant LBM reproduces the propagation of a spherical acoustic pulse and the infinite spherical wave generated from a point source, while the BGK LBM did not succeed due to a numerical instability at low viscosities. Besides this, the coupled cumulant LBM-FEM simulations show that the mobility of flaps the phase within the vortex shedding cycle, resulted in the reduction of the transversal dislocation of



the shed vorticity, causing the vortices being shed in a row along the center-line of the flow over a single cylinder.

Even though the cumulant method showed remarkable results for above simulations with low viscosities and high Re numbers, it was important to find new methods and substitute the cumulant LBM to overcome the issues of dependency to the number of points per wavelength. Therefore, the propagation of acoustic waves, including the temporal decay of a standing plane wave and the spatial decay of a planar acoustic pulse were chosen as case studies. As a first method, the local radial point interpolation cumulant lattice Boltzmann method (LRPIC-LBM) was proposed and used to study of the propagation of acoustic waves in the aforementioned cases. This method uses the cumulant method in the collision step, and the Lax-Wendroff scheme and the local radial point interpolation method (RPIM) for the time and space discretization in the streaming step. The results showed minor deviations for the phase speed and the dissipation rate for high number of points per wavelength  $N_{ppw}$  and resolution  $\sigma$ , similarly to the cumulant LBM. However, unlike the cumulant LBM, the time history for the acoustic pressure obtained by LRPIC-LBM showed considerably smaller errors for low  $N_{ppw}$  and  $\sigma$  due to use of the meshless method. In addition, using irregular nodal distributions instead of regular nodal distributions did not affect the results of the propagation of acoustic waves. As a second method, the meshless local Petrov-Galerkin cumulant lattice Boltzmann method (MLPGC-LBM) was introduced, where the meshless local Petrov-Galerkin method (MLPG) is used instead of the local radial point interpolation method (RPIM). The acoustic pressure time-history for this method has a similar behavior to the previous methods at high enough  $N_{ppw}$  and  $\sigma$ . MLPGC-LBM predicts the same acoustic pressure time-history as LRPIC-LBM, but with shorter run times, for low  $N_{ppw}$  and  $\sigma$ . However, MLPGC-LBM with irregular nodal distributions and linear basis functions did not correctly model the propagation of acoustic waves due to inaccuracy made by the lack of delta function properties in the MLPGM scheme, which cause the use of the quadric basis functions. To conclude, the freedom to scatter nodes according to the problem conditions inside the domain and boundaries, the accuracy achieved by RPIM and MLPG, and the high stability provided by the cumulant

LBM, make MFree local weak-form cumulant LB methods good alternatives to conventional methods to model engineering simulations.



## References

- (1) Fard, E. G. A Cumulant LBM approach for Large Eddy Simulation of Dispersion Microsystems., Ph.D. Thesis, Univ.-Bibl., 2015.
- (2) Hardy, J, Pomeau, Y., and De Pazzis, O (1973). Time evolution of a two-dimensional model system. I. Invariant states and time correlation functions. *Journal of Mathematical Physics* 14, 1746–1759.
- (3) Frisch, U., Hasslacher, B., and Pomeau, Y. (1986). Lattice-gas automata for the Navier-Stokes equation. *Physical Review Letters* 56, 1505.
- (4) McNamara, G. R., and Zanetti, G. (1988). Use of the Boltzmann equation to simulate lattice-gas automata. *Physical Review Letters* 61, 2332.
- (5) Kian Far, E., Geier, M., Kutscher, K., and Konstantin, M. (2016). Simulation of micro aggregate breakage in turbulent flows by the cumulant lattice Boltzmann method. *Computers & Fluids* 140, 222 –231.
- (6) Kian Far, E., Geier, M., and Krafczyk, M. (2018). Simulation of rotating objects in fluids with the cumulant lattice Boltzmann model on sliding meshes. *Computers & Mathematics with Applications*, DOI: <https://doi.org/10.1016/j.camwa.2018.08.055>.
- (7) Succi, S., *The lattice Boltzmann equation: for fluid dynamics and beyond*; Oxford University Press: 2001.
- (8) Kian Far, E., Geier, M., Kutscher, K., and Krafczyk, M. (2017). Implicit Large Eddy Simulation of Flow in a Micro-Orifice with the Cumulant Lattice Boltzmann Method. *Computation* 5, DOI: [10.3390/computation5020023](https://doi.org/10.3390/computation5020023).
- (9) Bhatnagar, P. L., Gross, E. P., and Krook, M. (1954). A model for collision processes in gases. I. Small amplitude processes in charged and neutral one-component systems. *Physical Review* 94, 511.

- (10) Geier, M. et al. (2006). Ab initio derivation of the cascaded Lattice Boltzmann Automaton. *University of Freiburg–IMTEK*.
- (11) Geier, M., Greiner, A., and Korvink, J. G. (2008). Reference frame independent partitioning of the momentum distribution function in lattice Boltzmann methods with multiple relaxation rates. *University of Freiburg: Freiburg, Germany*.
- (12) Seeger, S., and Hoffmann, H. (2000). The cumulant method for computational kinetic theory. *Continuum Mechanics and Thermodynamics* 12, 403–421.
- (13) Seeger, S, and Hoffmann, K. (2005). The cumulant method for the space-homogeneous Boltzmann equation. *Continuum Mechanics and Thermodynamics* 17, 51–60.
- (14) Geier, M., Schönherr, M., Pasquali, A., and Krafczyk, M. (2015). The cumulant lattice Boltzmann equation in three dimensions: Theory and validation. *Computers & Mathematics with Applications* 70, 507–547.
- (15) Manwell, J. F., McGowan, J. G., and Rogers, A. L., *Wind energy explained: theory, design and application*; John Wiley & Sons: 2010.
- (16) Geier, M., and Kian Far, E. In *The First International Workshop on Lattice Boltzmann for Wind Energy*, 2021.
- (17) Morris, P., Long, L., and Brentner, K. In *42nd AIAA aerospace sciences meeting and exhibit*, 2004, p 1184.
- (18) Robinson, M. C., Hand, M., Simms, D., and Schreck, S. Horizontal axis wind turbine aerodynamics: three-dimensional, unsteady, and separated flow influences., tech. rep., National Renewable Energy Lab., Golden, CO (US), 1999.
- (19) Tam, C. K. (1995). Computational aeroacoustics-Issues and methods. *AIAA Journal* 33, 1788–1796.
- (20) Wells, V. L., and Renaut, R. A. (1997). Computing aerodynamically generated noise. *Annual Review of Fluid Mechanics* 29, 161–199.
- (21) Kim, J. W., and Lee, D. J. (1996). Optimized compact finite difference schemes with maximum resolution. *AIAA Journal* 34, 887–893.

- 
- (22) Tam, C. K., and Webb, J. C. (1992). Dispersion-relation-preserving schemes for computational aeroacoustics.
  - (23) Cheong, C., and Lee, S. (2001). Grid Optimized Dispersion Relation Preserving Schemes on General Geometries for Computational Aeroacoustics. *Journal of Computational Physics* 174, 248–276.
  - (24) Gröschel, E, Schröder, W, Renze, P, Meinke, M, and Comte, P (2008). Noise prediction for a turbulent jet using different hybrid methods. *Computers & Fluids* 37, 414–426.
  - (25) Delfs, J., Bertsch, L., Zellmann, C., Rossian, L., Kian Far, E., Ring, T., and Langer, S. C. (2018). Aircraft Noise Assessment—From Single Components to Large Scenarios. *Energies* 11, 429.
  - (26) Colonius, T., Lele, S. K., and Moin, P. (1994). The scattering of sound waves by a vortex: numerical simulations and analytical solutions. *Journal of Fluid Mechanics* 260, 271–298.
  - (27) MITCHELL, B., LELE, S., and Moin, P. In *30th Aerospace Sciences Meeting and Exhibit*, 1992, p 374.
  - (28) Buick, J., Greated, C., and Campbell, D. (1998). Lattice BGK simulation of sound waves. *EPL (Europhysics Letters)* 43, 235.
  - (29) Dellar, P. J. (2001). Bulk and shear viscosities in lattice Boltzmann equations. *Physical Review E* 64, 031203.
  - (30) Brès, G., Pérot, F., and Freed, D. In *15th AIAA/CEAS Aeroacoustics Conference (30th AIAA Aeroacoustics Conference)*, 2009, p 3395.
  - (31) Latt, J., and Chopard, B. (2006). Lattice Boltzmann method with regularized pre-collision distribution functions. *Mathematics and Computers in Simulation* 72, 165–168.
  - (32) Malaspinas, O. (2015). Increasing stability and accuracy of the lattice Boltzmann scheme: recursivity and regularization. *arXiv preprint arXiv:1505.06900*.

- (33) Brogi, F., Malaspinas, O., Chopard, B., and Bonadonna, C. (2017). Hermite regularization of the lattice Boltzmann method for open source computational aeroacoustics. *The Journal of the Acoustical Society of America* 142, 2332–2345.
- (34) Zdravkovich, M. (1981). Review and classification of various aerodynamic and hydrodynamic means for suppressing vortex shedding. *Journal of Wind Engineering and Industrial Aerodynamics* 7, 145–189.
- (35) Lee, S.-J., Lim, H.-C., Han, M., and Lee, S. S. (2005). Flow control of circular cylinder with a V-grooved micro-riblet film. *Fluid Dynamics Research* 37, 246–266.
- (36) Bearman, P. W. (1965). Investigation of the flow behind a two-dimensional model with a blunt trailing edge and fitted with splitter plates. *Journal of Fluid Mechanics* 21, 241–255.
- (37) Kwon, K., and Choi, H. (1996). Control of laminar vortex shedding behind a circular cylinder using splitter plates. *Physics of Fluids* 8, 479–486.
- (38) Akilli, H., Karakus, C., Akar, A., Sahin, B., and Ozdil, N (2008). Control of Vortex Shedding of Circular Cylinder in Shallow Water Flow Using an Attached Splitter Plate. *Journal of Fluids Engineering-transactions of The Asme - J FLUID ENG* 130, DOI: [10.1115/1.2903813](https://doi.org/10.1115/1.2903813).
- (39) Kunze, S., and Brücker, C. (2012). Control of vortex shedding on a circular cylinder using self-adaptive hairy-flaps. *Comptes Rendus Mécanique* 340, Biomimetic flow control, 41–56.
- (40) Kamps, L., Geyer, T. F., Sarradj, E., and Brücker, C. (2017). Vortex shedding noise of a cylinder with hairy flaps. *Journal of Sound and Vibration* 388, 69–84.
- (41) Kian Far, E., Geier, M., Kutscher, K., and Krafczyk, M. (2016). Distributed cumulant lattice Boltzmann simulation of the dispersion process of ceramic agglomerates. *Journal of Computational Methods in Sciences and Engineering* 16, 231–252.
- (42) Filippova, O., and Hänel, D. (1998). Grid Refinement for Lattice-BGK Models. *Journal of Computational Physics* 147, 219–228.

- 
- (43) Gorakifard, M., Salueña, C., Cuesta, I., and Kian Far, E. In *The 16th International Conference for Mesoscopic Methods in Engineering and Science At: Heriot-Watt University, Edinburgh, Scotland*, 2019.
- (44) He, X., Luo, L.-S., and Dembo, M. (1996). Some Progress in Lattice Boltzmann Method. Part I. Nonuniform Mesh Grids. *Journal of Computational Physics* 129, 357–363.
- (45) He, X., and Doolen, G. (1997). Lattice Boltzmann Method on Curvilinear Coordinates System: Flow around a Circular Cylinder. *Journal of Computational Physics* 134, 306–315.
- (46) Mei, R., and Shyy, W. (1998). On the finite difference-based lattice Boltzmann method in curvilinear coordinates. *Journal of Computational Physics* 143, 426–448.
- (47) Xi, H., Peng, G., and Chou, S.-H. (1999). Finite-volume lattice Boltzmann method. *Physical Review E* 59, 6202.
- (48) Nannelli, F., and Succi, S. (1992). The lattice Boltzmann equation on irregular lattices. *Journal of Statistical Physics* 68, 401–407.
- (49) Peng, G., Xi, H., Duncan, C., and Chou, S.-H. (1999). Finite volume scheme for the lattice Boltzmann method on unstructured meshes. *Physical Review E* 59, 4675.
- (50) Lee, T., and Lin, C.-L. (2001). A Characteristic Galerkin Method for Discrete Boltzmann Equation. *Journal of Computational Physics* 171, 336–356.
- (51) Li, Y., LeBoeuf, E. J., and Basu, P. K. (2005). Least-squares finite-element scheme for the lattice Boltzmann method on an unstructured mesh. *Phys. Rev. E* 72, 046711.
- (52) Min, M., and Lee, T. (2011). A spectral-element discontinuous Galerkin lattice Boltzmann method for nearly incompressible flows. *Journal of Computational Physics* 230, 245–259.
- (53) Shu, C, Niu, X., and Chew, Y. (2002). Taylor-series expansion and least-squares-based lattice Boltzmann method: two-dimensional formulation and its applications. *Physical Review E* 65, 036708.



- 
- (54) Shu, C, Chew, Y., and Niu, X. (2001). Least-squares-based lattice Boltzmann method: a meshless approach for simulation of flows with complex geometry. *Physical Review E* 64, 045701.
- (55) Slater, J. C. (1934). Electronic energy bands in metals. *Physical Review* 45, 794.
- (56) Frazer, R. A., Jones, W. N. P., and Skan, S. W., *Approximations to functions and to the solutions of differential equations*; HSMO: 1937.
- (57) Chorin, A. J. (1973). Numerical study of slightly viscous flow. *Journal of Fluid Mechanics* 57, 785–796.
- (58) Bernard, P. S. (1995). A deterministic vortex sheet method for boundary layer flow. *Journal of Computational Physics* 117, 132–145.
- (59) Girault, V (1974). Theory of a finite difference method on irregular networks. *SIAM Journal on Numerical Analysis* 11, 260–282.
- (60) Perrone, N., and Kao, R. (1975). A general finite difference method for arbitrary meshes. *Computers & Structures* 5, 45–57.
- (61) Gingold, R. A., and Monaghan, J. J. (1977). Smoothed particle hydrodynamics: theory and application to non-spherical stars. *Monthly notices of the royal astronomical society* 181, 375–389.
- (62) Lucy, L. B. (1977). A numerical approach to the testing of the fission hypothesis. *The Astronomical Journal* 82, 1013–1024.
- (63) Nayroles, B, Touzot, G, and Villon, P (1992). Generalizing the finite element method: diffuse approximation and diffuse elements. *Computational Mechanics* 10, 307–318.
- (64) Belytscho, T, Lu, Y., and Gu, L (1994). Element-free Galerkin methods, *Int. J. Num. Methods*.
- (65) Belytschko, T, Krysl, P, and Krongauz, Y (1997). A three-dimensional explicit element-free galerkin method. *International Journal for Numerical Methods in Fluids* 24, 1253–1270.
- (66) Liu, W. K., Jun, S., and Zhang, Y. F. (1995). Reproducing kernel particle methods. *International journal for numerical methods in fluids* 20, 1081–1106.

- 
- (67) Liu, G.-R., and Gu, Y. (2001). A point interpolation method for two dimensional solids. *International Journal for Numerical Methods in Engineering* 50, 937–951.
- (68) Atluri, S. N., and Zhu, T. (1998). A new meshless local Petrov-Galerkin (MLPG) approach in computational mechanics. *Computational Mechanics* 22, 117–127.
- (69) Mukherjee, Y. X., and Mukherjee, S. (1997). The boundary node method for potential problems. *International Journal for Numerical Methods in Engineering* 40, 797–815.
- (70) Gu, Y., and Liu, G. (2002). A boundary point interpolation method for stress analysis of solids. *Computational Mechanics* 28, 47–54.
- (71) Musavi, S. H., and Ashrafizaadeh, M. (2015). Meshless lattice Boltzmann method for the simulation of fluid flows. *Physical Review E* 91, 023310.
- (72) Musavi, S. H., and Ashrafizaadeh, M. (2019). Development of a three dimensional meshless numerical method for the solution of the Boltzmann equation on complex geometries. *Computers & Fluids* 181, 236–247.
- (73) Tanwar, S. In *Analysis and Applications of Lattice Boltzmann Simulations*; IGI Global: 2018, pp 188–222.
- (74) Pribec, I., Becker, T., and Fattahi, E. (2021). A Strong-Form Off-Lattice Boltzmann Method for Irregular Point Clouds. *Symmetry* 13, 1802.
- (75) Kian Far, E., and Langer, S. In *the 13th International Conference on Theoretical and Computational Acoustics At: Vienna, Austria, 2017*.
- (76) Gorakifard, M., Salueña, C., Cuesta, I., and Far, E. K. (2021). Analysis of Aeroacoustic Properties of the Local Radial Point Interpolation Cumulant Lattice Boltzmann Method. *Energies* 14, DOI: [10.3390/en14051443](https://doi.org/10.3390/en14051443).
- (77) Gorakifard, M., Salueña, C., Cuesta, I., and Kian Far, E. (2022). The meshless local Petrov–Galerkin cumulant lattice Boltzmann method: strengths and weaknesses in aeroacoustic analysis. *Acta Mechanica* 233, 1467–1483.
- (78) Richardson, E. G. (1923). Aeolian tones. *Proceedings of the Physical Society of London* 36, 153–167.

- 
- (79) Etkin, B., Korbacher, G. K., and Keefe, R. T. (1957). Acoustic Radiation from a Stationary Cylinder in a Fluid Stream (Aeolian Tones). *The Journal of the Acoustical Society of America* 29, 30–36.
- (80) Blevins, R. (1984). Review of sound induced by vortex shedding from cylinders. *Journal of Sound and Vibration* 92, 455–470.
- (81) Blake, W. K., *Mechanics of flow-induced sound and vibration*, Includes bibliographies and index; Orlando, Fla. : Academic Press: 1986.
- (82) Norberg, C. (2003). Fluctuating lift on a circular cylinder: review and new measurements. *17*, 57–96.
- (83) Strouhal, V. (1878). Ueber eine besondere Art der Tonerregung. *Annalen der Physik* 241, 216–251.
- (84) Hardin, J. C., and Lamkin, S. L. (1984). Aeroacoustic Computation of Cylinder Wake Flow. *AIAA Journal* 22, 51–57.
- (85) Cox, J. S., Brentner, K. S., and Rumsey, C. L. (1998). Computation of Vortex Shedding and Radiated Sound for a Circular Cylinder: Subcritical to Transcritical Reynolds Numbers. *Theoretical and Computational Fluid Dynamics* 12, 233–253.
- (86) Inoue, O., Iwakami, W., and Hatakeyama, N. (2006). Aeolian tones radiated from flow past two square cylinders in a side-by-side arrangement. *Physics of Fluids* 18, 046104.
- (87) Tam, C. K. W. (1995). Computational aeroacoustics - Issues and methods. *AIAA Journal* 33, 1788–1796.
- (88) Lele, S. K. In *Numerical Modeling of Seismic Wave Propagation: Gridded Two-way Wave-equation Methods*; Society of Exploration Geophysicists: 2012.
- (89) Mazellier, N., Feuvrier, A., and Kourta, A. (2012). Biomimetic bluff body drag reduction by self-adaptive porous flaps. *Comptes Rendus Mécanique* 340, 81 – 94.
- (90) MITCHELL, B., LELE, S., and MOIN, P. In *30th Aerospace Sciences Meeting and Exhibit*.

- 
- (91) INOUE, O., and HATAKEYAMA, N. (2002). Sound generation by a two-dimensional circular cylinder in a uniform flow. *Journal of Fluid Mechanics* 471, 285–314.
- (92) Crouse, B, Freed, D, Balasubramanian, G, Senthooran, S, Lew, P., and Mongeau, L In *CEAS Aeroacoustics Conference and Exhibit, AIAA*, 2006, pp 06–2571.
- (93) Marié, S., Ricot, D., and Sagaut, P. (2009). Comparison between lattice Boltzmann method and Navier–Stokes high order schemes for computational aeroacoustics. *Journal of Computational Physics* 228, 1056–1070.
- (94) Viggen, E. M. (2014). The lattice Boltzmann method: Fundamentals and acoustics.
- (95) Dhuri, D. B., Hanasoge, S. M., Perlekar, P., and Robertsson, J. O. (2017). Numerical analysis of the lattice Boltzmann method for simulation of linear acoustic waves. *Physical Review E* 95, 043306.
- (96) Kataoka, T., and Tsutahara, M. (2004). Lattice Boltzmann model for the compressible Navier-Stokes equations with flexible specific-heat ratio. *Phys. Rev. E* 69, 035701.
- (97) Watari, M., and Tsutahara, M. (2003). Two-dimensional thermal model of the finite-difference lattice Boltzmann method with high spatial isotropy. *Phys. Rev. E* 67, 036306.
- (98) Noh, H.-M. (2019). Numerical analysis of aerodynamic noise from pantograph in high-speed trains using lattice Boltzmann method. *Advances in Mechanical Engineering* 11, 1687814019863995.
- (99) Dubois, F., and Lallemand, P. (2011). Quartic parameters for acoustic applications of lattice Boltzmann scheme. *Computers & Mathematics with Applications* 61, 3404–3416.
- (100) Dubois, F. (2013). Stable lattice Boltzmann schemes with a dual entropy approach for monodimensional nonlinear waves. *Computers & Mathematics with Applications* 65, 142–159.

- 
- (101) Li, Y., Shock, R., Zhang, R., and Chen, H. (2004). Numerical study of flow past an impulsively started cylinder by the lattice-Boltzmann method. *Journal of Fluid Mechanics* 519, 273.
- (102) Ricot, D., Marié, S., Sagaut, P., and Bailly, C. (2009). Lattice Boltzmann method with selective viscosity filter. *Journal of Computational Physics* 228, 4478–4490.
- (103) Lallemand, P., and Luo, L.-S. (2000). Theory of the lattice Boltzmann method: Dispersion, dissipation, isotropy, Galilean invariance, and stability. *Physical Review E* 61, 6546.
- (104) Xu, H., and Sagaut, P. (2011). Optimal low-dispersion low-dissipation LBM schemes for computational aeroacoustics. *Journal of Computational Physics* 230, 5353–5382.
- (105) Dellar, P. J. (2014). Lattice Boltzmann algorithms without cubic defects in Galilean invariance on standard lattices. *Journal of Computational Physics* 259, 270–283.
- (106) Qian, Y.-H. (1997). Fractional propagation and the elimination of staggered invariants in lattice-BGK models. *International journal of modern physics C* 8, 753–761.
- (107) Fan, H., Zhang, R., and Chen, H. (2006). Extended volumetric scheme for lattice Boltzmann models. *Physical Review E* 73, 066708.
- (108) Niu, X., Shu, C., Chew, Y., and Wang, T. (2004). Investigation of stability and hydrodynamics of different lattice Boltzmann models. *Journal of statistical physics* 117, 665–680.
- (109) Ansumali, S., and Karlin, I. V. (2002). Single relaxation time model for entropic lattice Boltzmann methods. *Physical Review E* 65, 056312.
- (110) Brownlee, R., Gorban, A. N., and Levesley, J. (2006). Stabilization of the lattice Boltzmann method using the Ehrenfests' coarse-graining idea. *Physical Review E* 74, 037703.
- (111) Brownlee, R., Gorban, A. N., and Levesley, J. (2007). Stability and stabilization of the lattice Boltzmann method. *Physical Review E* 75, 036711.

- 
- (112) Brownlee, R., Gorban, A. N., and Levesley, J. (2008). Nonequilibrium entropy limiters in lattice Boltzmann methods. *Physica A: Statistical Mechanics and its Applications* 387, 385–406.
- (113) Coreixas, C. G. High-order extension of the recursive regularized lattice Boltzmann method., Ph.D. Thesis, 2018.
- (114) Coreixas, C., Wissocq, G., Puigt, G., Boussuge, J.-F., and Sagaut, P. (2017). Recursive regularization step for high-order lattice Boltzmann methods. *Physical Review E* 96, 033306.
- (115) Feng, Y., Boivin, P., Jacob, J., and Sagaut, P. (2019). Hybrid recursive regularized thermal lattice Boltzmann model for high subsonic compressible flows. *Journal of Computational Physics* 394, 82–99.
- (116) Pasquali, A., Geier, M., and Krafczyk, M. (2020). Near-wall treatment for the simulation of turbulent flow by the cumulant lattice Boltzmann method. *Computers & Mathematics with Applications* 79, 195–212.
- (117) Reddy, J. N. (1993). An introduction to the finite element method. *New York* 27.
- (118) Kian Far, E. Simulation of Moving Body in Field Flow and Fluid Structure Interaction with using Lattice Boltzmann Method., Ph.D. Thesis, 2010.
- (119) Fard, E. G., Shirani, E., and Geller, S. In *13th. Annual International Conference fluid dynamic conference*, 2010.
- (120) Geller, S., Tölke, J., and Krafczyk, M. In *Fluid-Structure Interaction*; Springer: 2006, pp 270–293.
- (121) Mei, R., Yu, D., Shyy, W., and Luo, L.-S. (2002). Force evaluation in the lattice Boltzmann method involving curved geometry. *Physical Review E* 65, 041203.
- (122) Lorensen, W. E., and Cline, H. E. (1987). Marching cubes: A high resolution 3D surface construction algorithm. *ACM Siggraph Computer Graphics* 21, 163–169.
- (123) Luo, L. (2006). Consistent Initial Conditions for LBE Simulation. *preprint*.
- (124) Morse, P. M., and Feshbach, H. (1954). Methods of theoretical physics. *American Journal of Physics* 22, 410–413.

- 
- (125) Kinsler, L. E., Frey, A. R., Coppens, A. B., and Sanders, J. V. (1999). Fundamentals of acoustics. *Fundamentals of Acoustics, 4th Edition, by Lawrence E. Kinsler, Austin R. Frey, Alan B. Coppens, James V. Sanders, pp. 560. ISBN 0-471-84789-5. Wiley-VCH, December 1999. 560.*
- (126) Viggen, E. M. The lattice Boltzmann method with applications in acoustics., MA thesis, Norges teknisk-naturvitenskapelige universitet, Fakultet, 2009.
- (127) Gendre, F., Ricot, D., Fritz, G., and Sagaut, P. (2017). Grid refinement for aeroacoustics in the lattice Boltzmann method: A directional splitting approach. *Physical Review E* 96, 023311.
- (128) Tam, C. K., and Webb, J. C. (1993). Dispersion-relation-preserving finite difference schemes for computational acoustics. *Journal of Computational Physics* 107, 262–281.
- (129) Salomons, E. M., Lohman, W. J., and Zhou, H. (2016). Simulation of sound waves using the lattice Boltzmann method for fluid flow: Benchmark cases for outdoor sound propagation. *PloS One* 11, e0147206.
- (130) Vergnault, E., Malaspinas, O., and Sagaut, P. (2013). Noise source identification with the lattice Boltzmann method. *The Journal of the Acoustical Society of America* 133, 1293–1305.
- (131) Bouzidi, M., Firdaouss, M., and Lallemand, P. (2001). Momentum transfer of a Boltzmann-lattice fluid with boundaries. *Physics of Fluids* 13, 3452–3459.
- (132) Lallemand, P., and Luo, L.-S. (2003). Lattice Boltzmann method for moving boundaries. *Journal of Computational Physics* 184, 406–421.
- (133) Lienhard, J., and Liu, L. In, 1967.
- (134) Achenbach, E, and Heinecke, E (1981). On vortex shedding from smooth and rough cylinders in the range of Reynolds numbers  $6 \times 10^3$  to  $5 \times 10^6$ . *Journal of Fluid Mechanics* 109, 239–251.
- (135) Dahl, M. D. (2004). Fourth computational aeroacoustics (CAA) workshop on benchmark problems.
- (136) Kiya, M, Arie, M, Tamura, H, and Mori, H (1980). Vortex shedding from two circular cylinders in staggered arrangement.

- 
- (137) Cheong, C., Ryu, J., and Lee, S. (2006). Computation of aeolian tones from twin-cylinders using immersed surface dipole sources. *Journal of Mechanical Science and Technology* 20, 2292–2314.
- (138) Burton-Jones, A. et al. (2001). Knowledge capitalism: Business, work, and learning in the new economy. *Oup Catalogue*.
- (139) Letcher, T. M., *Wind energy engineering: A handbook for onshore and offshore wind turbines*; Academic Press: 2017.
- (140) Bowdler, D., and Leventhall, H., *Wind Turbine Noise*; Multi-Science Pub: 2011.
- (141) Wagner, S., Bareiss, R., and Guidati, G., *Wind turbine noise*; Springer Science & Business Media: 2012.
- (142) Singer, B. A., Lockard, D. P., and Brentner, K. S. (2000). Computational aeroacoustic analysis of slat trailing-edge flow. *AIAA Journal* 38, 1558–1564.
- (143) Tummala, A., Velamati, R. K., Sinha, D. K., Indraja, V, and Krishna, V. H. (2016). A review on small scale wind turbines. *Renewable and Sustainable Energy Reviews* 56, 1351–1371.
- (144) Spera, D. A. (1994). Wind turbine technology.
- (145) Gorakifard, M., Cuesta, I., Salueña, C., and Kian Far, E. (2021). Acoustic Wave Propagation and its Application to Fluid Structure Interaction using the Cumulant Lattice Boltzmann Method. *Computers & Mathematics with Applications*.
- (146) Chávez-Modena, M, Martínez, J., Cabello, J., and Ferrer, E (2020). Simulations of aerodynamic separated flows using the lattice Boltzmann solver XFlow. *Energies* 13, 5146.
- (147) Wood, S. L. Lattice Boltzmann Methods for Wind Energy Analysis., Ph.D. Thesis, University of Tennessee, 2016.
- (148) Deiterding, R., and Wood, S. L. In *Journal of Physics: Conference Series*, 2016; Vol. 753, p 082005.
- (149) Chen, Z., Shu, C., and Tan, D. S. (2018). The simplified lattice Boltzmann method on non-uniform meshes. *Commun. Comput. Phys* 23, 1131.



- 
- (150) Chen, H. (1998). Volumetric formulation of the lattice Boltzmann method for fluid dynamics: Basic concept. *Phys. Rev. E* 58, 3955–3963.
- (151) Liu, G.-R., and Gu, Y.-T., *An introduction to meshfree methods and their programming*; Springer Science & Business Media: 2005.
- (152) Liu, G., *Meshfree Methods: Moving Beyond the Finite Element Method, Second Edition (2nd ed.)* CRC Press: 2009, pp 1–692.
- (153) Liu, G., and Gu, Y. (2001). A local point interpolation method for stress analysis of two-dimensional solids. *Structural Engineering and Mechanics* 11, 221–236.
- (154) Liu, G., and Gu, Y. (2001). A local radial point interpolation method (LRPIM) for free vibration analyses of 2-D solids. *Journal of Sound and vibration* 246, 29–46.
- (155) Li, Q., Yang, H., Yang, F., Yao, D., Zhang, G., Ran, J., and Gao, B. (2018). Calculation of Hybrid Ionized Field of AC/DC Transmission Lines by the Meshless Local Petrov–Galerkin Method. *Energies* 11, 1521.
- (156) Bawazeer, S. (2019). Lattice Boltzmann Method with Improved Radial Basis Function Method.
- (157) Geier, M., Greiner, A., and Korvink, J. G. Reference frame independent partitioning of the momentum distribution function in lattice Boltzmann methods with multiple relaxation rates., 2008.
- (158) Schäfer, R., and Böhle, M. In *Acoustics*, 2020; Vol. 2, pp 735–752.
- (159) Ye, Q., Avallone, F., Van Der Velden, W., and Casalino, D. In *Journal of Physics: Conference Series*, 2020; Vol. 1618, p 052077.
- (160) Slater, J. C. (1934). Electronic energy bands in metals. *Physical Review* 45, 794.
- (161) Frazer, R. A., Jones, W. N. P., and Skan, S. W., *Approximations to functions and to the solutions of differential equations*; HSMO: 1937.
- (162) Girault, V (1974). Theory of a finite difference method on irregular networks. *SIAM Journal on Numerical Analysis* 11, 260–282.
- (163) Perrone, N., and Kao, R. (1975). A general finite difference method for arbitrary meshes. *Computers & Structures* 5, 45–57.

- 
- (164) Snell, C, Vesey, D., and Mullord, P (1981). The application of a general finite difference method to some boundary value problems. *Computers & Structures* 13, 547–552.
- (165) Gingold, R. A., and Monaghan, J. J. (1977). Smoothed particle hydrodynamics: theory and application to non-spherical stars. *Monthly Notices of the Royal Astronomical Society* 181, 375–389.
- (166) Monaghan, J. J., and Lattanzio, J. C. (1985). A refined particle method for astrophysical problems. *Astronomy and Astrophysics* 149, 135–143.
- (167) Lancaster, P., and Salkauskas, K. (1981). Surfaces generated by moving least squares methods. *Mathematics of Computation* 37, 141–158.





UNIVERSITAT  
ROVIRA i VIRGILI